Development and Characterization of Infrared Broadband Open-Path Hydrocarbon Detectors for Chemical Species Tomography

by

Roger Tsang

A thesis
presented to the University of Waterloo
in fulfillment of the
thesis requirement for the degree of
Master of Applied Science
in
Mechanical and Mechatronics Engineering

Waterloo, Ontario, Canada, 2017

Author's Declaration

I hereby declare that I am the sole author of this thesis. This is a true copy of the thesis, including any required final revisions, as accepted by my examiners.

I understand that my thesis may be made electronically available to the public.

Abstract

Chemical species tomography (CST) is an emerging diagnostic technique for estimating the spatial distribution of a chemical species of interest. This thesis focuses on using CST to detect and map fugitive hydrocarbon emissions resulting from crude oil refinement, where current methods of detecting and measuring these emissions can be costly and inaccurate. This technique utilizes multiple optical paths to measure path-integrated concentrations over a flow field that are used in reconstructions to obtain an estimated discrete distribution. Prior CST work has made use of diode lasers, ultraviolet differential optical absorption spectrometers, or Fourier transform infrared spectrometers. This thesis pioneers the use of broadband infrared open path detectors for CST.

A theoretical background is laid out with a discussion of the fundamentals of how E-M waves interact with gas molecules, which underlies the CST measurement principle. This is followed by an explanation of monochromatic tomography, which involves solving a rank-deficient problem through the context of a Bayesian problem with prior information. Broadband tomography is then developed on that foundation, requiring a transfer function to linearize the problem. Details of a design overview is presented for four open path broadband detector and emitter pairs that were fabricated for use in lab-scale tomography experiments. Focusing on the mid-infrared ro-vibrational band of hydrocarbons at approximately 3.3 μm, the pairs contain optical components suitable for operation at distances up to 10 m. These components include a thermal emitter, a collimating reflector, bandpass filter, focusing lens, and photovoltaic detector.

The detector pairs were validated and transfer functions were built with a calibration process through a custom-built absorption cell with gaseous species of methane, propane, and ethylene. Using known concentrations of one species at a time, the transmittance of an optical pair was compared to an expected model that was constructed from spectral data compiled in the HITRAN or PNNL databases. Twelve tomography experiments followed, culminating in a final successful proof-of-concept tomographic reconstruction of a propane plume that was validated with flame ionization detector measurements.

Acknowledgements

First and foremost, I would like to acknowledge my supervisor, Prof. Kyle Daun, for his patience, guidance, and encouragement over the course of my degree. Words alone cannot express my gratitude for the support he has provided over the years.

This degree would not have been possible without Imperial Oil and the National Sciences and Engineering Research Council for their funding. In particular, I would like to thank Dr. Sebastien Bergeron, Ross Christopher, and especially Alistaire Holmes for their expertise and assistance in conducting some of my experiments.

I would like to thank the technical staff in the Department of Mechanical and Mechatronics Engineering for lending me a hand when I needed it. Their kindness, knowledge, and experience was incredibly valuable and appreciated.

I would also like to thank Prof. Elizabeth Weckman and her graduate students, Matt DiDomizio and Nicole Nagy, for providing me with the space to do my experiments and help when I needed it. I think I say it every time, but I hope I was not too much in the way!

My friends, who are far too numerous to name, deserve recognition for the support and laughs that they have provided. I am incredibly lucky to be surrounded by the people that I am. In particular, I would like to thank Samuel Grauer, not only for the engaging and thoughtful conversations we have had, but for the immense help he has provided as a cohort on this project.

I would like to say thank you to my family, who have always been supportive and loving at every point of my journey thus far. Without them, I would not be where I am today.

Finally, I would like to thank my partner, Neil Proulx, who has been there for me, through every good and bad moment.

Dedication

This thesis is dedicated to my parents

Dr. Chin Fai Tsang

And in loving memory of

Anna Sau-Mei Tsang

Table of Contents

List of Figures

List of Tables

List of Abbreviations

BTEX	Benzene, toluene, ethylbenzene, and xylene
CEPA	Canadian Environmental Protection Act
CST	Chemical species tomography
DIAL	Differential absorbtion lidar
DOAS	Differential optical absorption spectroscopy
EMR	Electromagnetic radiation
FDS	Fire Dynamics Simulator
FID	Flame ionization detector
FTIR	Fourier transform infrared
GHG	Greenhouse gas
HITRAN	High transmission
LDAR	Leak detection and reporting
LEL	Lower explosive limit
LES	Large eddy simulation
LIDAR	Light detection and ranging
NPRI	National Pollutant Release Inventory
pdf	Probability density function
PID	Photoionization detector
PNNL	Pacific Northwest National Laboratories
RTE	Radiative transfer equation
TDLS	Tunable diode laser spectroscopy
TSM	Trajectory statistical method
VOC	Volatile organic compound

List of Symbols

γ_c	Collision broadened half-width
γ_D	Doppler broadened half-width
γ_n	Natural/self-broadened half-width
Γ_x	Spatial covariance
η	Wavenumber
κ	Absorption coefficient
λ	Wavelength
λ	Tikhonov parameter
ν	Frequency
$\pi(\mathbf{b})$	Bayesian evidence
$\pi(\mathbf{b} \mid \mathbf{x})$	Bayesian likelihood
$\pi(\mathbf{x} \mid \mathbf{b})$	Bayesion posterior
$\pi_{Pr}(\mathbf{x})$	Bayesian prior
σ_m	Noise standard deviation
σ_η	Absorption cross-section
$\mathbf{A}$	Ray-sum matrix
a_{ij}	Pixel path length
b	Path-integrated measurement
$\mathbf{b}$	Measurement vector
c_0	Speed of light, $c_0 = 299{,}792{,}458\ m/s$
C_1	Constant, $C_1 = hc_0^2$
C_2	Constant, $C_2 = hc_0/k$
C_η	Spectral shape function
$c_i(s)$	Local concentration
D	Effective diameter
F	View factor
G	Transfer function

h	Planck's constant, h = 6.626 × 10-34 $J \cdot s$
I	Intensity
k	Boltzmann's constant, k = 1.381 × 10^{-23} J/K
M	Molecular mass
m	Number of paths
n	Number of pixels
n	Index of refraction
N	Number of molecules
P	Pressure
P	Power
R°	Universal gas constant
S	Line strength
T	Temperature
T	Transmittance
$\mathbf{x}$	Pixel concentration estimate vector
$\overline{\boldsymbol{x}}$	Mean distribution
$\mathbf{x}^{MAP}$	Maximum *a posteriori* estimate

Introduction

1.1 Motivation

Canada's upstream oil and gas sector is responsible for the largest portion of greenhouse gas (GHG) emissions, amounting to approximately 26% of the nation's greenhouse gas inventory [1], shown in Figure 1. Fugitive hydrocarbon emissions from the oil and gas sector, in particular, are responsible for approximately 8% of the total inventory in 2015, and grew by 24% over the period from 1990 to 2013, mainly as a result of increased production during the same time period [2].

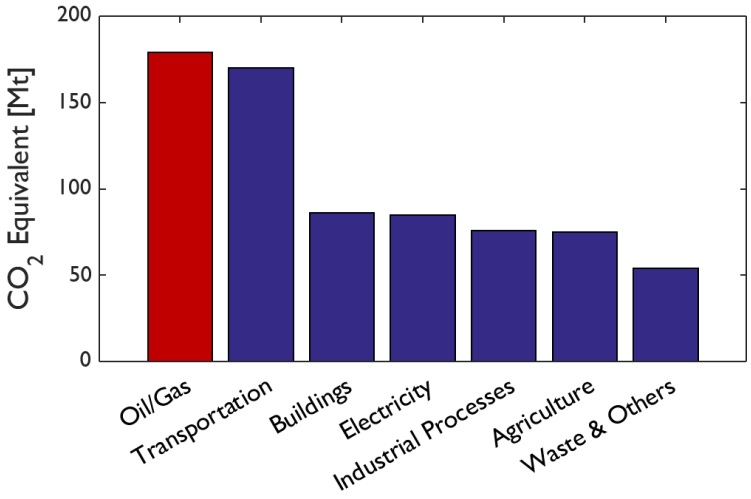

Figure 1: Breakdown of carbon dioxide-equivalent emissions in Canada by sector for 2013 [2]**.**

Fugitive emissions can be intentional or unintentional releases of hydrocarbons (including light hydrocarbons, such as methane, as well as more complex volatile organic compounds (VOCs)) as a result of industrial activities (related to production, processing, transportation, and storage). Sources of fugitive emissions include, but are not limited to, valves, seals, pipe connections, etc. [3]. Another example of a fugitive emission source are API (American Petroleum Institute) separators (as shown in Figure 2), which are large open surfaces from which hydrocarbons can evaporate.

Figure 2: A photograph of a typical API separator at an industrial site.

The main VOCs of interest are aromatic hydrocarbons of benzene (C_6H_6), toluene (C_7H_8), ethylbenzene (C_8H_{10}), and the three xylene (C_8H_{10}) isomers, which together are identified as "BTEX". These compounds have various health and environmental impacts that are discussed in more detail in Section 1.1.2. Imperial Oil, as a producer of oil and gas in Canada, is committed to carrying out their production in a safe and environmentally responsible manner. Supported by a University Research Award and a National Sciences and Engineering Research Council Collaborative Research and Development (NSERC-CRD) grant, this project aims to detect and measure BTEX emissions that are released from API separators. With BTEX as the principal emission of interest, a primary experimental focus of this thesis is on toluene because it is the least hazardous molecule of the group. Methane and propane are also prominent targets as they are gas-phase species that are readily available, easy to work with, and exhibit similar optical absorption properties to toluene.

1.1.1 Environmental Impact of Greenhouse Gas Emissions

With current atmospheric levels of carbon dioxide (CO_2) having reached approximately 400 ppm [4], it is difficult to overstate the threat climate change poses to almost every ecosystem on the planet and the future of civilization. Atmospheric CO_2 levels have been rising at an accelerating pace that correlates with the start of the Industrial Revolution at the end of the 18th century [5]. This can be seen in the Keeling curve, shown in Figure 3, which is a measure of atmospheric CO_2 levels over time.

These measurements were taken at the Mauna Loa Observatory starting in 1958, with measurements continuing to be taken today. Antarctic ice core analysis provides atmospheric CO_2 levels dating back 420,000 years, also shown in Figure 3, indicating that CO_2 levels have consistently remained between 180 and 300 *ppm* over this time period [6].

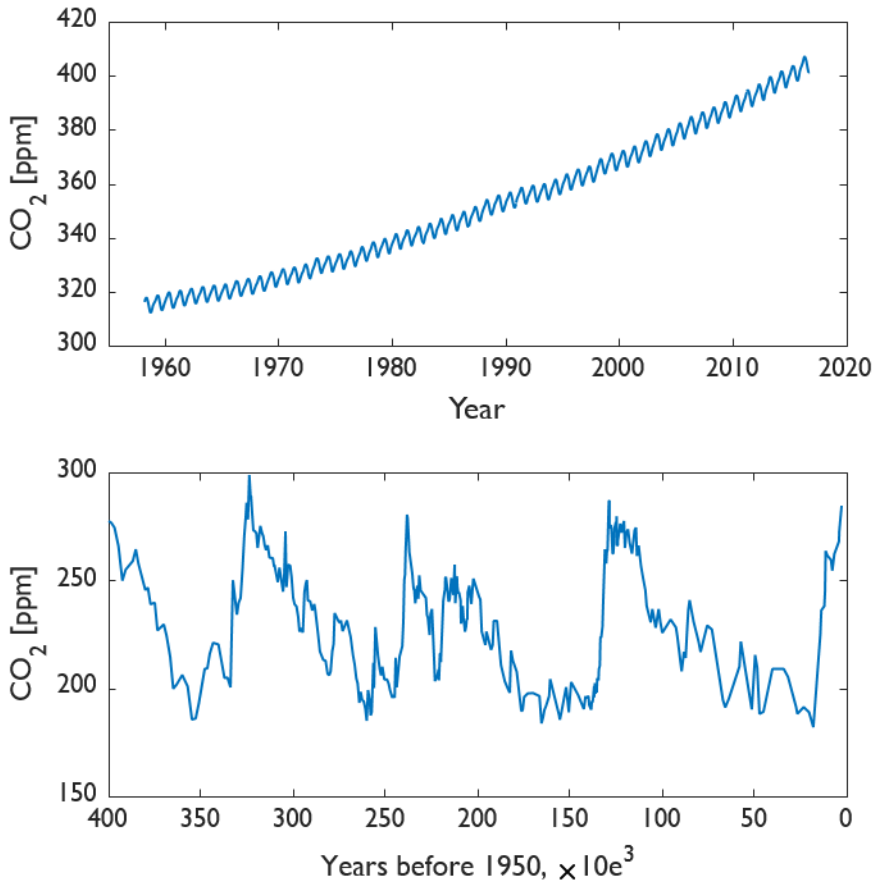

Figure 3: Keeling curves showing the concentration of atmospheric CO_2 levels over time; regular measurements since 1958 at an observation station in Mauna Loa (upper) as well as air analysis from Antarctic ice core samples (lower) [4], [6]**.**

While the emphasis of the discussion on climate change and global warming is generally centred on CO_2 levels, many other species are significant contributors. The Intergovernmental Panel on Climate Change (IPCC) uses various metrics to quantify the relative contributions to climate change, such as Global Warming Potential (GWP) and Global Temperature change Potential (GTP). The GWP is a

measure of the time-integrated radiative forcing caused by a burst emission of a particular component compared to an equal mass of CO_2, with methane (CH_4) having a GWP of 84 over 20 years [7]. This means that over a 20-year period, the energy introduced into the Earth's system by CH_4 is greater than that by CO_2 by a factor of 84. In this way, methane and other species are included in the discussion by way of an equivalent impact factor. A CO_2-equivalent conversion is also used, in which an amount of a particular hydrocarbon is considered equivalent based on the CO_2 that would be produced through the combustion reaction.

As atmospheric CO_2 levels increase, so too does the global mean surface temperature. According to the IPCC, the average temperature of the Earth's surface has successively increased in each decade from the 1980's to the 2000's, with the 2000's being the warmest on instrumental record (since the late 19th century) [8]. Combined land and ocean temperature data has shown that the average surface temperature has increased 0.85 K between 1880 and 2012. The report goes on to present atmospheric changes that have occurred in recent history, such as: there is a very likely chance (90-100% probability) that global near surface and tropospheric air specific humidity have increased since the 1970's; it is very likely that Arctic sea ice extent decreased between 1979-2012; there is medium confidence that the Arctic summer sea ice retreat for the current period (1980-2012) was unprecedented; the sea surface temperatures were anomalously high for at least the last 1,450 years; the global mean sea level has risen by 0.19 m very likely at an increasing rate; etc. [8].

Further increases in the global mean surface temperature correspond with many other global geographic changes. A natural expectation is that the Arctic sea ice extent will further decrease and eventually disappear, while the West Antarctic and Greenland ice sheets will experience partial melting. A projected estimation of the sea level rise, based on past observed sea level increases and temperature data, shows that the sea level is expected to rise by between 0.75 and 1.9 m by the end of this century [9]. If a warming of 4 $^{\circ}C$ is reached, it is speculated that there will be more extreme and disastrous weather events across the globe, a shortage of water will be experienced as mountain glaciers shrink rapidly, heavy wildlife extinction including coral reefs, and a drying of the Amazon rainforest [10].

Given its broad and severe consequences, efforts are being made to halt the acceleration of climate change. The Paris Agreement was adopted by the United Nations Framework Convention on Climate Change (UNFCCC) in December of 2015. As of November 2016, 115 of 197 parties have ratified the agreement, including Canada. Article 2 of the agreement states:

> 1. *This Agreement, in enhancing the implementation of the Convention, including its objective, aims to strengthen the global response to the threat of climate change, in the context of sustainable development and efforts to eradicate poverty, including by:*
>
>   a. *Holding the increase in the global average temperature to well below 2°C above pre-industrial levels and pursuing efforts to limit the temperature increase to 1.5°C above pre-industrial levels, recognizing that this would significantly reduce the risks and impacts of climate change;* … [11]

1.1.2 Health Impact of Fugitive Emissions

When discussing the impact of fugitive emissions on human health, specific focus shifts to VOCs such as BTEX. While toluene, ethylbenzene, and xylene have been shown to be non-cancerous, benzene is known to be hematotoxic, immunotoxic, genotoxic, and carcinogenic under chronic exposure conditions [12]. Other conditions identified as a result of benzene exposure include aplastic anemia, thrombocytopenia, and acute myelogenous leukemia.

Consequently, occupational chronic exposure to benzene is understandably a concern, which is why organizations like the OSHA, WHO, and EU (Directive 2008/50/EC) have guidelines for acceptable safe limits of exposure. Residents living near refineries have justifiable reason for concern, which has a result of being the motivation for numerous studies across the globe on cancer incidence and other negative effects due to benzene exposure, although epidemiology studies have been inconclusive or contradictory.

Lyons et al. [13] and Sans et al. [14] independently studied the incidence of leukemia and cancers in residents near a petrochemical plant at Baglan Bay, South Wales between 1974 and 1991, motivated by an alleged cluster of cancer cases between 1984 and 1989. Lyons et al. focused on the age group under 25 years that lived within 1.5 and 3 km of the plant and found that while there was a greater incidence of leukemia or lymphomas in the area, there was no significant excess [13]. Sans et al. focused on a 7.5 km radius around the plant and analyzed cancer incidence and mortality for multiple specific periods; they concluded that while there was an excess incidence of cancers within the 7.5 km radius, it was comparable with the rest of the surrounding area of West Glamorgan, where there was no relationship between the incidence of cancer and the distance from the plant [14].

Another study taken up by Axelsson et al. examined the incidence of leukemia, lymphoma, and lung, liver, and central nervous system cancers in Stenungsund, Sweden, concluding that there was no evidence that there was an increased risk for living near petrochemical industry [16]. Baltrenas et al. performed measurements of atmospheric levels of BTEX in Lithuania. Finding an average concentration range of 2.12 to 2.75 ppbv of benzene, the authors conclude there is no significant change in air quality in the vicinity of the crude oil refinery [17]. Wilkinson et al., in an analysis of 7 different major oil refineries around Great Britain between 1974 and 1991, found no significant increase in the risk of leukemia or non-Hodgkin's lymphoma within 2 km or 7.5 km of residency [18]. However, there was a weak association found between Hodgkin's lymphoma and proximity of residency to a refinery.

On the opposing side, studies of refinery areas in Italy, USA, Turkey, and Taiwan have shown that living in the vicinity carries a carcinogenic risk. Belli et al. investigated the area of Brindisi, Italy near a petrochemical plant. Using mortality data, they concluded that there were moderate increases in the risk of developing lung and bladder cancers as well as lymphohematopoietic neoplasms when living within 2 km of the plant [19]. In the US, Kaldor et al. performed an ecologic study to find associations between cancer incidence/mortality and estimated residential proximity to petroleum and chemical industry emissions. They found that there was an increased incidence in cancer of the buccal cavity and of the pharynx in both men and women, and of the stomach, lung, prostate, kidney, and urinary organs in men [20]. In Turkey, 58 VOCs were detected at 40 different sites, including 1,2-dichloroethane, benzene, chloroform, and carbon tetrachloride. In the study, Dumanoglu et al. conclude that the

carcinogenic risks are considerably high when taking the high concentrations of these VOCs into consideration [21]. In two separate studies of Taiwanese residents near petrochemical plants, it was found that there was an excess in mortality in men for liver cancer [22] and in women for lung cancer that is not explained by smoking habits [23].

In addition to carcinogenic risks, residents living near a petrochemical plant often complain about odours that arise that may also be associated with symptoms and effects such as fatigue, headaches, dizziness, nausea, respiratory irritation, and asthma [17], [22]–[26]. Effects may even be as extreme as altered sex ratios at birth and an excess risk of low-birth rate deliveries in babies at term [23], [26]].

Regardless, there appears to be sufficient scientific evidence to justify the concern of people who reside within the vicinity of petrochemical processing facilities. It is these reasons, along with the environmental concerns discussed above, that make it important for the government to implement legislative measures for tracking and reducing emissions.

1.2 Legal Requirements and Measurement Techniques for Oil & Gas Facilities

As a part of the Canadian federal government's effort to address climate change and air quality issues, the Canadian Environmental Protection Act (CEPA) of 1999 was introduced [27]. This act states that the Minister will publish a national inventory of releases of pollutants to assist the government to protect the environment and the health of Canadians. The result is the National Pollutant Release Inventory (NPRI), which is a collection of facility-specific information regarding the release, disposal, and recycling of substances, including toxic substances as well as pollutants that affect the quality of air. These substances are outlined under Section 63 of the CEPA. Sections 47, 49, and 51-53 outline the guidelines for collection and publication of pollution data. Facilities that meet or exceed the thresholds (either 20,000 employee-hours worked or Criteria Air Contaminant thresholds) are required to report to the NPRI on an annual basis.

Currently, fugitive emission estimation practices for the NPRI are based on US EPA guidelines for leak detection and reporting (LDAR) [28]. These guidelines state that a portable organic vapour analyzer that meets the minimum criteria must be used to detect individual components. If the component measures a gas concentration that exceeds the threshold, it is deemed to be leaking. Once

leaking components are identified, emission factors for each component are applied and summed to estimate the total emission inventory for the facility.

Emission factor techniques are mainly centered on using correlation factors obtained through various methods varying in complexity. In its simplest form, total emission estimates are obtained from empirical factors from basic individual components (e.g. valves, pumps, flanges, etc.) in conjunction with a survey of components of the plant in question to form a total emission value to report. These factors may be updated for a specific component or have specific correlations developed, however this requires significant amounts of additional work. Companies may develop a database of factors unique to their own facility for more accurate reporting.

While emission factors are an acceptable method for estimating total emission losses, they have been shown to be inaccurate. By some accounts, the emission factors method has been shown to overestimate fugitive emissions, on the order of 4000 kg/year estimated vs. 1.5 kg/year actual loss through bagging and sampling [29]. However, in another case, differential absorption LIDAR (DIAL) measurements, discussed in the next section, at two Alberta gas plants by Chambers et al. demonstrated that emission factor estimates of methane and VOC emissions underestimated actual emission releases by a factor of four to eight [30]. Another study showed emission factors to severely underestimate emissions for storage tanks by a factor of 448 times in one case. In other cases from the same study, benzene and other VOC emissions were measured to be 5 to 20 times larger than values determined through emission factor usage [31].

In addition to the interest of meeting regulatory requirements, fugitive emissions can represent a large loss in revenue for the oil and gas companies. The DIAL measurements previously mentioned have shown that losses over a number of weeks can translate into losses worth several hundred thousand dollars [30]. Unfortunately, measurements of this nature are too expensive to conduct on a regular basis, so emission factor estimations are the industry standard [29], [31].

1.3 Detection Techniques

The emission flux estimation methodology defined by Method 21 [28] is frequently complemented with additional techniques for detecting VOCs and hydrocarbon emissions. The techniques discussed in

this section can be split into three categories: traditional techniques, point detection methods, and large-area measurements.

1.3.1 Traditional Techniques

Historically, other than emission factors, methods of detection and measurement of fugitive emissions fall into one of two categories: engineering estimates or material balance techniques [29].

Techniques based around engineering estimates come in the form of software tools. In these cases, the losses are not highly variable and are predictable. Software available for wastewater treatment facilities includes PAVE, CHEMDAT7, WATER7, and FATE. TANKS provides accurate measurements for storage facilities. POSSEE is available for fugitive emissions, but is mainly a data control tool not generally recommended for calculation purposes, and TANKS is software used for estimating losses from storage tanks.

Material balance techniques compare the inputs and outputs of specific chemicals for processes. However, this method requires accurate measurement and tracking of these chemicals, which is not possible for all processes.

1.3.2 Point Detection

Point detectors are those that detect emissions in a relatively small area or volume. As such, they can be more generally categorized as closed-path devices. This includes flame- and photoionization detectors, soap solution, and Fourier transform infrared (FTIR) spectrometers.

1.3.2.1 Flame and Photo Ionization Detectors

Flame ionization detectors (FIDs) and photoionization detectors (PIDs) are based on similar principles of measuring ions to determine the concentration of a gas species. Their principles of operation differ slightly, and they are each suited to different applications.

An FID measures organic compounds through the ions produced by combustion of a carbon-based compound in a hydrogen flame. Since there are no ions produced in the combustion of hydrogen, the baseline signal is typically near zero [32]. FIDs typically feature low levels of noise, high sensitivity, predictable responses by nature, and are insensitive to external factors such as detector temperature and

hydrogen flow rate. However, FIDs cannot detect inorganic substances (e.g. CO, CO_2, etc.), require O_2 and H_2 sources for the flame, and have a long initial warm-up time [33]. Additionally, they are a destructive method of measurement, and a dilutor kit must be used if high concentrations of hydrocarbons are being detected (i.e. if the sample contains less than <14% O_2 by volume) by virtue of the operating principle.

Photoionization detectors, on the other hand, are a non-destructive form of measurement. PID instruments use a UV lamp of a specific energy to ionize the compounds in question in a separate chamber. The ions collect on an electrode and the resulting current produced is proportional to the compound concentration. As a result, PIDs do not require O_2 or H_2 like FID, are much more sensitive to select components (up to 5-50 times), and are able to detect aromatics and inorganic compounds (e.g. ammonia, carbon tetrachloride, formaldehyde, hydrogen sulfide, etc.) [34]. Unfortunately, the dynamic range of PID (1-2000 *ppm*) is smaller than that of FID (0-10000 *ppm*), they are susceptible to water vapour interference, and are insensitive to some hydrocarbons.

1.3.2.2 Soap Solution

Soap solution is an alternate method for detecting fugitive leaks listed in EPA's Method 21. The principle is based on the visual discovery of bubble formation after a soap solution is sprayed onto a potential leak source. However, this leak detection method carries some limitations: the potential leak source cannot have continuously moving parts; the surface temperature must be between the freezing and boiling points of the soap solution; it must not have open areas to the atmosphere that the solution cannot bridge; and the source must not show signs of liquid leaks. Once a leak has been confirmed, the component must be measured by an instrument that meets the specifications outlined in the document (e.g. FID) [28].

1.3.2.3 Closed-path Fourier Transform Infrared

FTIR spectroscopy is a technique for measuring the absorbance of a sample with a broadband infrared scan of the sample. This technique is based on a Michelson interferometer (see Figure 4), where a beam of light is passed through a beamsplitter. One half is sent a certain distance to a fixed mirror, while the other half travels to a moving mirror, resulting in a variable distance. Once reflected back towards the

beamsplitter, the beam halves combine and the intensity is measured at the detector to produce an interferogram (a plot of light intensity versus optical path difference). As given by wave theory, the intensity of light will vary depending on the amount of constructive or destructive interference that has occurred from the combination of light waves that have travelled different differences. Since a broadband light source is used, the total interferogram generated is a summation of interferograms from all wavelengths, and the Fourier transform is used to generate a transmittance spectrum [35].

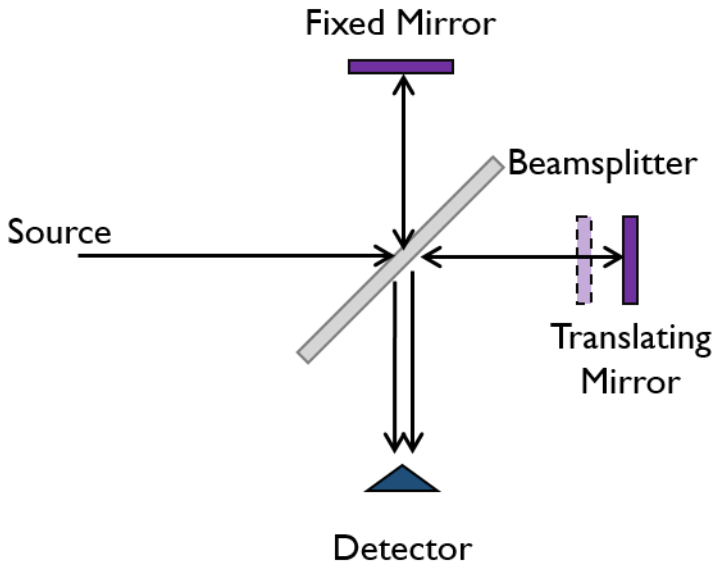

Figure 4: Schematic of a Michelson interferometer used in FTIR spectrometers.

1.3.3 Large-area Detection

Large area measurements can be categorized based on the underlying physical spectroscopic principle (i.e. absorption or emission), the wavelength spectrum used, and/or the light source used. The wavelengths used are typically centered between the UV and the far infrared, dependent on the species of interest and the light source used. Light sources can be either active or passive: active techniques use powered sources, whereas passive techniques use background or atmospheric light. Techniques used include, but are not limited to: tunable diode laser spectroscopy (TDLS); light detection and ranging (LIDAR); differential absorption LIDAR (DIAL); differential optical absorption spectroscopy (DOAS); trajectory statistical models (TSM); and chemical species tomography (CST). These methods are not

generally used for contained samples, and as such they are classed as open-path measurements. Figure 5 shows an example of the basic principle by which many detection methods operate. A light source generates an initial light intensity $I_{\eta 0}$ that is measured as $I_{\eta}(s)$ after it has traversed through an absorbing field. The concentration of the absorbing medium can be inferred in many forms depending on the technology used through the Beer-Lambert law, the governing equation discussed in more detail in Chapter 2.

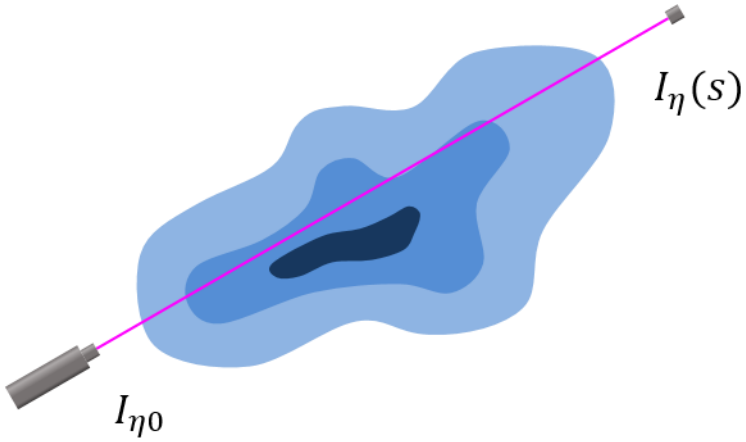

Figure 5: Spectral absorption of light intensity through an absorbing plume, $I_{\eta 0} > I_{\eta}(s)$.

1.3.3.1 Tunable Diode Laser Spectroscopy

Single absorption lines can be measured for an absorbing species using a laser that is tunable to narrow band frequencies. Laser light is highly collimated and intense, which allows for detection of the weaker overtone bands in the near IR region over long path-lengths [36], and can scan across a spectral range for a spectrally-resolved measurement. However, disadvantages include the cooling requirements for some lasers, as well as the safety hazards present when operating the instrument. Specifically, lasers used for spectroscopy are class 3B and 4 lasers, which are hazardous to the eye and skin. Class 4 lasers are powerful enough such that even the diffuse reflections present eye and skin hazards [37]. Operation of these lasers in open air is problematic and is restricted to highly controlled laboratory settings.

Resulting TDLS absorption measurements are path-averaged, which provides information about the concentration of the species of interest, but not the spatial variation.

1.3.3.2 Differential Optical Absorption Spectroscopy

DOAS is a method for analyzing the compositions of gases, typically used for trace gas measurement of the atmosphere. Based on the principle demonstrated in Figure 5, DOAS can determine gas compositions using two measured wavelengths for analysis. One wavelength is a strongly absorbing wavelength of the gas of interest, and the second is a weakly absorbing wavelength. In this way the column density of a gas can be found. In a majority of active DOAS system designs, arc lamps are used as the main light source [36] due to their brightness and smooth emission spectrum. Passive designs using direct sunlight as a source also exist, but complications arise due to several factors: the beam component of sunlight cannot be obscured by clouds; and strong atmospheric absorption lines (known as Fraunhofer lines) exist in the UV spectrum that overlap with those of many species of interest, thereby complicating the measurement.

1.3.3.3 Light Detection and Ranging

Light Detection and Ranging (LIDAR), which was originally named to reflect RADAR (radiowave detection and ranging) technology, uses a pulsed laser light into the atmosphere to detect atmospheric compounds and particles. By measuring the backscattered intensity as a function of time, the spatial distribution of the measured species can be deduced. However, LIDAR has several key disadvantages. Since the technique relies on backscattered intensity, it can be difficult to discern the difference in backscattering and total atmospheric scattering/extinction, and since backscattering is normally weak, the sensitivity is quite low [36]. Economically speaking, LIDAR systems are also large, complex, and expensive, requiring highly skilled operators [38].

1.3.3.4 Differential Absorption LIDAR

As an extension to LIDAR, DIAL uses laser pulses of two adjacent wavelengths in order to determine concentrations of a specific species. While one pulse is strongly absorbed by the species, the other is relatively transparent. The ratio of these measurements is proportional to the number density of the species, resulting in a measurement that pinpoints the concentration and locations of a specific spectrally-absorbing species.

1.3.3.5 Trajectory Statistical Models

TSMs are a method of locating fugitive emission sources by combining downstream concentration measurements with local wind condition data. TSMs have been used for pollutant source identification at the continental scale, but have been investigated in building-scale scenarios. In a study of TSMs, Brereton and Johnson [39] evaluated four different models: potential source contribution function; concentration-weighted trajectory; residence time-weighted concentration; and quantitative transport bias analysis. A proof-of-concept using computational fluid dynamics (CFD) simulations found that TSMs are a potential solution to locating fugitive emissions at industrial facilities.

1.3.3.6 Open-path Fourier Transform Infrared

While FTIR has traditionally been a closed-path technique for analyzing gas samples (see Section 1.3.2.3), FTIR can also be adapted for atmospheric measurement monitoring by two methods: extractive monitoring and open-path FTIR spectrometry. In extractive monitoring, a sample of the atmosphere is placed inside a multi-pass gas cell and analyzed. However, as a localized technique, there will always be uncertainty regarding the homogeneity of the sample with respect to the rest of the surrounding atmosphere. In contrast, in open-path FTIR spectrometry the light path is shone directly across the area of interest. This method also only returns path-integrated measurements, so localized detection is not possible. The other main downside of this technique is that the background spectrum of baseline measurements is rarely ideal, and some form of correction is almost always necessary [40].

1.4 Chemical Species Tomography

CST is an emerging imaging technique that has the potential to generate estimates of gas-phase species concentration distributions from light intensity measurements that are resolved both temporally and spatially. In CST, a model of light-matter interaction is used to deconvolve multiple open-path light absorption measurements, resulting in an image of the species concentration distribution. Optical tomography separates into three main categories: emission tomography, low-scattering tomography, and high-scattering tomography [41]. Gaseous flows, typically the focus of CST, exhibit little-to-no scattering [42], and fall into the low-scattering tomography category, which will be the focus of this thesis. Figure 6 shows an example of the basic principle.

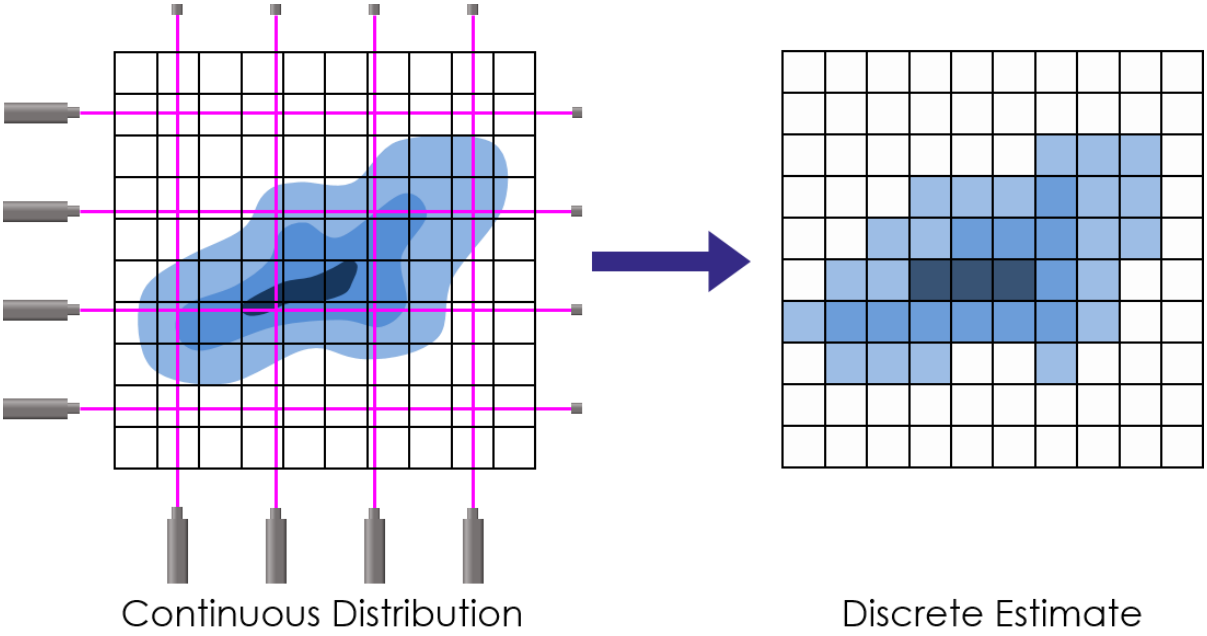

Figure 6: An example of chemical species tomography in which multiple open path measurements are used to estimate the spatial distribution of an absorbing species.

Ideally, lasers or commercial open path detectors are used for CST. However, these instruments are costly even for a single path, in addition to the fact that lasers are a hazard source for eye and skin injuries. The following subsections will outline the various applications in which CST is used. Starting with the historical origins of the technique, the discussion will be followed by a review of some noteworthy applications.

1.4.1 Proposal for CST

The first CST studies were numerical simulations aimed to determine the feasibility of CST for measuring concentrations of air pollutants. B.W. Stuck proposed using laser measurements around a region to detect pollutants (such as nitrogen dioxide, particulates, sulfur dioxide, ozone, and hydrocarbons) in conjunction with a Radon transform algorithm in 1977, where he found good agreement between the theoretical analysis and computer simulations [43]. Byer and Shepp proposed a technique to map a 2D concentration map over a source of pollution in 1979. In their technique, a single tunable laser is placed in the centre of a radius, while mirrors and detectors are placed around the

circumference of the circle, measuring the attenuation of the laser signal by air pollutants [44]. Wolfe and Byer expand further upon this work with a model study published in 1982 [45], in which they discuss the application of laser absorption tomography over kilometer-sized areas to reconstruct 2D maps of air pollution concentration based on model simulations to demonstrate potential for the technique.

1.4.2 Lab-scale Flame and Chemical Analysis

The first experimental study of chemical species tomography was performed by Santoro and Semerjian in 1981 [46]. Their work presents tomography applied to an off-axis turbulent methane-air jet to determine the mean concentration of methane within the jet using a 3.39 μm He-Ne laser with a multiangular absorption approach. The multiangular absorption approach uses a number of parallel absorption measurements at equally spaced angles, resulting in a matrix data set that was used to reconstruct the property field. Tomography techniques were then expanded to experiments involving liquid droplets and vapour species. Yule et al. measured the droplet sizes and concentrations of kerosene sprays at various conditions by measuring scattered He-Ne laser light [47], while Bennett et al. used the convolution backprojection algorithm in conjunction with fan beam geometry absorption measurements of an argon ion laser through an iodine vapour to map the density of the plume [48].

More recently, experimental CST research has increased due to the rapid technological advancements in detectors, spectroscopic devices, and computing power. Experiments carried out between the first experiment conducted by Santoro and Semerjian and the present include, but are not limited to: asymmetric flame temperature distribution estimation through a Multiplicative Algebraic Reconstruction Technique (MART) using Mach-Zehnder interferometer measurements of a He-Ne laser [49]; absorption coefficient and temperature distribution estimations of an ethylene flame using a tungsten filament source based on emission-absorption tomography by Hall and Boncyzk [50]; He-Ne laser absorption measurements to reconstruct a helium-argon jet using a finite-domain direct inversion method with *a priori* information by Chung et al. [51], who were able to compare their experimental reconstructions with probe point measurements as well as simulated phantom projection results by Ravichandran and Gouldin [52] for good general agreement with errors $<30\%$ occurring near the peripheral regions.

1.4.3 Engine Cylinder Diagnostics

Internal combustion (IC) engines have become a large area for CST research, due in large part to the University of Manchester's Industrial Process Tomography group and their collaborators. Early research began with Carey et al. presenting a tomography technique using near-IR measurements of iso-octane inside an IC engine to map the concentration distribution [53], followed closely by Hindle et al., who did measurements of non-stationary plumes of a propane and butane mixture inside an 85 *mm* diameter chamber to mimic an IC engine cylinder [54]. Development in the area led to the detailing of the design of the dual wavelength Near-InfraRed Absorption Tomography (NIRAT) technique, and the first (non-tomography) measurements of in-cylinder IR absorption of iso-octane using an optical access layer (dubbed OPAL) by Wright et al. [55].

Since then, research within the group has expanded considerably, with development resulting in in-cylinder measurements of an automotive production engine using irregular and sparse beam arrays [56], validation tests of the NIRAT with corresponding tomographic reconstructions [57], and mixture strength visualization of liquefied natural gas in a large-bore marine engine [58]. Additionally, the FLITES (fibre-laser imaging of gas turbine exhaust species) program is an industry-academia collaborative effort devoted to applying laser absorption CST techniques to aviation turbine- and fuel-related research and development [59], [60].

1.4.4 Environmental Monitoring

While most of the CST research to date has focused on lab-scale experiments, including flames, jets, and IC engine diagnostics, the technique has also been applied to large-scale imaging scenarios. With cost reductions in optical measurement techniques and fast computing resources, CST is quickly becoming a viable diagnostic for the measurement and detection of emissions.

UV-based DOAS (UV-DOAS) has been proposed for tomography purposes, where Pundt and Mettendorf modified a single DOAS unit to provide four optical paths using a series of retroreflectors [61]. Using the instrument, they performed atmospheric measurements of NO_2, SO_2, H_2CO, and O_3 with similar trace detection limits to those of traditional DOAS units. Since then, DOAS-based tomography has received more attention. Johansson et al. reported an algorithm used experimentally to

reconstruct cross-sectional gas plumes from a single elevated point (at an Andorran power plant in one experiment and at Mt. Etna in Italy in another), which were consistent with SO_2 flux estimates derived from simultaneous DOAS measurements of the plume [62]. In another study at Mt. Etna, Wright et al. used five automated scanning spectrometers to measure and tomographically reconstruct volcanic sulfur dioxide (SO_2) fluxes [63]. Their results were compared to concurrent SO_2 UV-DOAS flux measurements by Salerno et al. [64], where good agreement was found. In a third study of volcanic SO_2 flux emissions, Kazahaya et al. performed reconstructions of SO_2 concentration distributions around Miyakejima, Japan. In their procedure, they used three UV spectrometers and an airborne traverse technique in conjunction with tomography techniques for a total of four reconstructions [65].

CST techniques have also been used for real-time urban monitoring of BTEX and styrene. Olaguer et al. carried out a field study, Benzene and other Toxics Exposure (BEE-TEX), to perform tomographic remote sensing based on DOAS measurements over three residential communities near petrochemical facilities in Texas [66].

1.5 Thesis Objectives

The objective of this thesis is to document the evolution of the project within the boundaries of the project scope and goals set out by Imperial Oil. At the outset of the project, three main goals were identified:

1) Conduct a proof-of-concept line-of-sight attenuation measurement

2) a) Develop tomography reconstruction algorithms and,

   b) Conduct an experimental implementation of lab-scale LOSA-CST

3) Conduct field measurements of concentration distribution at Imperial Oil's Sarnia facility

This thesis focuses largely on segments of the first and second goals. A portion the first goal was groundwork design conducted previously, which is discussed briefly in Chapter 3. Improvements to the design are also discussed, with experimental characterization of the open-path detectors to serve as the line-of-sight proof-of-concept. The penultimate chapter of the thesis focuses on the experimental

implementation of lab-scale chemical species tomography on methane, propane, and ethylene plumes as a surrogate for BTEX.

The third goal is discussed briefly in terms of additional future work required to conduct field measurements. The current implementation of the detailed broadband open-path detectors do not permit resolved measurements for total mass flux as initially intended, and also do not meet the stringent safety requirements for devices intended to be operated at Imperial Oil's facilities.

1.6 Thesis Outline

This thesis presents the need for and development of a broadband chemical species tomography system for hydrocarbon detection.

Chapter 2 provides a review of the scientific knowledge that is required for tomography, starting with the basis of absorption spectroscopy and continuing with developing the equations and models used for broadband CST, beginning with monochromatic CST within a Bayesian framework as a stepping stone. Included in the discussion of absorption spectroscopy is the background of optical absorption of specific spectra by species, the resulting lines and broadening mechanisms, and models used to quantify absorption.

Chapter 3 describes the design considerations of a low-cost, broadband open-path optical detector. The chapter starts with the design of the initial prototype with discussion of part selection and specifications, expanding to the required improvements that were made in order to be ready for the tomography experiments. Improvements include new reflector selection, introduction of an alignment mechanism, as well as other minor design changes to facilitate simpler fabrication processes.

Chapter 4 presents the calibration procedure used to verify the accuracy of each emitter-detector pair that was manufactured. Experimental procedures and results are presented for multiple species of interest, including toluene, methane, ethylene, and propane.

Chapter 5 presents the proposed base tomography experiment as well as the results of each experiment. In total there were 12 experiments conducted, each with changing parameters based on knowledge and experience gained with each experiment.

Finally, Chapter 6 presents a summary of the project conclusions and outlines the recommended future work.

Chapter 2
Theoretical Background

The focus of this chapter is the derivation and discussion of the equations underlying the principles of absorption spectroscopy and tomographic reconstructions. The chapter starts with a description of electromagnetic radiation and its interaction with gas molecules, the broadening of spectral lines, and proceeds with the process of tomographic reconstruction. The discussion will begin with the monochromatic case and will continue with incorporating broadband measurements into the technique.

2.1 Electromagnetic Radiation

Electromagnetic radiation (EMR) is the directional propagation of coupled electric and magnetic waves that move at the speed of light ($c_0 = 299{,}792{,}458\ m/s$). Another interpretation of electromagnetic radiation is the flow of photons, which have momentum but no resting mass. The energy of EMR is defined by its wavelength frequency. Assuming a constant index of refraction $n = 1$ (i.e. through air or other molecular gases) the energy of a wave can be described as:

$$\frac{E}{hc_0} = \frac{1}{\lambda} = \frac{\nu}{c_0} = \eta \qquad [2.1]$$

where h is Planck's constant ($h = 6.626 \times 10^{-34}\ J \cdot s$), λ is the wavelength, ν is the frequency, and η is the wavenumber. Wavelength, frequency, and wavenumber can all be used interchangeably to denote the spectrum of a wave; preference for these terms is usually dependent on the application or field. For instance, in infrared spectroscopy it is beneficial to use wavenumber (which has units of cm^{-1}) since it is directly proportional to energy.

The electromagnetic spectrum is classified according to its wavelength or wavenumber in a vacuum, or by its frequency. Types of waves include gamma rays, x-rays, ultraviolet (UV), visible, infrared (IR), microwaves, and radio waves. The spectra corresponding to these wave types can be seen in Table 1 below, with converted wavenumber ranges for the infrared regions.

Table 1: Classification of electromagnetic radiation spectrum [67]**.**

Designation	Wavelength Range, λ	Wavenumber, η
Gamma-ray	$< 0.05\ A$	
X-Ray	$0.05 - 100\ A$	
Far (vacuum) UV	$10 - 180\ nm$	
Near UV	$180 - 350\ nm$	
Visible	$350 - 770\ nm$	
Near IR	$770 - 2500\ nm$	$12{,}900 - 4000\ cm^{-1}$
Middle IR	$2.5 - 50\ \mu m$	$4000 - 200\ cm^{-1}$
Far IR	$50 - 1000\ \mu m$	$200 - 10\ cm^{-1}$
Microwaves	$1 - 300\ mm$	
Radio Waves	$> 300\ mm$	

In terms of the photonic interpretation of electromagnetic radiation, a photon is the basic unit of radiative energy. The absorption or emission of a photon by a molecule corresponds to an increase or a decrease in energy, respectively, by the molecule. Absorption or emission by a molecule must correspond directly with energy state transitions in the molecule.

These energy state transitions can be categorized into three types of transitions: bound-bound; bound-free; and free-free (Figure 7). Bound-free transitions typically occur in cases when the initial energy of a molecule is very high; at high temperatures, for example. The result is continuous absorption across a wide spectrum due to the high kinetic energy levels which are not quantized. Free-free transitions occur in cases like plasmas, where free electrons are available for interaction.

In addition to electron orbital states, the internal energy of a molecule is also dependent on its rotational and vibrational energy, which is quantized. Electron orbital changes require larger amounts of energy, which corresponds to the short wavelengths in the ultraviolet and near-infrared ranges (0.1 to 1.5 μm). Vibrational and rotational energy levels are lower, corresponding to ranges between 1.5 and 10 μm, and greater than 10 μm, respectively. However, changes in vibrational energy are often accompanied by rotational changes, resulting in closely spaced lines that lead to characteristic spectral lines in the infrared region, called the ro-vibrational bands.

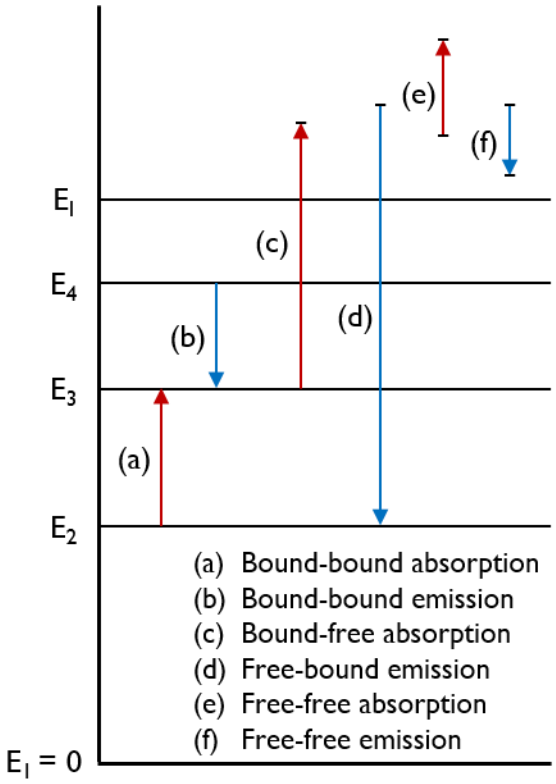

Figure 7: A schematic of molecular energy state transitions. Bound-bound transitions require discrete energy levels for state changes to occur.

Due to the differing structures of molecules, each species has its own absorption profile. As an example, Figure 8 shows the absorption profiles for methane (CH_4), carbon dioxide (CO_2), and nitrogen dioxide (NO_2) between wavelengths of 2.5 and 16.7 μm. Absorption appears in bands due to small ranges of the electromagnetic spectrum that exactly match the energy levels for absorption and emission for those molecules.

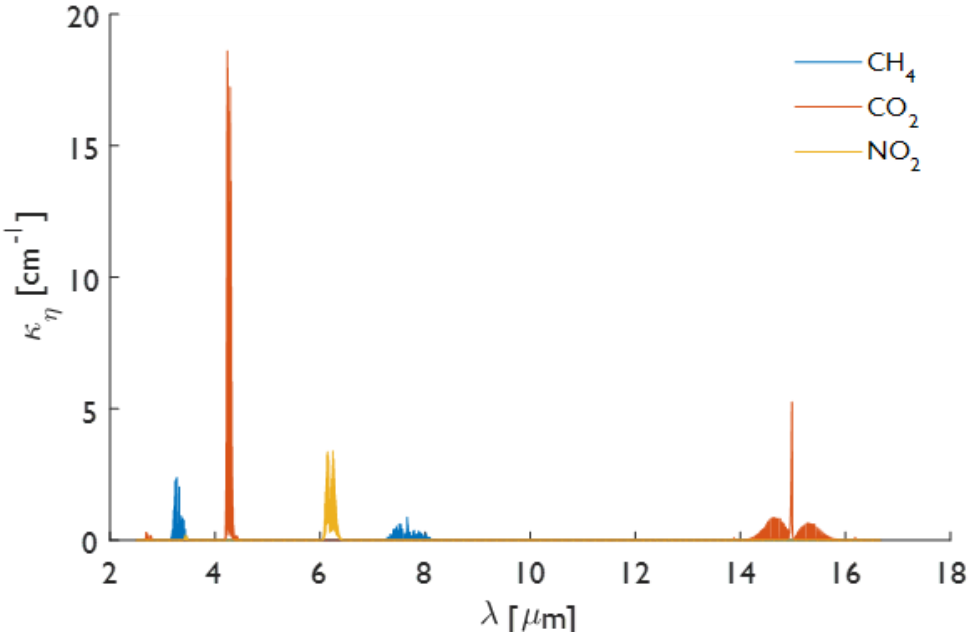

Figure 8: Absorption profiles for methane, carbon dioxide, and nitrogen dioxide across a wide spectrum, derived from the HITRAN database [68]**, appearing in bands at irregular intervals due to individual internal energy levels.**

2.2 Line Absorption by Molecular Gases

As mentioned previously, absorption in the infrared region occurs in discrete lines due to the quantization of energy states of a molecule. These lines are not truly discrete and monochromatic; any significant amount of absorption must occur over a wider spectrum. These spectral lines are broadened through various mechanisms and centered at an energy level corresponding to a wavelength or wavenumber. The most important broadening mechanisms are collision broadening and Doppler broadening, with collision broadening being the most dominant mechanism for most engineering applications involving infrared radiation. Other broadening mechanisms, such as natural broadening and Stark broadening, are only considered in limited cases and are negligible otherwise [69]. As an example, Figure 9 shows the structure of a single broadened line.

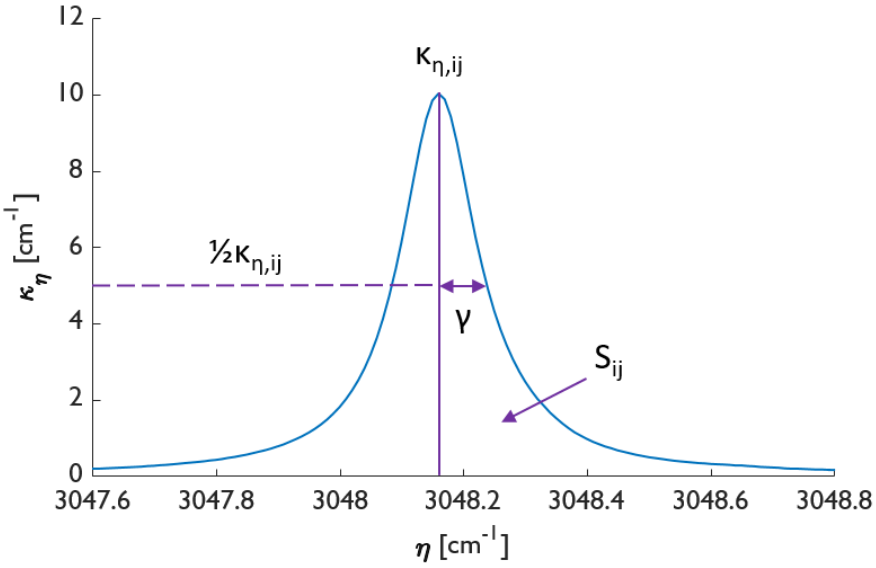

Figure 9: The profile of a single absorption line centered at 3048 cm^{-1}. Absorption lines are characterized by their half-widths, line strengths, and absorption.

This figure shows the absorption coefficient, $\kappa_{\eta,ij}$, centered at a particular wavelength, η_{ij}. The line intensity, S_{ij}, is defined as

$$S_{ij} = \int_0^\infty \kappa_{\eta,ij} d\eta = \int_{-\infty}^\infty \kappa_{\eta,ij} d(\eta - \eta_{ij}) \qquad [2.2]$$

Since the wings of the line approach zero asymptotically as the distance from the centre wavelength increases, the width of the line is described by a half-width, γ. The half-width is half of the width of the line at half of the maximum height, described by $\left(\frac{1}{2}\right)\kappa_{\eta ij}$ in Figure 9.

Collision broadening of a spectral line occurs due to collisions between individual gas molecules. The result of broadening by collisions is a Lorentz profile described by

$$\frac{\kappa_{\eta,ij}}{S_{ij}} = \frac{\gamma_c}{(\eta - \eta_0)^2 + \gamma_c^2} \qquad [2.3]$$

where γ_c refers to the collision half-width. This half-width can be approximated by

$$\gamma_c = \frac{1}{c}\frac{2D^2P}{(\pi MkT)^{\frac{1}{2}}} \quad [2.4]$$

where D is the effective diameter of the molecule, P is the gas pressure, M is the mass of a molecule, and c and k are constants (speed of light and Boltzmann, respectively, $k = 1.381 \times 10^{-23}\ J/K$).

Doppler broadening arises due to the Doppler Effect, in which the velocity of the atoms or molecules of a gas affects the observed wavelength. Doppler broadening produces a line shape described by

$$\frac{\kappa_{\eta,ij}}{S_{ij}} = \frac{1}{\gamma_D}\sqrt{\frac{\ln 2}{\pi}}\exp\left[-(\eta-\eta_{ij})\frac{ln2}{\gamma_D^2}\right] \quad [2.5]$$

where γ_D is the Doppler half-width,

$$\gamma_D = \frac{\eta_{ij}}{c}\left(\frac{2kT}{M}\ ln2\right)^{\frac{1}{2}} \quad [2.6]$$

Natural broadening of a line arises due to Heisenberg's uncertainty principle. The uncertainty in the exact energy levels of the transition energy states contributes to the shape of the line. This shape is known as a Lorentz profile,

$$\frac{\kappa_{\eta,ij}}{S_{ij}} = \frac{\gamma_n/\pi}{\gamma_n^2 + (\eta-\eta_{ij})^2} \quad [2.7]$$

Generally, natural broadening has a minimal overall effect on total absorption, and can be considered negligible.

2.3 Spectral Databases

Large databases containing detailed line absorption information exist for simple molecules. One of the most comprehensive databases is the high resolution transmission (HITRAN) database [68], originally developed by the U.S. Air Force Geophysics Laboratory. As of 2012, the database contains line-by-line parameters at room temperature for 47 different molecules. Some of the parameters include: wavenumber; line intensity; air-broadened width; and self-broadened width. With these values, exact absorption coefficients κ_λ are then obtained by applying the broadening mechanisms

discussed in Section 2.2. However, the database is limited to rather simple molecules such as H_2O, CO_2, O_2, CH_4, etc. As the complexity of molecules increase the viability of performing line-by-line calculations decreases to a prohibitive point. Large molecules (e.g. BTEX) are too large and thus are not included in the HITRAN database.

Fortunately, with high-resolution spectroscopy advances over the last 60 years (e.g. FTIR spectrometers), the strengths of individual lines of these large molecules can be measured. This allows comprehensive empirically-derived databases to be created for many vapour-phase materials. Both the National Institute of Standards and Technology (NIST) and the Pacific Northwest National Laboratories (PNNL) have begun to independently compile extensive libraries. NIST aims to maintain a spectral library of approximately 100 compounds, whereas the PNNL library will contain data for up to approximately 400 compounds [70].

As discussed in Section 1.1, the main species of interest are toluene, methane, and propane. Ethylene was also used to help solve filter specification issues, which will be discussed in Section 4.2. Toluene and propane absorption data are obtained from the PNNL database, while methane and ethylene absorption data are obtained from the HITRAN database. For this reason, methane and ethylene are used as additional baselines to confirm the functionality of the detectors. Shown below are the HITRAN absorption profiles for methane and ethylene, and the PNNL absorption profiles for toluene and propane.

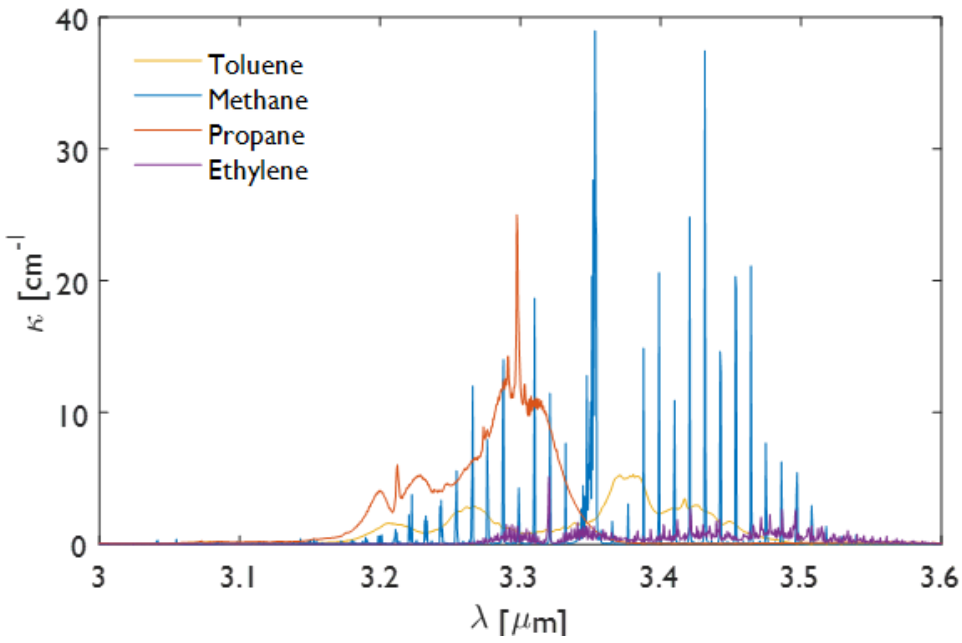

Figure 10: Scaled absorption coefficients of the ro-vibrational bands for toluene (C_7H_8), methane (CH_4), propane (C_3H_8), and ethylene (C_2H_4), obtained from the HITRAN database [68].

2.4 Monochromatic Absorption Tomography

As stated in Section 1.4, absorption tomography is an imaging technique used to estimate chemical distributions. In traditional absorption tomography techniques, measurements of the flow field are carried out at monochromatic wavelengths. The physical model stems from the radiative transfer equation (RTE), which is an equation that describes the radiative flux incident on a surface or the flux at any point inside a participating medium, which may emit, absorb, or scatter radiation [71]. The RTE is an energy balance such that the change in spectral radiative intensity along a line of sight $\hat{\boldsymbol{s}}$ is described by

$$\frac{dI_\eta}{ds} = \kappa_\eta I_{b\eta} - \kappa_\eta I_\eta - \sigma_{s\eta} I_\eta + \frac{\sigma_{s\eta}}{4\pi} \iint_{4\pi} I_\eta\,(\hat{\boldsymbol{s}}_i)\Phi_\eta(\hat{\boldsymbol{s}}_i, \hat{\boldsymbol{s}})d\Omega_i \qquad [2.8]$$

where the terms on the right-hand side of the equation represent the emission, absorption, scattering away from $\hat{\boldsymbol{s}}$, and incoming scattering, respectively. For infrared applications, the emission and

scattering terms are negligible, which reduces the significant terms in the RTE to only absorption, $-\kappa_\eta I_\eta$. Integrating the RTE over the field of interest yields the Beer-Lambert law,

$$I_{\eta L} = I_{\eta 0} \exp\left[-\int_0^L \kappa_\eta(s)ds\right] \quad [2.9]$$

which describes the intensity that would be measured across an absorbing medium ($I_{\eta L}$) based on the intensity entering the domain ($I_{\eta 0}$) and the spectral absorption coefficient (κ_η). The spectral absorption coefficient is proportional to the species local mole fraction, χ, which is related by the equation

$$\kappa_\eta = \sigma_\eta N = \sigma_\eta \frac{\chi(s)P}{R°T} \quad [2.10]$$

where σ_η is the molecular absorption cross-section, N is the molecular number density, P is the pressure of the species, T is the temperature, and $R°$ is the universal gas constant.

Equation [2.9] can be rearranged to the form of a Volterra integral of the first kind (IFK)

$$b \equiv \ln\left(\frac{I_{\eta 0}}{I_{\eta L}}\right) = \int_0^L \kappa_\eta(s)ds \quad [2.11]$$

where b is the path-integrated absorption coefficient along the measurement path. As discussed previously, CST aims to reconstruct the distribution of κ_η. This is done by first discretizing the domain, usually into an array of square pixels, in which each pixel is assumed to have a uniform concentration (see Figure 11 for an example). Estimates of the pixel concentrations are stored in a vector of coefficients $\mathbf{x} \in \mathbb{R}^{nx1}$. Multiple measurements of b are to be stored in a vector $\mathbf{b} \in \mathbb{R}^{mx1}$, where m is the number of paths in the measurement domain. As a result, Equation [2.11] can be estimated by a ray-sum

$$b_i \approx \sum_{j=1}^{n} a_{ij}x_j \quad [2.12]$$

where a_{ij} is the length of the i^{th} path intersecting the j^{th} pixel shown in Figure 11. Combining the ray-sums for each path forms a ray-sum matrix $\mathbf{A} \in \mathbb{R}^{mxn}$. This matrix forms the linear system

$$\mathbf{Ax} = \mathbf{b} \qquad [2.13]$$

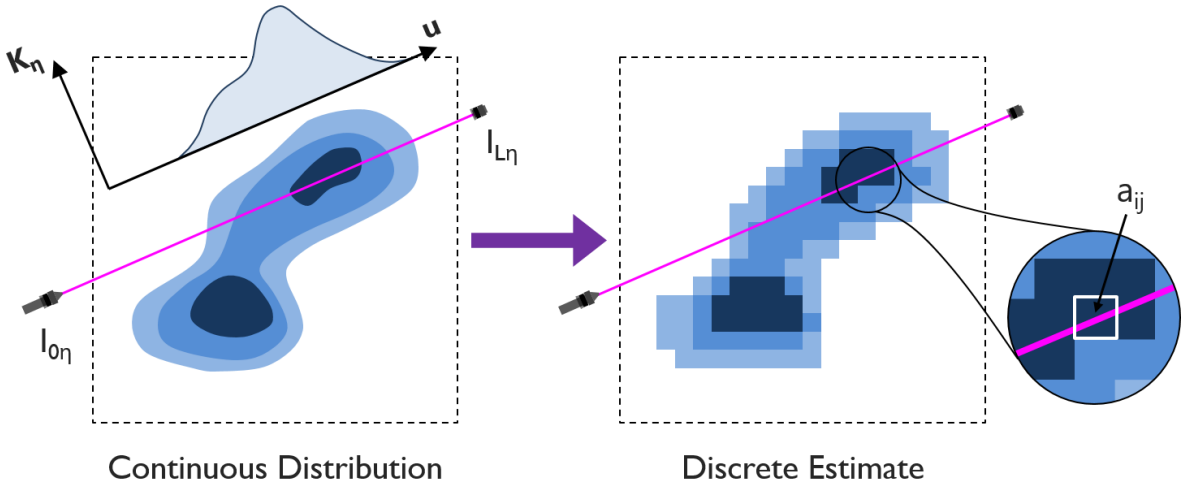

Figure 11: Discretization of a chemical species tomography problem with construction of the ray-sum matrix.

In order for the assumption of uniform species concentration within each pixel to hold, the size of the pixels must be small. Due to the nature of CST problems and a limited number of beams m, the system is under the condition $m < n$, making the system rank-deficient according to the rank-nullity theorem. For a full-rank problem, the linear system can usually be solved directly through matrix inversion (i.e. $\mathbf{x} = \mathbf{A}^{-1}\mathbf{b}$). This is not the case for the CST problem, which is known to be mathematically ill-posed [72]. Well-posed problems, originally outlined by Jacques Hadamard [73], have the following characteristics:

1) The problem has a solution,

2) The solution to the problem is unique, and

3) The solution is stable to perturbations in the measurement data.

Problems that violate the third criterion for stability are known as discrete ill-posed problems. CST problems of this nature are those in which dense sampling is possible, but the solution is unstable due to the amplification of measurement noise in the deconvolution process. However, rank-deficient

problems violate the second criterion for uniqueness, as the limited number of measurements in **b** can be explained by any number of distributions **x**.

2.4.1 Bayesian Framework

Since CST problems often feature incomplete or insufficient information, Bayesian priors can be used to add sufficient information. The goal of applying Bayesian statistics to CST is to maximize the posterior probability density function (pdf) which is formally given by Bayes' equation

$$\pi(\boldsymbol{x}|\boldsymbol{b}) = \frac{\pi(\boldsymbol{b}|\boldsymbol{x}) \cdot \pi_{Pr}(\boldsymbol{x})}{\pi(\boldsymbol{b})} \quad [2.14]$$

where $\pi(\boldsymbol{x}|\boldsymbol{b})$ is the posterior PDF of $\boldsymbol{x}$ given measurement data $\boldsymbol{b}$, $\pi(\boldsymbol{b}|\boldsymbol{x})$ is the likelihood pdf, $\pi_{Pr}(\boldsymbol{x})$ is a prior pdf of $\boldsymbol{x}$, and $\pi(\boldsymbol{b})$ is the evidence. The evidence is a scaling factor, and thus it can be neglected for the purposes of this problem. Consequently,

$$\pi(\boldsymbol{x}|\boldsymbol{b}) \propto \pi(\boldsymbol{b}|\boldsymbol{x}) \cdot \pi_{Pr}(\boldsymbol{x}) \quad [2.15]$$

The reconstruction for most CST applications is obtained through the maximum *a posteriori* (MAP) estimate, $\boldsymbol{x}^{MAP} = \text{argmax}\,[\pi(x|b)]$, which requires the likelihood function and a prior distribution.

Measurement noise of the system is due to photonic shot noise and electronic noise. Combined, the noise follows a Gaussian distribution and can be modelled as an independent and identically distributed term [74]. The likelihood pdf can then be described by the following expression,

$$\pi(\boldsymbol{b}|\boldsymbol{x}) = \frac{1}{2\pi\sigma_m^2} \exp\left[-\frac{1}{(2\sigma_m^2)^{\frac{n}{2}}}(\boldsymbol{A}\boldsymbol{x}-\boldsymbol{b})^T(\boldsymbol{A}\boldsymbol{x}-\boldsymbol{b})\right] \quad [2.16]$$

where σ_m is the standard deviation of the noise. Since **A** is rank-deficient, there is insufficient information to provide a unique solution.

The prior pdf, $\pi_{Pr}(\boldsymbol{x})$, represents information that is known about the target species distribution. Concentration data can be modelled as a joint-normal random variable $\boldsymbol{x} \sim \mathcal{N}(\overline{\boldsymbol{x}}, \boldsymbol{\Gamma_x})$, where $\overline{\boldsymbol{x}}$ is the mean distribution and $\boldsymbol{\Gamma_x}$ is the spatial covariance of the flow. The prior pdf then looks like:

$$\pi_{Pr}(\boldsymbol{x}) = \frac{1}{\sqrt{(2\pi)^n |\boldsymbol{\Gamma}_{\boldsymbol{x}}|}} \exp\left[-\frac{1}{2}(\boldsymbol{x}-\bar{\boldsymbol{x}})^T \boldsymbol{\Gamma}_{\boldsymbol{x}}(\boldsymbol{x}-\bar{\boldsymbol{x}})\right] \quad [2.17]$$

Combining Equations [2.15], [2.16], and [2.17] yields the expression

$$\pi(\boldsymbol{x}|\boldsymbol{b}) \propto \exp\left[\left\|\begin{bmatrix}\sigma_m \boldsymbol{A} \\ \boldsymbol{L}\end{bmatrix}\boldsymbol{x} - \begin{bmatrix}\sigma_m \boldsymbol{b} \\ \boldsymbol{L}\bar{\boldsymbol{x}}\end{bmatrix}\right\|_2^2\right] \quad [2.18]$$

where $\boldsymbol{L}$ is the Cholesky factor of the inverse covariance matrix, $\boldsymbol{L} = \text{chol}(\boldsymbol{\Gamma}_{\boldsymbol{x}}^{-1})$. Knowing that species concentration, as a physical property, can only be a positive value adds an additional prior. Equation [2.19] can be minimized with a non-negativity constraint for the MAP estimate:

$$\boldsymbol{x}^{MAP} = \min_{x>0}\left[\left\|\begin{bmatrix}\sigma_m \boldsymbol{A} \\ \boldsymbol{L}\end{bmatrix}\boldsymbol{x} - \begin{bmatrix}\sigma_m \boldsymbol{b} \\ \boldsymbol{L}\bar{\boldsymbol{x}}\end{bmatrix}\right\|_2^2\right] \quad [2.19]$$

The covariance matrix, which describes how a basis function correlates with other basis functions, can be estimated through the use of simulations or published variance data [74]. If neither option is viable, it can be assumed that the flow is spatially smooth using first-order Tikhonov regularization [75] with a regularization parameter $\lambda = 0.20$.

2.5 Broadband Absorption Tomography

The procedure outlined in Section 2.4 is a basic approach for monochromatic sources. For broadband sources, a more complicated approach must be developed due to the fact that κ_η is highly variable over a spectral broadband width, as discussed in Section 2.2. Additionally, the intensity of a broadband source varies as a function of the spectrum, which is given by Planck's law,

$$I_{b\lambda}(\mathrm{T},\lambda) = \frac{2C_1}{\lambda^5\left[e^{\frac{C_2}{\lambda T}} - 1\right]} \quad [2.20]$$

or

$$I_{b\eta}(T,\eta) = \frac{2C_1\eta^3}{e^{\frac{C_2\eta}{T}} - 1} \quad [2.21]$$

depending on the use of wavelength or wavenumber. C_1 and C_2 refer to constants, where $C_1 = hc_0^2$ and $C_2 = hc_0/k$. The constant h is Planck's constant and k refers to Boltzmann's constant. Figure 12 shows the intensity of a blackbody at various temperatures.

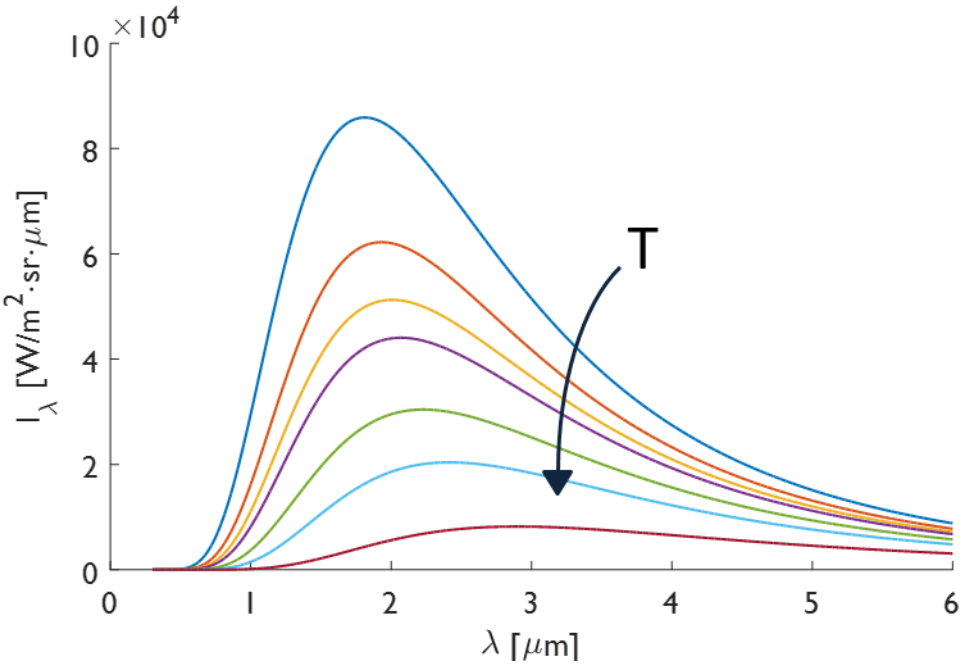

Figure 12: Blackbody intensity profiles at decreasing temperatures (1600, 1500, 1443, 1400, 1300, 1200, and 1000 *K*).

For a single broadband optical path, a broadband transmittance can be calculated by taking the ratio of the attenuated incident power on the detector through an absorbing medium to an incident reference power of the detector (i.e. incident power that has not been attenuated),

$$T = \frac{P_{abs}}{P_{ref}} \qquad [2.22]$$

where P_{abs} is given by

$$P_{abs} = \int_{\eta_{1-2}} C_g f_\eta \epsilon_\eta I_{\eta 0} \exp\left[-\int_0^L \kappa_\eta(s) ds\right] d\eta \qquad [2.23]$$

In this equation, C_g refers to a configuration factor that is influenced by geometric considerations; f_η is the photovoltaic detector efficiency; ϵ_η is the emissivity of the broadband source; $I_{\eta 0}$ is the intensity produced by the blackbody source; and κ_η is the local absorption coefficient. The intensity at the spectrum of interest (i.e. η_{1-2}) does not vary significantly and can be treated as constant. The intensity, along with the other constants, can be grouped together as another coefficient, C_{e-d}, and removed from the integrand

$$P = C_{e-d} \int_{\eta_{1-2}} \exp\left[-\int_0^L \kappa_\eta(s)ds\right] d\eta \quad [2.24]$$

The reference power can be similarly expressed, noting that the power is a measurement with no absorption occurring (i.e. $\kappa_\eta = 0$),

$$P_{ref} = C_{e-d} \int_{\eta_{1-2}} \exp\left[-\int_0^L \kappa_\eta(s)ds\right] d\eta = C_{e-d}\Delta\eta_{1-2} \quad [2.25]$$

The constants for both measurements are identical and thus cancel out when determining the transmittance, yielding

$$T = \frac{1}{\Delta\eta_{1-2}} \int_{\eta_{1-2}} \exp\left[-\int_0^L \kappa_\eta(s)ds\right] d\eta \quad [2.26]$$

Since this broadband transmittance is a nonlinear function of the path-integrated concentration, additional manipulation is required to estimate the concentration distribution [74].

Photonic absorption events are independent, and line strength is related linearly to the partial pressure of the species of interest. As such, the absorption coefficient can be expressed as a product of the local concentration, $c_i(s)$, and a spectral shape function, C_η

$$\kappa_\eta = c_i(s) \cdot C_\eta \quad [2.27]$$

This relationship holds up under most conditions of constant temperature and pressure when the self-collision and air-collision broadened half-widths are not significantly different. Equation [2.27] can then be substituted into Equation [2.26]:

$$T = \frac{1}{\Delta\eta_{1-2}} \int_{\eta_{1-2}} \exp\left[- \int_0^L c_i(s) ds \right]^{C_\eta} d\eta \quad [2.28]$$

The exponential term can be replaced with a function G,

$$G(L) \equiv - \int_0^L c_i(s) ds \quad [2.29]$$

which results in the transmittance equation,

$$T = \int_{\eta_{1-2}} \frac{\exp[-G(L)]^{C_\eta}}{\Delta\eta_{1-2}} d\eta \quad [2.30]$$

The transmittance can be calculated for a species with a known spectral shape function over a specific range. The inverse of G, which is also known as a linearizing transfer function, can be related to the path-integrated measurement of the target species,

$$b_i \equiv G(L) = G^{-1}(T) \quad [2.31]$$

At this point, the methods outlined in Section 2.4 employed for estimating the concentration, including the Bayesian framework, can be applied to broadband tomographic reconstructions due to the shared forms of Equations [2.11] and [2.29].

Chapter 3
Broadband Optical Path Design

As has been discussed previously, one of the main challenges in CST is the high number of optical paths needed for high quality reconstructions, due to the high cost of commercial open path detectors as well as lasers. This chapter describes the design and manufacture of open path detector pairs used to carry out chemical species tomography.

3.1 Original Design

The initial concept for a low-cost infrared open path hydrocarbon gas detector was designed by a group of mechatronics engineering students (Nick Bodd, Ali Jahed, Shari King, and Peter Robertson) as part of their capstone MTE 481/482 design project at the University of Waterloo [76]. The scope of the project, which this thesis builds upon, was to design an open path detector that scales to multiple measurements, built under a budget of $8,000, operates under a fail-to-safe mode, and that is field-deployable. A field-deployable requirement suggests that the units be portable (i.e. lightweight, easy to maneuver, and allows for flexibility in arrangement) and housed in a casing suitable for operation in a Class I, Div. I location (i.e. a location in which flammable gases are present at all times). This requires that the casing and selected components be either intrinsically safe or explosion-proof. In Canada, intrinsically safe equipment meets the CSA C22.2 NO. 157-92 standard [77] while explosion-proof enclosures meet the CSA C22.2 NO. 30-M1986 standard [78]. The original design included a detector and emitter pair, each unit mounted in an Adalet explosion-proof case and mounted on an adjustable tripod.

Initial considerations for the emitter included infrared LEDs, lasers, xenon flash lamps, and thermal emitters. The criteria upon which each emitter type was judged were available wavelength, intensity, cost, collimation, safety, and field depth. Overall, the thermal source was judged to best satisfy these criteria. Although lasers are often the source of choice in spectroscopic applications due to their high intensity, collimation, and specific spectral range, the safety hazards that they present make this option much less desirable.

Considerations for detectors included photovoltaic, photoresistive, and photoconductive. The criteria used to judge detector options were wavelength, sensitivity, and cost. A photovoltaic detector was deemed to be most appropriate based on the weighted criteria.

Other aspects of the project that required consideration included telemetry, casings, mounts, and optical elements. Key components are listed in Table 2 and a model of the final prototype design can be seen in Figure 13.

Table 2: Summary of selected design components for an open path detector prototype.

Item	Manufacturer	Model/Item Number
Photovoltaic detector	Hamamatsu	P10090-01
Infrared source	Hawkeye Technologies, Inc.	IR-Si253
Telemetry	Omega Omega	UWTC-REC1 UWPC-2-NEMA
Optical components	Spectrogon Thorlabs, Inc.	BP-1695-097 LA5370-E
Power supply	Power Patrol Tenma	SLA 1022 72-630
Housing	Adalet	XDHLDGCX

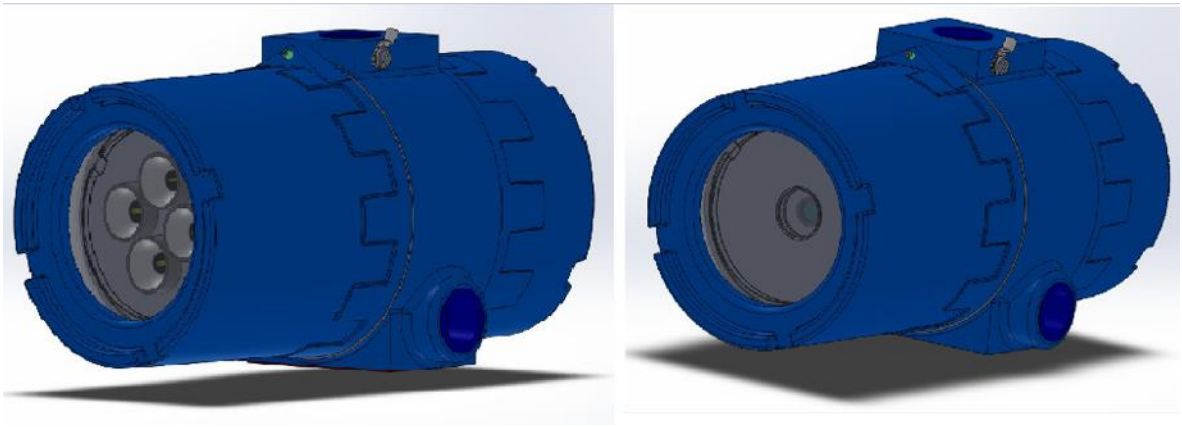

Figure 13: Rendering of original prototype design of the detector and emitter pair [76].

3.1.1 Emitter Specifications

The IR-Si253 emitter by Hawkeye Technologies, Inc. is a thermal infrared emitter made of silicon nitride. This emitter was chosen for both its recommended operating parameters and expected performance. The recommended operating parameters can be seen in Table 3.

Table 3: Summary of the Hawkeye Technologies Inc. IR-Si253 thermal emitter.

Parameter	Specification
Voltage, V	12.0
Current, A	1.6
Temperature, K	1443
Power, W	20.0
Emissivity, %	80

Being a thermal emitter, it is expected that the IR-Si253 behaves akin to that of a greybody operating at a temperature of 1170 $°C$ (1443.15 K). The spectral intensity of a blackbody is given by Equation [2.20] (or Equation [2.21] if working in wavenumber). The blackbody emission of the emitter is shown in Figure 14 with absorption lines of methane for comparison. The emitter was originally selected for its peak emission, which occurs near the weak overtone absorption band for hydrocarbons centred at approximately 1.6 μm. This band is highlighted in the following figure.

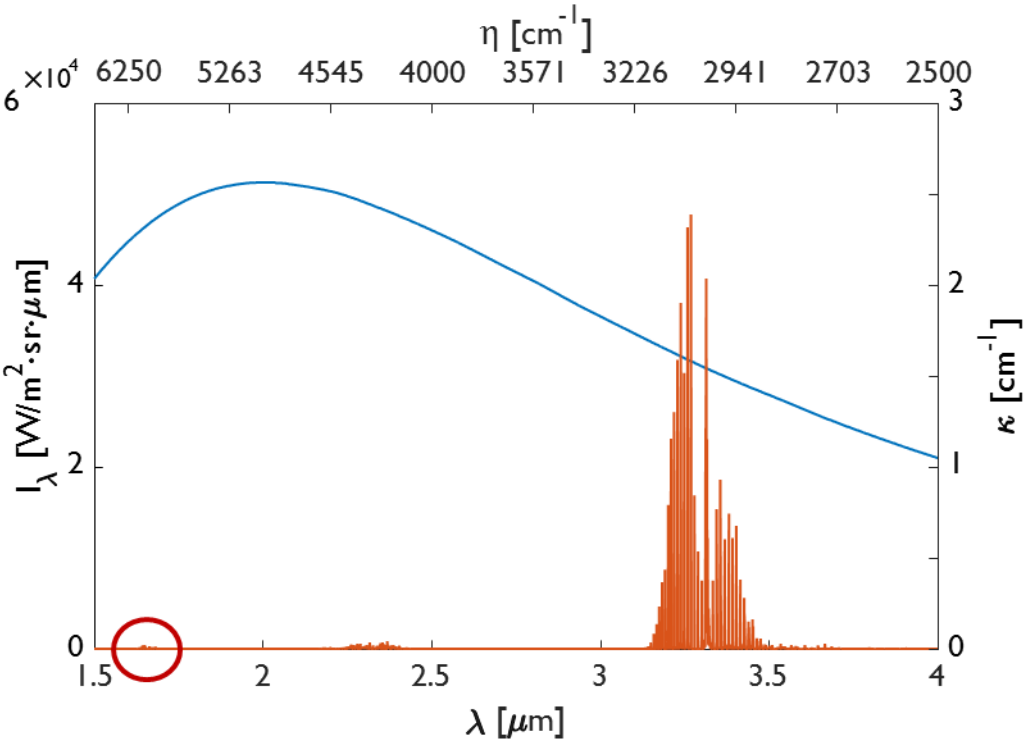

Figure 14: Blackbody intensity profile for the IR-Si253 with methane absorption profile between λ = 1.5 and λ = 4.0 *μm*.

3.1.2 Power Supply

The emitter specifications recommend a power supply that outputs 1.6 *A* at 12 *V*. Originally, 12 *V* sealed lead acid batteries were chosen for portability for each emitter unit. The selected battery has a capacity of 2.9 *Ah* and physical dimensions of 7.0 x 9.0 x 10.1 *cm* (width x length x height) that enables it to sit behind the emitter in the casing. Lab-based experiments and later tomography experiments used a Tenma 72-630 DC power supply, which offers variable output voltage of 1-15 *V* and a maximum current output of 30 *A*. Photographs of each are shown in Figure 15.

(a) (b)

Figure 15: Photographs of sealed lead acid battery (a) and DC power supply (b) used to power thermal emitter source.

The change from batteries to the wall power supply for tomography experiments was made due to the nature of voltage drops of batteries as the charge decreases. Initially it was not thought to be a problem but experimental results, displayed in Figure 16, indicate otherwise. Shown is a comparison of signals received from the emitter unit when powered by a battery vs. the wall supply. Due to the decaying nature of power from the battery, the dedicated wall supply was used for all tomography experiments beyond experiment #5, discussed in Chapter 5.

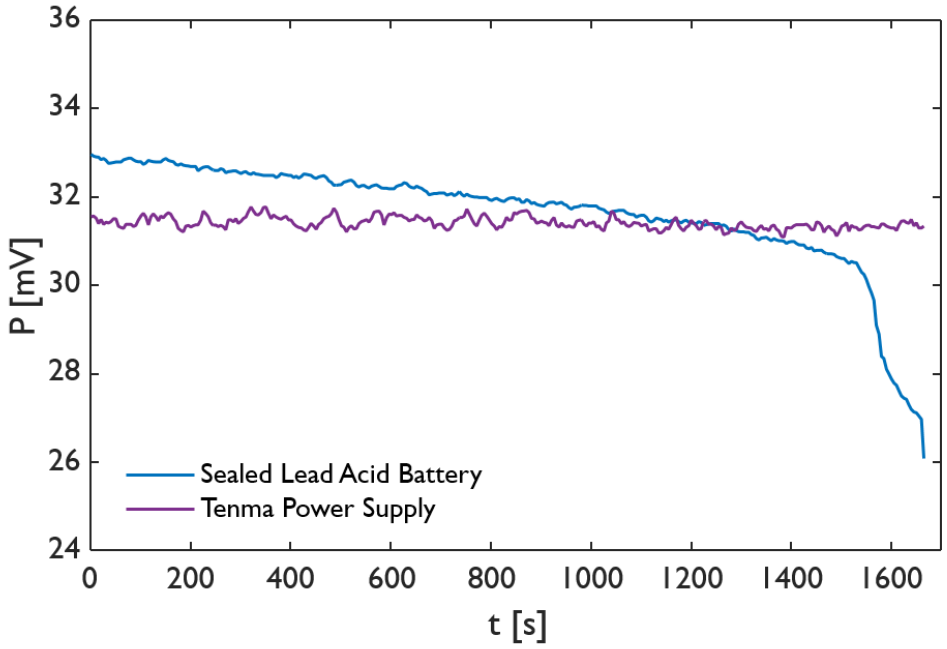

Figure 16: Power supply comparison test of sealed lead acid battery to Tenma wall power supply.

3.1.3 Detector Specifications

The detector, a Hamamatsu P10090-01 detector, is a non-cooled indium arsenic (InAs) detector capable of detecting infrared light with a peak sensitivity wavelength of 3.35 μm, making the detector an ideal choice for focus on hydrocarbon absorption in the mid-infrared region.

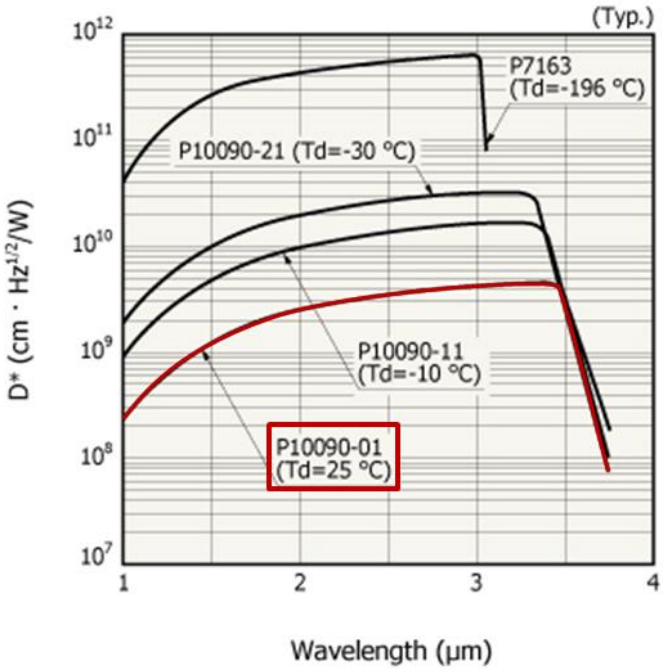

Figure 17: Detector spectral profiles for P10090-01 and other Hamamatsu InAs photovoltaic detectors.

3.1.4 Lens and Filter Specifications

The focusing lens used in the receiver side, the ThorLabs LA5370-E, is a 1-*inch* plano-convex lens made of calcium fluoride (CaF_2), with a focal length of 40 *mm*. The lens has an anti-reflective coating optimized for the range of 3 to 5 μm, while uncoated CaF_2 has a spectral transmission range from approximately 0.18 to 8.0 μm.

The filter selected for the original prototype was the Spectrogon BP-1695-097, which is a filter centered at 1,695 *nm* with a half-width of 100 *nm*. This filter corresponds to the weak overtone absorption band of hydrocarbons. However, subsequent design decisions were made such that the greater line strengths of the ro-vibrational band could be taken advantage of by considering other filters.

The first filter considered was the ThorLabs FB3250-500, which has a sapphire substrate mounted in an aluminum ring. The centre wavelength is located at 3.250 μm with a full width half-maximum of 0.5 $\pm$ 0.1 μm. This filter is an integral component as it contains the spectral range for absorption of the C–

H band. The second filter that was briefly considered and used was the ThorLabs FB2750-500 filter. With a centre wavelength of 2.750 μm, this filter would serve as a transparent window of hydrocarbon absorption, and therefore measurements made with this filter would be used as reference measurements (i.e. Equation [2.25]). Although some methane spectral lines exist in this region, they are few and low in intensity and would not impact experimental measurements in any appreciable manner. However, this filter was ultimately only tested briefly over a few tomography experiments because the absorption band for H_2O lies within this filter window and reduces the effectiveness of the reference measurements due to the variable levels of relative humidity of the air at the time of measurements.

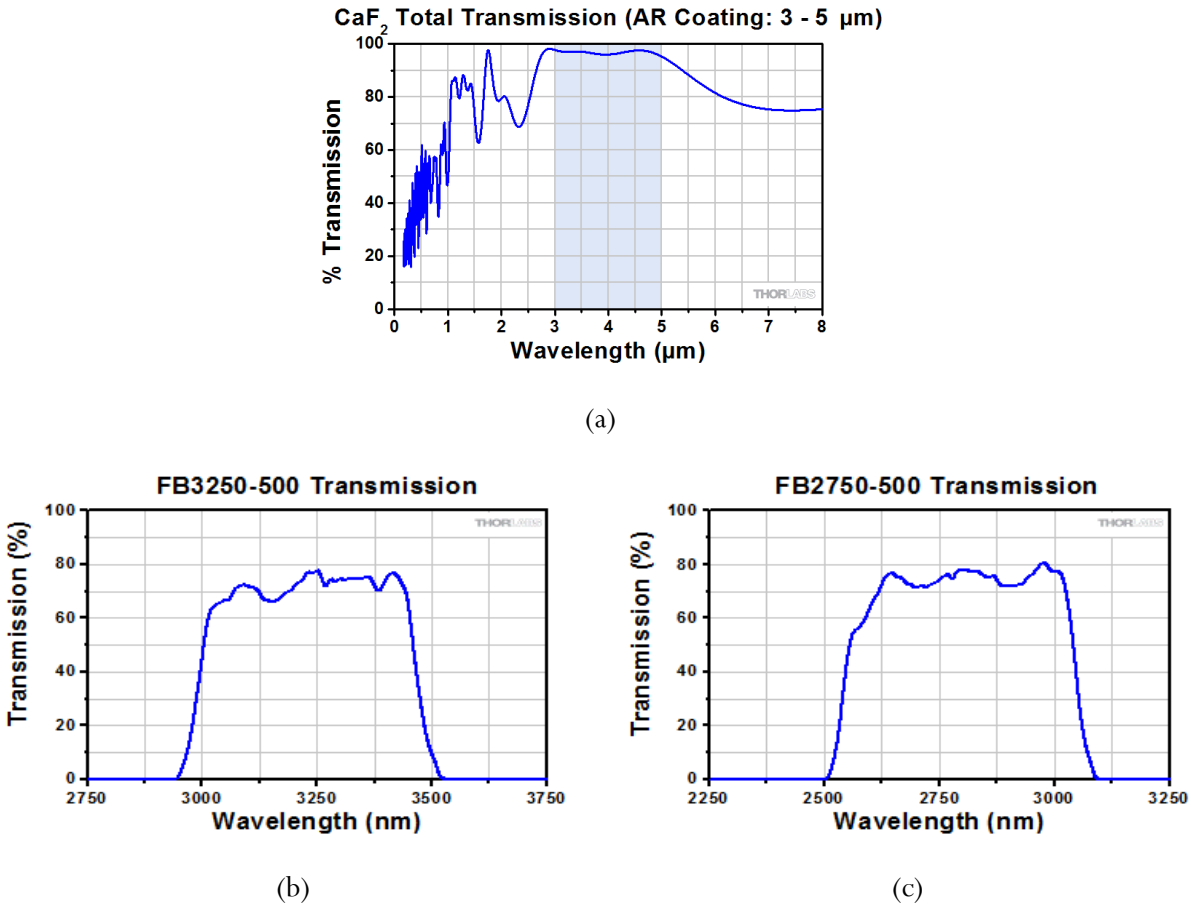

Figure 18: Transmissivity profiles for ThorLabs optical components (LA5370-E, FB3250-500, FB2750-500) [79].

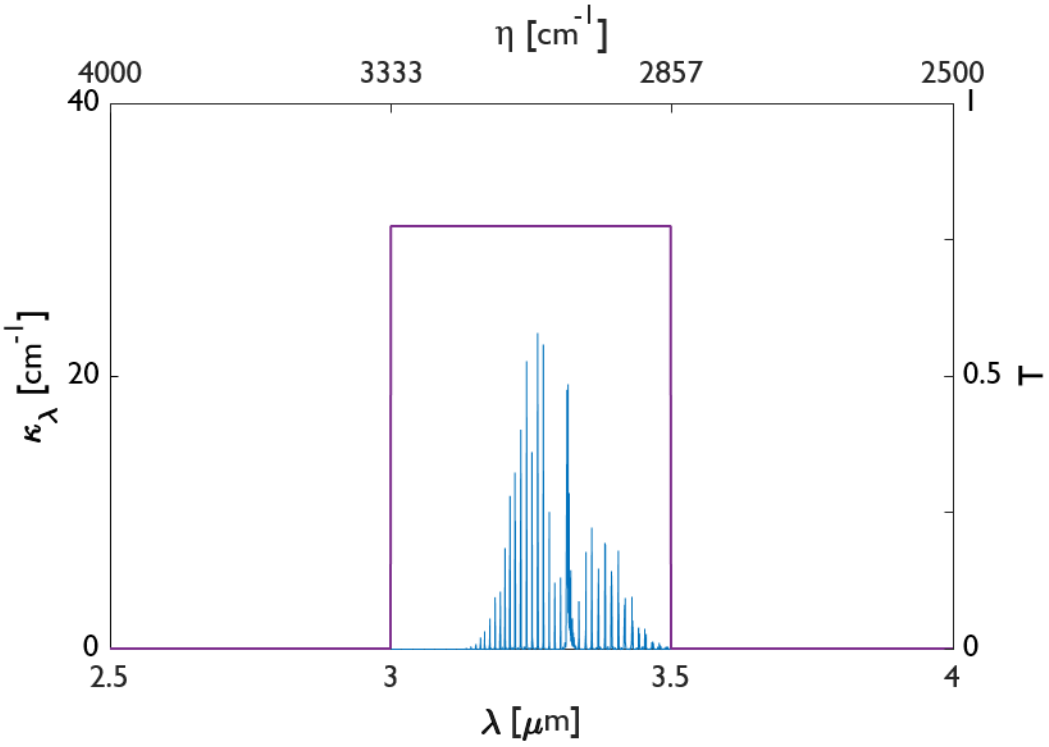

Figure 19: Absorption coefficients for methane with an ideal FB3250-500 box model filter.

3.2 Design Modifications

Several modifications needed to be made to the original design due to multiple issues regarding performance and efficiency. The major issue was that the performance of the optical transmitter-receiver pair was very poor. There was very little detectable signal above distances of 2 m as well as poor detection of absorption, therefore changes were made to improve performance. To improve detection of absorption signals, it was decided that the 3.3 μm ro-vibrational band be used due to the higher absorption coefficients. As a result, the Adalet explosion-proof cases were set aside because the soda-lime glass on the cases drop the transmissivity of infrared light to approximately 40% beyond wavelengths of 2.8 μm. For this reason, meeting the Class I Division I requirement was one that was put off to be revisited at a future time.

To improve the working performance of the open-path detector, three aspects were targeted: emitter placement, emitter collimation, and alignment. The emitter placement and collimation issues

were solved by using a Monte Carlo ray-tracing simulation to select a larger parabolic reflector, while the alignment issue was solved by developing an aligning laser.

3.2.1 Monte Carlo Ray-tracing Simulation

After reducing the transmitter unit to a single, centered thermal emitter, performance over longer distances was still poor. To quantify and visualize the behavior, a Monte Carlo method was used. A Monte Carlo simulation is one in which a randomized sample is simulated repeatedly to obtain a result [69], [71]; in this case, photon bundles (radiation) from the thermal emitter were simulated to obtain the view factor, or the frequency of photon bundle hits on the target.

To simulate this scenario, MATLAB® is used to reconstruct the geometry of the emitter, reflector, and target surface. The emitter element is 5 *mm* in length and 1 *mm* in diameter, while the reflector is 10.0 *mm* in length and 9.0 *mm* by 25.4 *mm* at the smaller and larger diameters at the ends. The simulation parabola can be constructed using these measurements of the reflector, and the centre of the emitter element is placed at the focal point of the parabola. The target surface is a 25.4 *mm* surface, representing the focusing lens used in the design, at a set distance defined from the front face of the parabola to the target surface. Due to symmetry, the problem can be simplified to a half-parabola in 2D space, displayed in Figure 20.

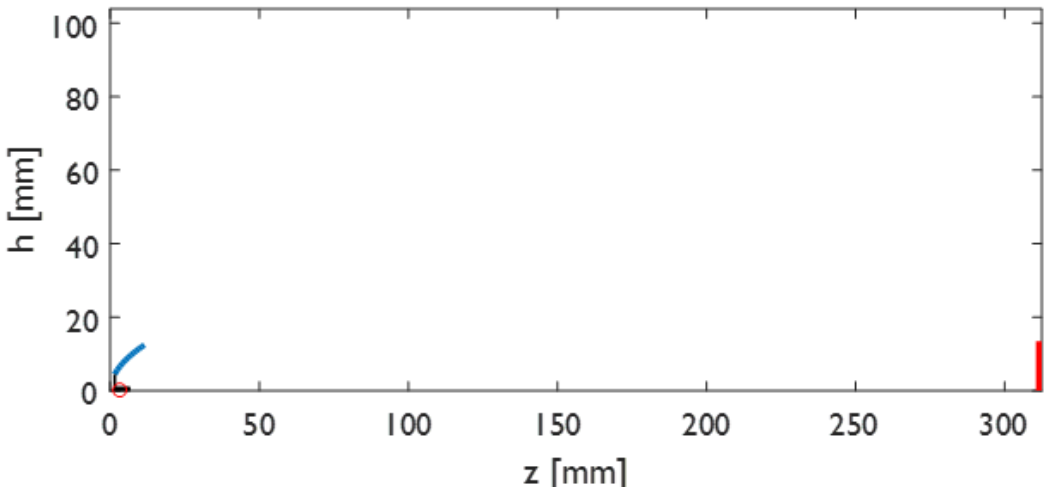

Figure 20: Base configuration of the Monte Carlo ray tracing simulation. Components present are the emitter filament (black, circled in red), parabolic reflector (blue), and optical target (red) at a distance of 300 *mm*.

An emission location on the filament surface is chosen at random, and a photon is emitted in a random direction. The filament is modelled as a diffuse emitter so the emission direction follows a Lambertian distribution. To quantify the performance of the reflector, the view factor is defined as the ratio of photons that strikes the target surface to the total number of photons released:

$$F = \frac{\sum_i^s \left(\frac{N_{strike}}{N}\right)_i}{s} \quad [3.1]$$

A simulation of N = 10,000 photons with a distance of 10 *m* to the target surface over s = 20 trials shows that the view factor of the stock IR-Si253 parabolic reflector is F = 0.0025, or 0.25%. An example of the simulation with N = 50 photons can be seen in Figure 21.

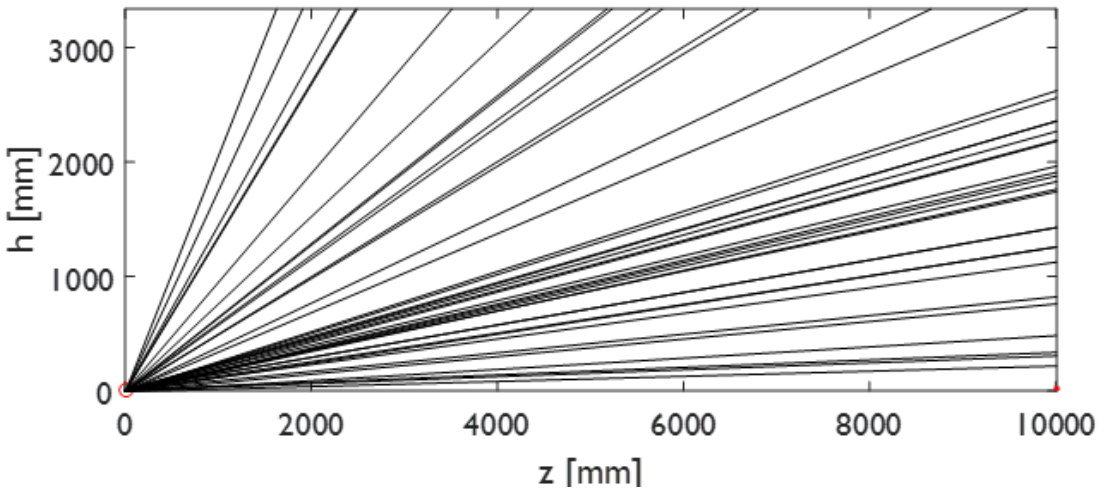

Figure 21: Sample results of the Monte Carlo ray tracing simulation for the IR-18 parabolic reflector. Shown are 50 rays across a distance of z = 10 *m*.

As the simulation shows, the performance of the stock reflector is inefficient, with few to no rays reaching the target. Due to the length of the filament in relation to the size of the reflector, a large portion of the radiation leaving the filament is not captured by the reflector, illustrated by the large number of rays that reach the top axis of the figure. The proposed solution is to use a larger reflector in the design. Phoenix Electroformed Products, Inc. offers a large array of stock reflectors with varying dimensions, their offerings categorized in series by focal length ranging from 0.055" to 3.000" (1.40 *mm* to 76.2 *mm*).

Although many reflectors have similar performance, only reflectors with a diameter $d_2 < 4.0$" (10.2 *cm*) can be considered due to space constraints in the tubes that are used for mounting the components. Out of the stock reflectors that Phoenix Electroformed Products, Inc. offers, the reflector that performed best according to the simulation was the PA10.2. Under comparable conditions to the simulation of the IR-18, the PA10.2 has a view factor of F = 0.0106, or 1.06%.

The simulation showed better collimation by the PA10.2 reflector than the IR-Si253 stock reflector. Figure 21 and Figure 22 illustrate this performance for the IR-Si253 and PA10.2 reflectors, respectively. Photons reflected by the PA10.2 have a much narrower spread towards the direction of the target than those reflected by the IR-Si253.

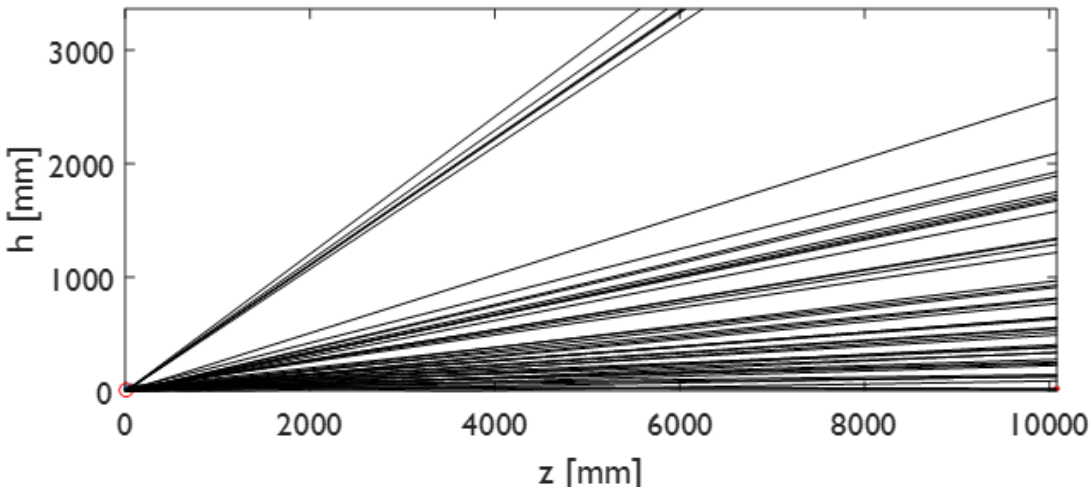

Figure 22: Sample results of the Monte Carlo ray tracing simulation for the PA10.2 parabolic reflector. Shown are 50 rays across a distance of z = 10 m.

Comparative results for simulated as well as experimental results can be seen in Figure 23. The solid lines indicate simulation results that are associated with the N_{targ}/N_{emit} axis, while the dashed lines indicate experimental results that are associated with the *Detector Response* axis. The purple series represents IR-Si253 reflector results, while the blue series represents PA10.2 reflector results. Figure 23 does not directly compare the simulated and experimental results, but rather displays the improvement in simulated results from using the IR-Si253 to the PA10-2 that is reflected in the experimental results.

It is clear from these results that the PA10.2 reflector results in a higher absolute signal as well as collimation that is not provided by the IR-18 reflector. A separate test was done to confirm that the emitter-detector pair was operational over 10 *m*, confirming that the PA10.2 provides sufficient collimation for large-area CST measurements.

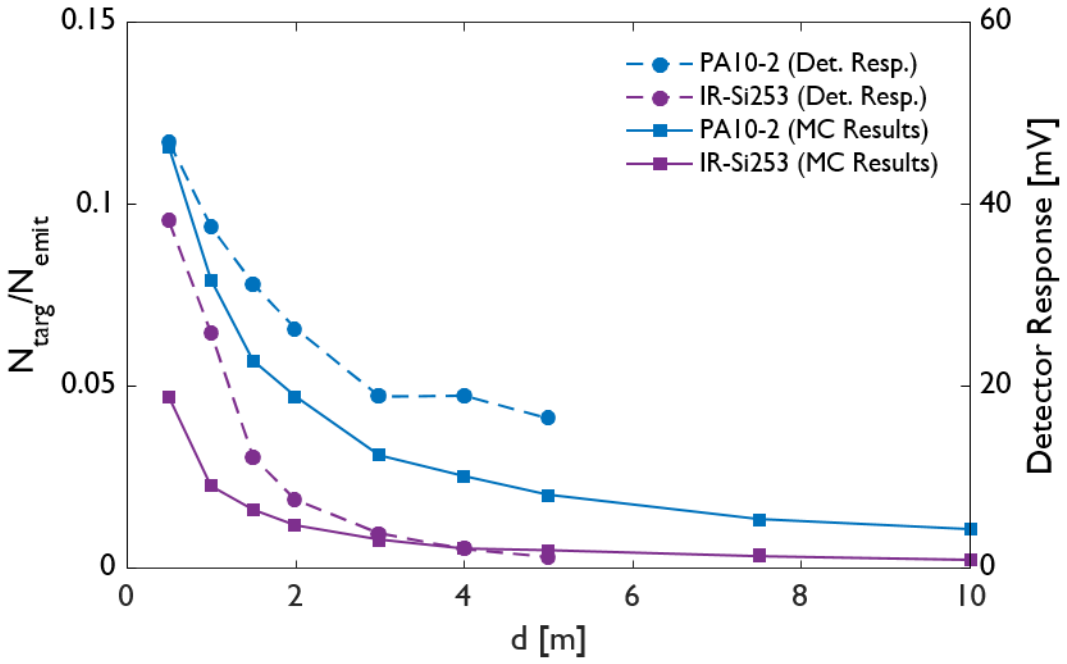

Figure 23: Simulated (solid lines) and experimental (dashed lines) comparisons of stock IR-18 and PA10.2 parabolic reflectors.

3.2.2 Visible Laser Alignment

Alignment of the emitter and the detector units is done with a low-powered optical laser on the emitter side with a basic mirror on the detector side. The laser is mounted at the centre of the emitter unit and pointed at the centre of a mirror mounted on the detector side. The detector unit can then be pointed directly to the emitter unit by reflecting the optical laser point to its source. This ensures that alignment of both units is achieved.

The laser used is a Quarton VLM-650-03 LPA red dot laser, which has a centre wavelength of 650 nm. With an output power of $< 5\ mW$, it is classified as a Class IIIa laser. Due to imperfections, the laser point is directed at a slight angle. This can be seen when the laser is shone at a far wall and rotated in place. To combat this, a custom mount is made to hold the laser at a slight offset. The mount uses three set screws, set 120° apart, to adjust the direction angle. Adjustments are made until the laser points at a single spot on the far wall while it is rotated. Figure 24 shows the laser mounted in place.

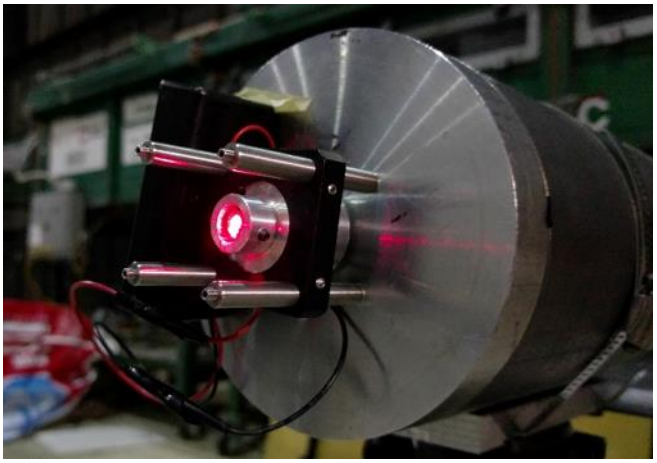

Figure 24: Mounted visible red laser alignment device.

3.2.3 Data Acquisition System

The Omega UWPC-2-NEMA unit was originally set to transmit a signal every five seconds, with a maximum sampling rate every two seconds. For the final tomography experiment (discussed in Section 5.2.6), a National Instruments USB-6001 data acquisition (DAQ) unit was chosen for use in order to achieve a higher sampling rate that would allow for statistical measurement analysis. Consequently, an amplifier was also required for the signal, discussed in the next subsection.

3.2.4 Detector Amplification

Based on experimental results, the output range of the photovoltaic detector fell in the sub-50 mV range. However, the specifications of the DAQ state the absolute accuracy of the unit at 6 mV and the system noise at 0.7 $mVrms$. This is problematic as the accuracy and inherent system noise make up a large portion of the uncertainty of the experimental transmissivity measurements. As such, an amplifier is required to minimize this uncertainty. The amplifier selected was the Texas Instruments LM358 dual operational amplifier to achieve a gain of 50. The amplifier unit received input from the photovoltaic detectors and output its signal to the NI USB-6001. A photograph of the amplifier unit can be seen in Figure 25.

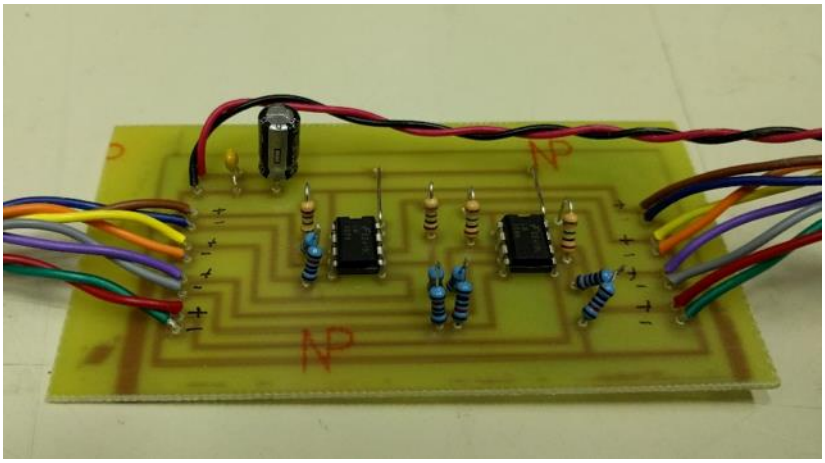

Figure 25: Photograph of the amplifier unit to improve photovoltaic detector signals.

3.3 Optical Paths Expansion

Incorporating the updated design details three more beams were constructed. Drawings of the individual components can be seen in Appendix A.

In expanding the number of optical paths other minor design details were changed. Optical components are mounted on the front faces of the detector plates, using ThorLabs cage system construction rods. Where the original prototype used steel pipes to house the emitter and detector assemblies, steel tubes were instead chosen for use in the new constructed units. The main reason for using tubes over pipes is primarily due to one reason: the pipes have a weld bead on the inside that is not present on the tubes. As a result, the new assemblies are slightly smaller due to the way that pipes and tubes are specified (inner diameter vs. outer diameter). While the weld beads can be ground off (as they were for the original prototype), the decision was made to size the new components appropriately to fit tubes and forego the additional step.

Chapter 4
Device Calibration and Characterization

To ensure that the fabricated prototypes function as designed, they were tested using an absorption cell. The purpose of an absorption cell is to hold a well-defined gas mixture consisting of an inert gas and an absorbing target while an absorption measurement is made through the cell. Absorption cells are commercially available for small path lengths, typically on the order of 1 *cm*, to be used with a small, focused source (e.g. diode lasers). The open-path detectors outlined in Chapter 3, by contrast, are designed for a large scale operation, and therefore require a custom cell. This chapter presents the design of the absorption cell and experimental procedures and results of the necessary device validation.

4.1 Absorption Cell Calibration

4.1.1 Cell Design and Purpose

The cell, designed and built by Antoni Pashartis, an M.Eng. student in the Department of Mechanical and Mechatronics Engineering at the University of Waterloo, is shown in Figure 26. Built from black steel plumbing pipes and caps, the cell has an approximate length of 81 *cm* and a volume of 7.0 *L*. The cell has 1.5" (38.1 *mm*) sapphire windows in each cap on the ends. Sapphire is used because it is spectrally transparent in the mid-IR. The cell features three ¼" NPT-threaded ports to be used as inlets, outlets, or for measurement devices. In the case of a liquid species, (e.g. toluene), the species can be placed in the cell's bottom cap.

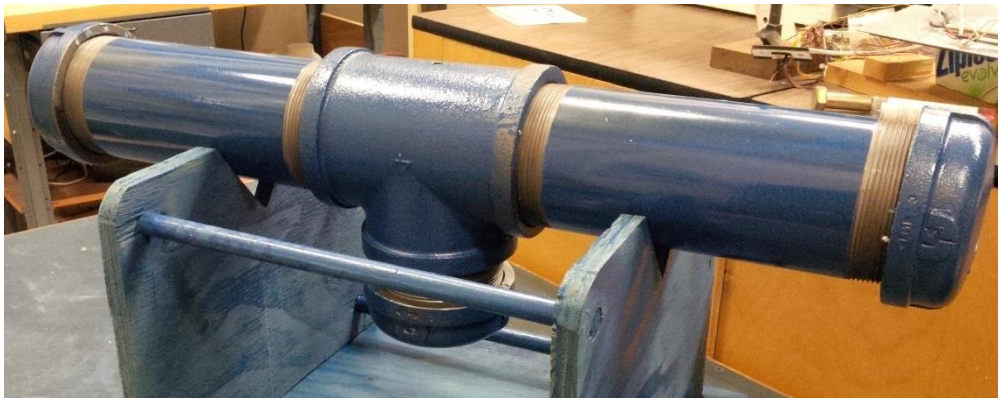

Figure 26: Custom absorption cell fabricated from steel piping components with 1.5" sapphire windows and three ports to be used as inlets or outlets to the cell.

4.1.2 Experimental Calibration

For all experiments, the absorption cell was placed in the centre of the testing table, with the source and detector at opposite ends, 1.9 *m* apart. The emitter was powered by a Tenma DC power supply, set to provide a constant 12.0 *V*.

4.1.2.1 Toluene Procedure and Results

Toluene absorption measurements required assistance from Imperial Oil Inc. A flame-ionizing detector (FID) was needed to determine the concentration inside the cell while simultaneously making absorption measurements of the detector. The FID is a ThermoScientific TVA-1000 model, which infers organic compound concentrations by measuring the ions produced from a combustion reaction of a hydrocarbon air sample in hydrogen flame.

To capture the full range of toluene concentration, the measurements of toluene absorption were done in two separate tests. The first toluene test, which was intended to measure high concentrations of toluene, saw 50 *mL* of liquid toluene placed inside the absorption cell and left for 24 *h* to reach phase equilibrium within the cell. Incident intensity measurements at the detector were taken at 20 *s* intervals in conjunction with point measurements from the FID. These point measurements required an air sample to be pulled from the cell on a continual basis. Sampling consistency was established by simultaneously drawing the sample from the end ports of the cell.

The second toluene test, which was meant to measure attenuation at low concentrations, began following the first test after purging the cell. Measurements began immediately upon placing the liquid toluene inside the cell. Attenuation and concentration were measured as the vapour concentration increased over time; the procedure for the measurements was identical to the first test.

Results from validation measurements in conjunction with a theoretical model constructed from spectral data are shown below in Figure 27. Toluene results show two curves that represent each individual test. Clean air FID measurements between the two tests measured non-zero, indicating a slight set point drift throughout the first test. This drift accounts for the minor discrepancy in transmittances for the region of burden overlap.

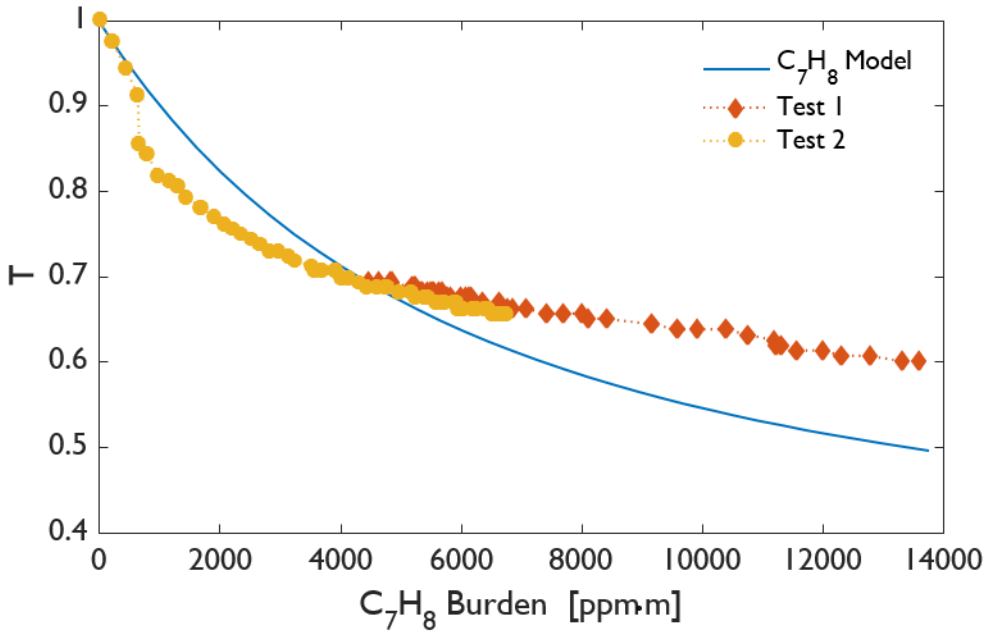

Figure 27: Toluene transmittance measurements through the absorption cell for the prototype emitter-detector pair with simultaneous FID readings, compared to a simulated transmittance model derived from spectral absorption reported in the PNNL database [70].

Upon inspection the measured trends generally follow the trends projected from database values. The normalized root-mean-square error (NRMSE) for toluene is 14.9%, with measured transmittance at higher concentrations of toluene larger than expected. The crossing of experimental and expected

data in the results suggests additional errors exist with the toluene experiments. Potential sources include:

1) PNNL absorbance data for toluene is specified at a burden of 1 ppm·m, which is extrapolated up to the 14,000 ppm·m observed during the experiments.
2) Experimentally, FID concentration measurements were also subject to extrapolation: manufacturer-provided response factor data, which are needed to convert FID readings to concentrations, are only available up to 104 ppm.
3) The FID, drawing a continuous feed of air from the cell, causes an inhomogeneity in the gas concentration, introducing further uncertainty.
4) Finally, the stated accuracy of the TVA-1000 FID is ±25% of the reading up to 104 ppm.

All of these factors significantly impact the analysis for toluene. While it is encouraging that the detector-emitter pair successfully detects the presence of toluene, the experimental procedure including the FID is not completely robust. Following construction of additional optical path pairs for tomography measurements, methane was chosen as the species of choice for further calibration study. As a gas, the proportions within the cell are more easily controlled, and it is a species included in the HITRAN database.

4.1.2.2 Methane Procedure and Results

For the calibration of optical paths using methane as a species, the amount is known by way of controlling the inlet flow to the cell. Methane is introduced into the cell at a known flow rate, the proportions balanced by mixing the input with an additional nitrogen flow.

Tests conducted using methane through the absorption cell progressed in two distinct steps. In the first step, the flow of nitrogen was kept steady while the rate of methane was increased incrementally to capture absorption measurements at low concentrations. In the second step, the methane concentration was held constant while the nitrogen flow was reduced incrementally until the flow entering the cell was purely methane. The calibration test was done to confirm the effectiveness of the initial prototype emitter-detector setup against the absorption data given by the HITRAN database for methane.

Additional sets of calibration tests were performed after additional beam pairs were constructed to confirm consistency between each other.

Each test began with an initial measurement made with an empty cell (i.e. no methane) to provide a reference power value, P_{ref}. Mass flow controllers (MFCs, Brooks Instrument SLA-5850S) were used for prototype testing, while rotameters were used for the additional pairs, to control the flows of methane and nitrogen into the cell. The mass flow controllers are originally calibrated for nitrogen and hydrogen, so a conversion factor based on the specific heats of gases are used for converting the flow rate from a hydrogen calibration to methane flow.

Detector voltages were recorded under steady-state conditions of the gases in the cell at predetermined mixture fractions. A test was performed to approximate the time required for steady-state conditions, seen in Figure 28. In this test, the cell was set to an initial concentration of 3.69% CH_4 and left until the detector signal appeared to be steady. The methane flow rate was then increased such that the mixture fraction was 7.76% CH_4 with absorption measurements taken every 20 *s*. For an approximate absorption cell volume of 7.0 *L*, it is expected that at a fill rate of 1.09 *L/min* the cell concentration will stabilize in 6.42 *min*. However, the results show that the signal appears to stabilize after approximately 900 *s*, or 15 *min*.

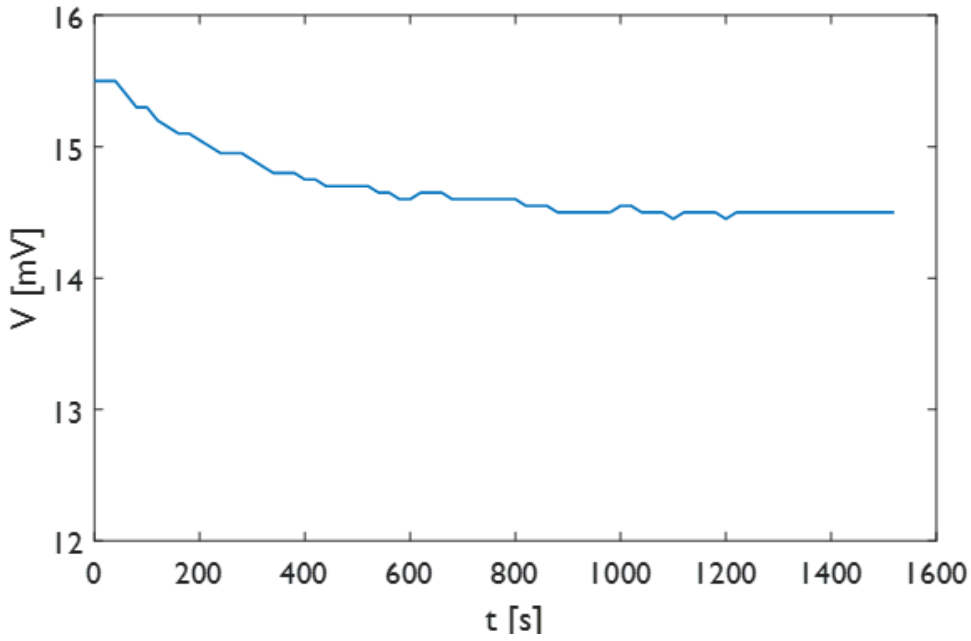

Figure 28: Experimental results through the absorption cell to determine time required for steady state conditions when changing cell concentration level.

Using HITRAN absorption data for methane, the expected transmittance values at varying volume fractions for the spectral range of interest can be calculated using Equation [2.30], which is shown alongside the measured transmittances in Figure 29 for the prototype, and Figure 30 for the additional constructed emitter-detector pairs.

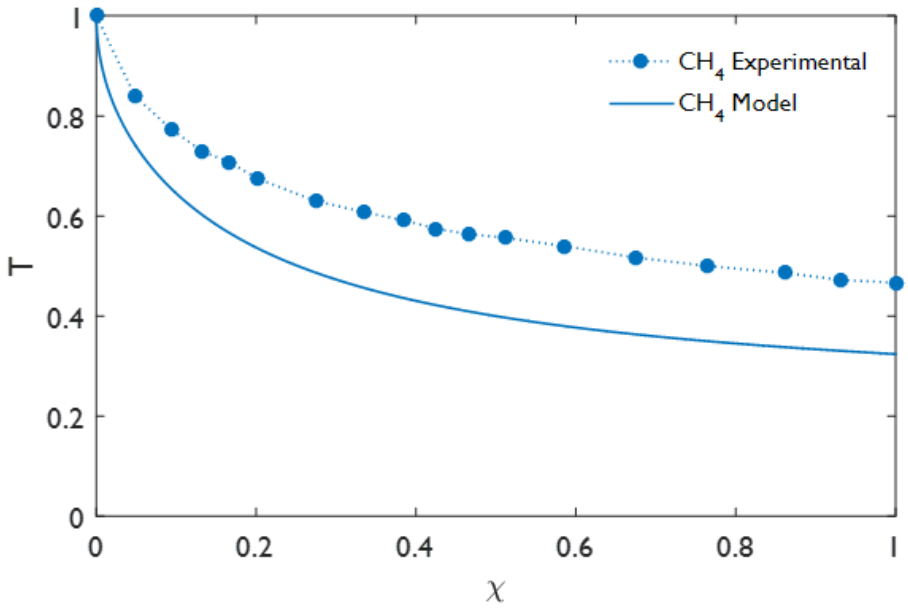

Figure 29: Methane transmittance measurements through the absorption cell for the prototype emitter-detector pair, compared to an expected transmittance model derived from HITRAN database absorption.

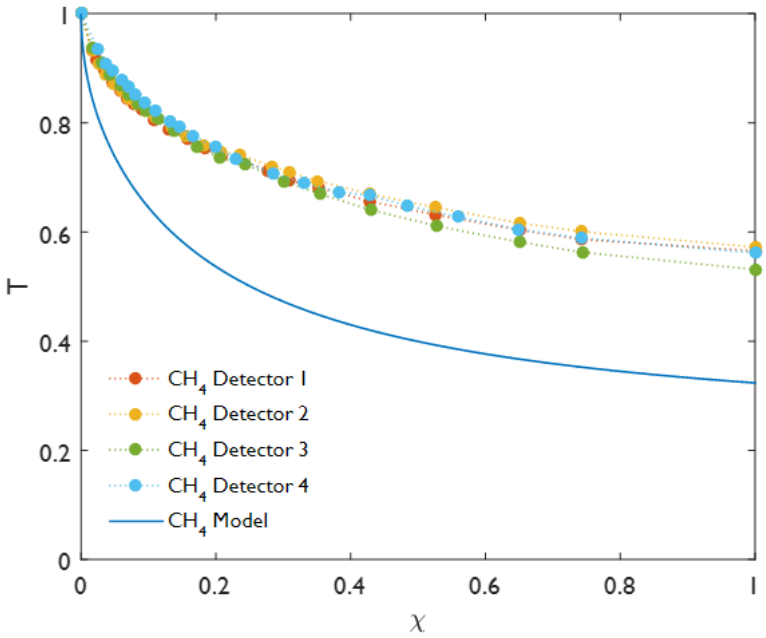

Figure 30: Transmittance measurements for the additional constructed emitter-detector pairs with expected transmittance.

As the results show, the measured readings for all units recorded a transmittance that was higher than expected. The model results were gathered by numerical integration of the absorption coefficients across the spectral window specified by the filter specifications (wavenumbers between 3333.33 and 2857.15 cm^{-1}, corresponding to wavelengths of 3.0 and 3.5 μm). The measurements show that the general trend of absorption follows the expected curve, but the values of actual absorption show a discrepancy when compared to the modeled line, resulting in a NRMSE of 14.0% for the prototype.

The NRMSE for the detectors shown in Figure 30 are 18.7%, 19.6%, 18.2%, and 20.2%. Another related issue is that the measured transmittance varies between detectors. This is most apparent at 100% methane, where the transmittance for detectors varies between 0.531 and 0.573. Initially, the difference was erroneously attributed to various factors, such as the experiment being highly non-repeatable, or effects arising due to backwards placement of one filter.

While the cause of the discrepancy issue went unsolved for a period of time, Section 4.2 describes the discrepancy issue and the solution in greater detail.

4.1.2.3 Ethylene and Propane Procedures and Results

Calibration experiments were also carried out on ethylene and propane as a part of solving the discrepancy issue as well as allowing for using these gases as part of tomographic experiments for reconstruction. Absorption data for ethylene and propane are discussed and shown in Section 2.3.

The calibration procedures for these gases are similar to the procedure used for calibration with methane, with the only major difference coming in the instrumentation for flow control. Rather than use mass flow controllers, rotameters (Cole Parmer N034-39 and N102-05) were used because the MFC flow rates were too low for both ethylene and propane. Additionally, the procedures were carried out only on one open path device. Results can be seen in Figure 31. The errors between the model and experimental data are 5.24% and 9.00% for ethylene and propane, respectively. Similar to the results for methane, less absorption was measured than was predicted by the model.

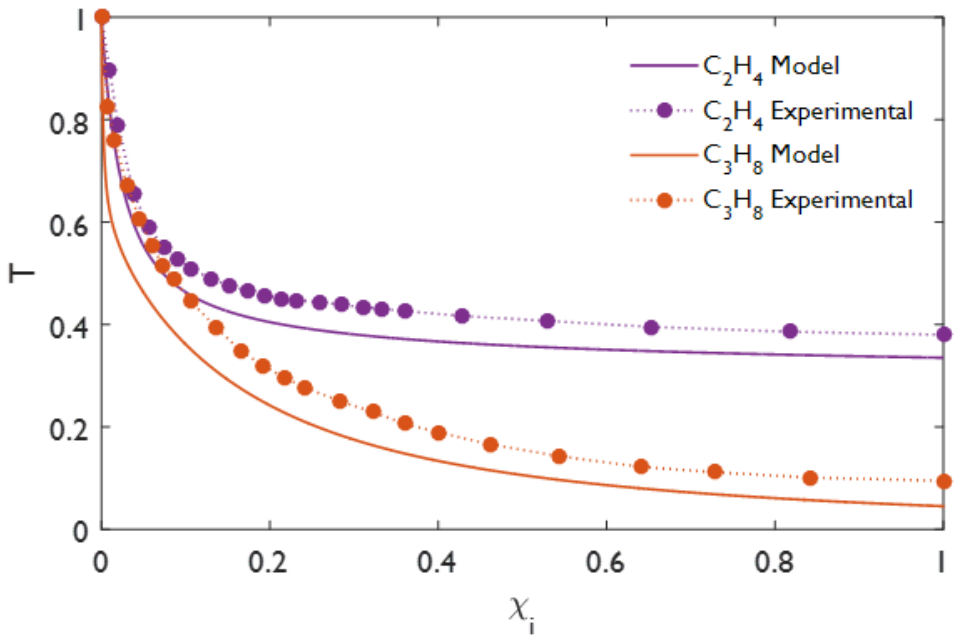

Figure 31: Transmittance measurements for ethylene and propane compared to model transmittances for each species.

4.2 Filter Bandwidth Specification

As mentioned previously, the specification for a ThorLabs filter is denoted by its name, with the major number indicating its centre wavelength and the minor number denoting its half-width. In this case, the FB3250-500 is centered at 3.25 μm and has a bandwidth of 0.5 μm. Under these circumstances, the filter will transmit light that ranges between 3.0 and 3.5 μm. However, the stated tolerances for these values are ± 0.1 μm. Accounting for specification tolerances, the filter may potentially have an actual range that includes spectrum from 2.8 to 3.7 μm, which is problematic for several reasons: any deviation from the assumed filter specification will affect the model parameters selected; and the complexity of the system increases because each path will have a separate spectral profile.

In order to try to determine the actual limits of the filters used in the 4 constructed emitter-detector pairs, the filters were measured using a Surface Optics SOC-400 FTIR reflectometer machine. As a reflectometer, the FTIR did not directly measure the filter transmissivity, but instead measured the

reflectance of the filter. In this way, the measured reflectance of a filter would indicate the spectra at which material changes of the substrate would occur, which would correspond with the spectral ends of the filter bandwidths. Figure 32 shows the FTIR measurements obtained, illustrating that the actual filter bands are shifted slightly from the ideal specifications. A summary of estimated half-maximum filter end locations are listed in Table 4.

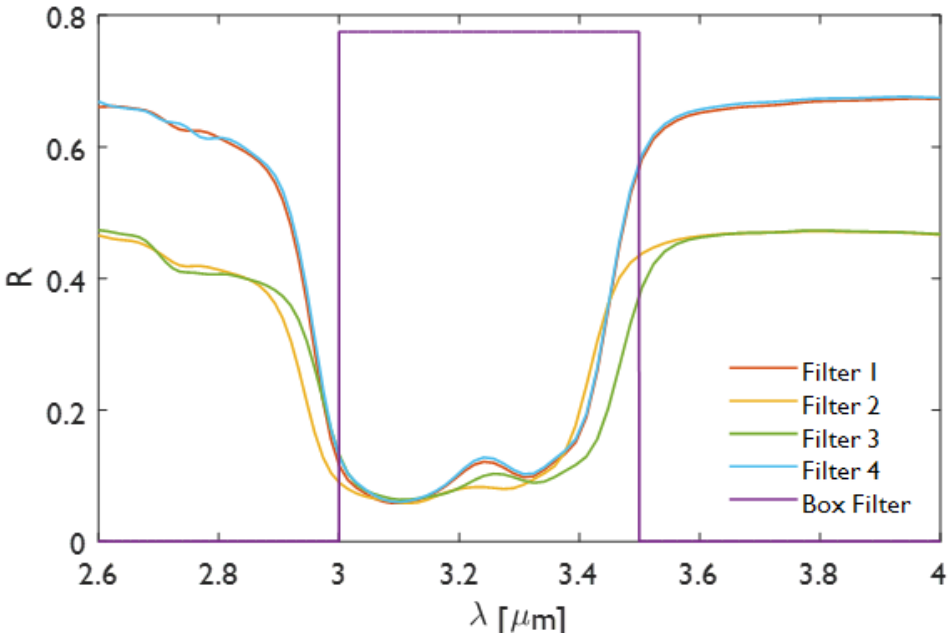

Figure 32: FTIR spectrometer reflectance measurements of each filter, compared to a box filter of expected performance based on manufacturer specifications.

Table 4: Summary of estimation of filter window ends based on FTIR reflectance measurements.

Filter	λ_{min} (μm)	λ_{max} (μm)	η_{min} (cm^{-1})	η_{max} (cm^{-1})
1	2.945	3.450	3396	2899
2	2.932	3.419	3411	2925
3	2.958	3.467	3381	2958
4	2.948	3.450	3392	2899

Based on the estimations of the filter ends, the four filters used for the detectors have an average bandwidth of 0.501 μm, which is within the specification provided by ThorLabs. The centre

wavelengths of the filters are then estimated to have an average placement at 3.196 μm, which places it just outside of the specified tolerance of $\pm 50\ nm$, with only filter #3 being located within tolerance ($CWL_3 = 3.213\ \mu m$). However, since these are only estimations of the filter bandwidths based on reflectance measurements, it is reasonable to assume that the filters are within specification, but albeit potentially at the high end of the limits.

Unfortunately, minor deviations in the positioning of the filter's spectral window have significant impacts on the transmittance models used (e.g. Figure 29). Looking at the absorption coefficients for a hydrocarbon of interest, methane in particular, it can be seen that the majority of absorption occurs well within the window with a small amount of the band appearing at the edge of the window (see Figure 19). This can be illustrated more clearly as an issue when absorption lines are compared to box filters constructed with the filter window ends of the measured filters, shown in the next figure. A small shift in the window placement results in a number of significant absorption lines being cut out. As a result, the model would predict a lower transmittance due to a greater amount of absorption than is actually occurring. If the models shown in Figure 29, Figure 30, and Figure 31 are set to account for the shift in filter positioning, then a closer agreement is seen between the model and experimental results, shown in Figure 34. The error between the measured data and models for methane, ethylene, and propane were 2.71%, 4.10%, and 4.94%, respectively, compared to errors of 14.0%, 5.24%, and 9.00% discussed in Sections 4.1.2.2 and 4.1.2.3.

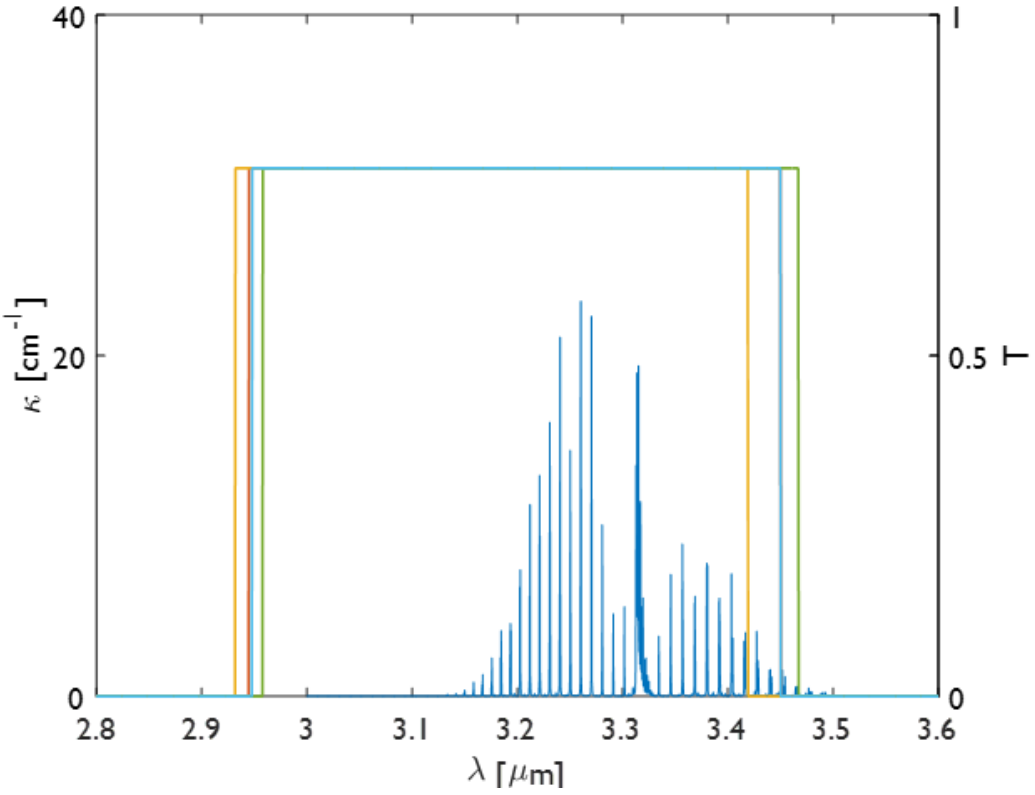

Figure 33: Box filters constructed with estimated spectral end locations of each filter compared to absorption coefficients of methane.

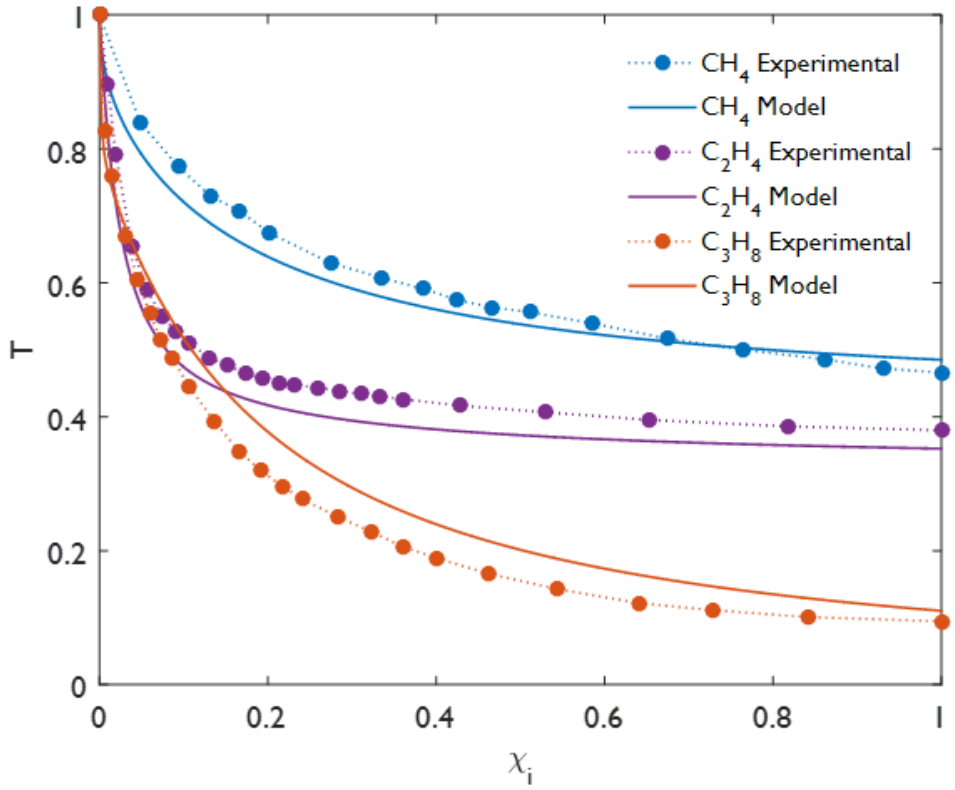

Figure 34: Adjusted model transmittance curves for corresponding estimated filter profile.

Developing accurate filter bounds can be taken a step further with a nonlinear regression between modeled and measured transmittance data [74]. This regression results in an optimal filter that is centered at $\eta_c = 3163\ cm^{-1}$ ($\lambda_c = 3.162\ \mu m$) with a width of 522.7 cm^{-1} (0.525 μm). This filter was used to build the transfer functions $G^{-1}(T)$, shown in the following figure. This function relates the transmittance that is measured by the open-path detectors to a path-integrated concentration of the species of interest.

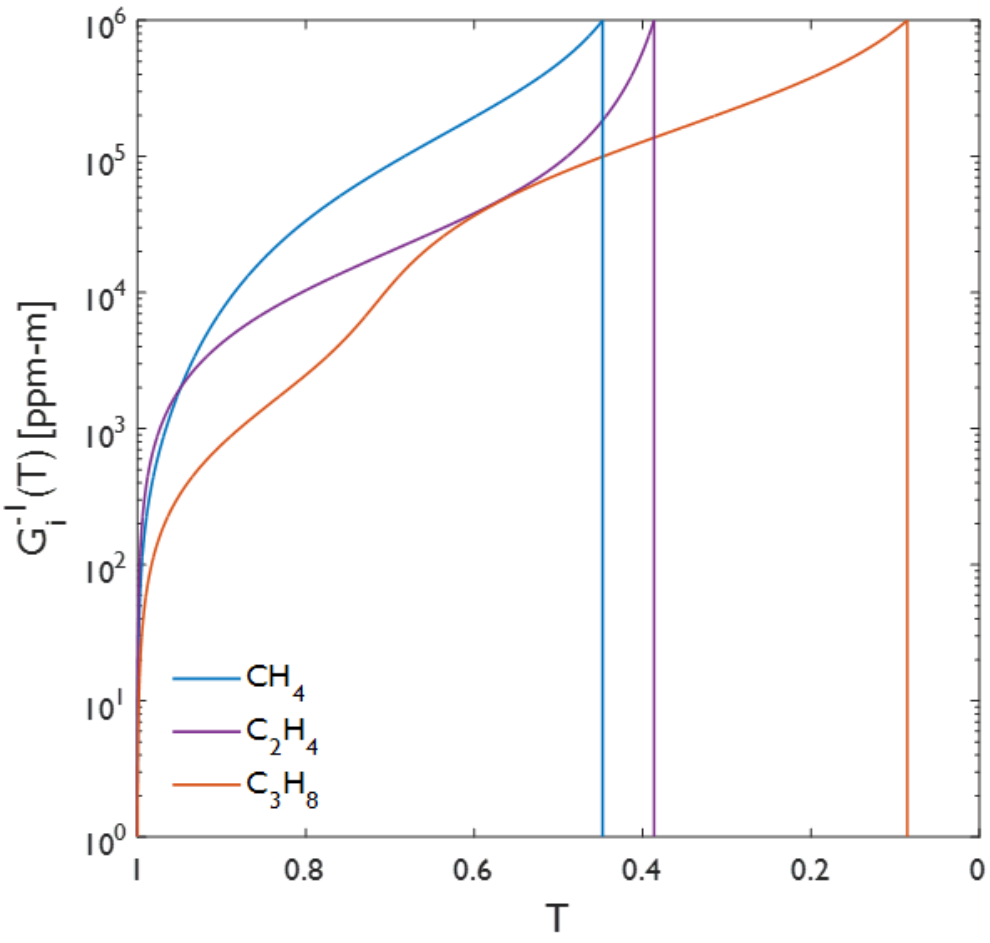

Figure 35: Broadband transfer functions for methane, ethylene, and propane, computed with the optimal box filter.

Chapter 5
Tomography Experiments

The initial intent in performing tomography experiments was to demonstrate practical viability in measuring a methane plume with forced advection, and to compare the accuracy of structured and unstructured optical path arrangements. However, experimental difficulties and issues lead to changes to the procedure between experiments, which served to refine both the apparatus and the measurement technique. This chapter presents the conducted experiments in a chronological context and offers discussion on the aspects learned from each experiment to the next.

In total, 12 tomography experiments were conducted under varying conditions, including beam arrangement, absorbing species, species source release rate, advection, source location, and source height. A summary of all experiments can be seen in the following tables. Table 5 describes the chronological evolution of experiments, with the dates, planned objectives, and information obtained from each experiment, which supplied the motivation for changes applied to each successive experiment. Table 6 provides a summary of the specific parameters for each experiment.

Table 5: Summary of experimental objectives and resulting information obtained to consider for succeeding experiments.

Exp. No.	Date	Reconstruction Objective	Information Obtained
1	Nov. 23, 2015	Advected methane plume with unstructured arrangement	Need more beams
2	Dec. 9, 2015	Advected methane plume with unstructured arrangement and additional beams	Equipment did not allow for more than four beams
3	Mar. 9, 2016	Advected methane plume with structured arrangement to compare with unstructured arrangement	Methane release rate is too low; source placement is sub-optimal
4	Mar. 15, 2016	Advected methane plume with new source location	Advection may be hindering reconstruction quality

5	Mar. 22, 2016	Stationary methane plume	Filter wheels and batteries are a source of large inconsistencies
6	May 4, 2016	Stationary methane plume	Methane absorption is poor at low concentrations
7	May 4, 2016	Stationary propane plume	Raise source height to reduce plume footprint
8	May 5, 2016	Stationary propane plume	Stationary plume may be too turbulent for high quality reconstruction
9	May 6, 2016	Advected propane plume	Successful reconstruction; attempt different source location to test robustness
10	May 6, 2016	Stationary propane plume at different location	Unsuccessful; peak concentration does not correspond with source location
11	May 31, 2016	Stationary ethylene plume	Unsuccessful; absorption not readily seen
12	Oct. 26, 2016	Advected propane plume with more measurement beams	Successful

Table 6: Experimental conditions for tomography experiments.

Exp. No.	Species	Release Rate	Advection	Source Location	Source Height
1	Methane	2.0 *L/min*	Yes	(-0.4,0.1)	-5 *cm*
2	Methane	2.0 *L/min*	Yes	(-0.4,0.1)	-5 *cm*
3	Methane	2.0 *L/min*	Yes	(-0.4,0.1)	-5 *cm*
4	Methane	7.0 *L/min*	Yes	(-0.11,0.11)	-5 *cm*
5	Methane	7.0 *L/min*	No	(-0.11,0.11)	-35 *cm*
6	Methane	7.0 *L/min*	No	(-0.11,0.11)	-35 *cm*
7	Propane	5.36 *L/min*	No	(-0.11,0.11)	-35 *cm*
8	Propane	5.36 *L/min*	No	(-0.11,0.11)	-15 *cm*
9	Propane	5.36 *L/min*	Yes	(-0.11,0.11)	-15 *cm*
10	Propane	5.36 *L/min*	No	(0.10,0.25)	-15 *cm*

11	Ethylene	7.81 *L/min*	No	(-0.11,0.11)	-15 *cm*
12	Propane	8.03 *L/min*	Yes	(0.21,0.21)	-5 *cm*

5.1 Tomography Methodology

All tomography experiments were conducted at the University of Waterloo Live Fire Research Facility, which provided an enclosed space to minimize air drafts but large enough prevent local collection of flammable gases. In this space, a 1 m^2 domain was marked out and the optical paths were arranged around this domain. The reconstruction domain was discretized using a 400 pixel basis.

5.1.1 Unstructured Optical Path Arrangement

The project budget and timeline only permitted development of four detector/emitter pairs. Four optical paths are inadequate to carry out the measurements required for tomographic reconstruction. However, with planning of the placement of the physical pair locations, each emitter can be paired with each of the other detectors, giving a total of $m = 16$ beam, although this disallows time-resolved reconstructions. As such, these reconstructions measure the average concentration of methane in the domain over a set time, which assumes that the release of methane occurs in a pseudo-steady state manner, with the understanding that this technique could be adapted to make time-resolved reconstructions given a larger equipment budget.

The beam arrangement used for the first two experiments was designed to image an advected methane plume, based on a modified genetic algorithm described by Grauer et al. [80]. The genetic algorithm generated a random beam arrangement, simulated absorption measurements of a specified flow field, and performed a Tikhonov reconstruction of the methane concentration field. This reconstruction was compared to that of the true field (i.e. the calculated simulation concentrations) and the error was calculated. The algorithm progressed in generations of a specified number of populations, each with a specified number of beams. Each generation began with the population of the previous herd with the lowest error. Under unconstrained conditions, the algorithm then began to replace one beam of the population with another randomly generated beam, with the number of replaced beams increasing throughout the generation.

For a given flow field, the algorithm uses methane concentration data generated by a large eddy simulation, where the true concentration in each pixel is known. The simulation data comes from a Fire Dynamics Simulator (FDS) file, which provides the expected instantaneous concentrations of methane for the proposed experimental situation, which can be averaged over a time period. The simulation used ran for 20 s with a specified wind speed of 2.0 m/s entering from a vent on the west side of the simulation. The vent is circular and sized similarly to the table fan used for the experiment, 0.3 m in diameter. For simplicity, the centre obstruction of the fan is modeled by a square of equivalent area. An example of the simulation can be seen in Figure 36. The source of methane is placed 5 cm below the measurement plane, at coordinates of (-0.4, 0.1) m, relative to the centre of the domain.

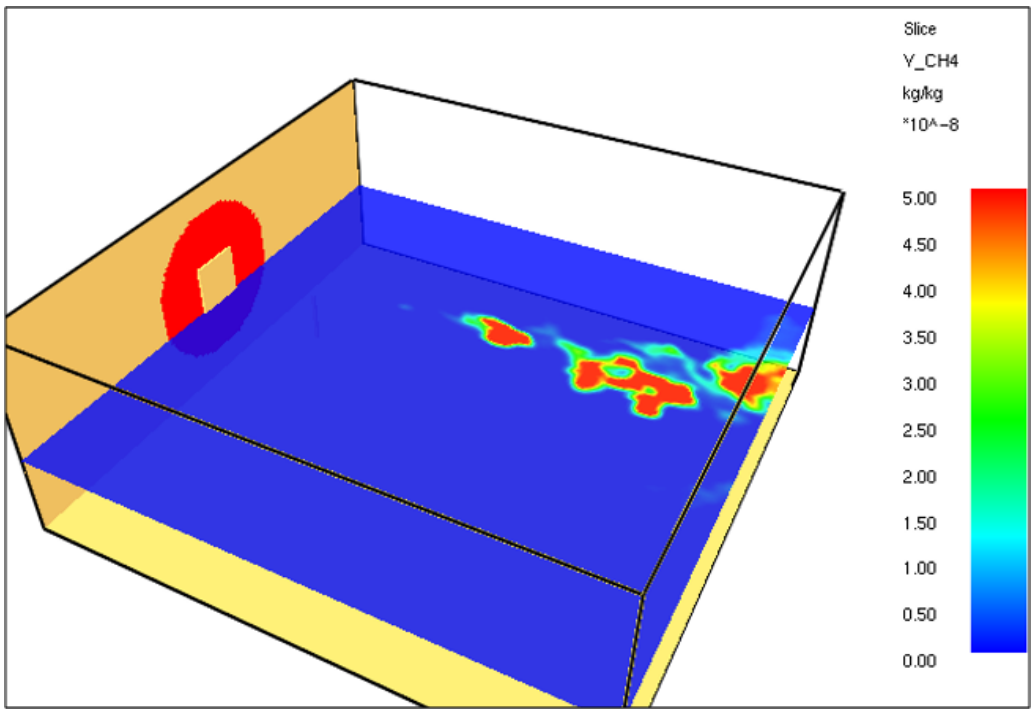

Figure 36: Fire Dynamics Simulator large eddy simulation for unstructured beam optimization.

The algorithm was modified in order to accommodate the physical constraints on the emitter and detector positions. In order to utilize a 16 beam arrangement, each detector and emitter is anchored at a single position and is pivoted on the tripod to form multiple optical paths. An example can be seen in Figure 37. In this way a single beam cannot be randomly generated to replace another. Instead the position of an emitter or detector must be randomly replaced, affecting 4 beams.

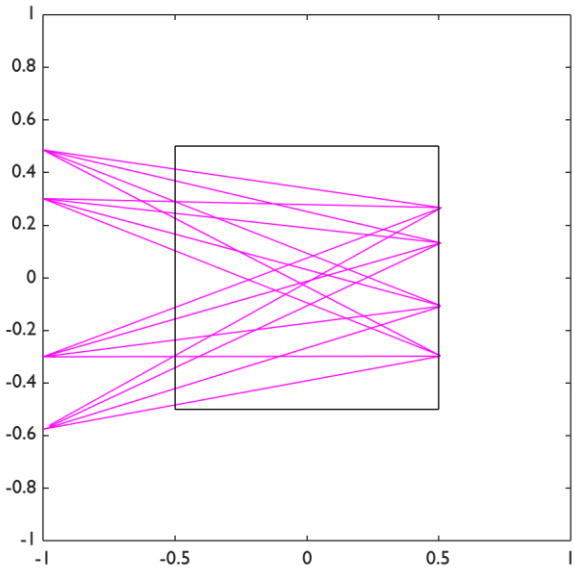

Figure 37: Optimized beam arrangement generated with large eddy simulation data, with constraints set by physical limitations.

5.1.2 Structured Optical Path Arrangement

The cases involving a structured path arrangement are based on work presented by Twynstra and Daun [81]. A resolution matrix approach is used to determine the optimal spacing for a fan-beam arrangement. The resolution matrix is used to calculate an upper bound on the error of the solution that arises from Tikhonov regularization. The objective function operates by minimizing this bound for a variable beam arrangement, which maximizes the information captured by each line of sight. Using this procedure, a path spacing of 32.5 *cm* was selected. This path spacing is the largest spacing possible given the number of beams and the physical size of the domain.

Where in the case of the unstructured arrangements the detector and emitter pairs can be rotated to form pairs with each other unit, the structured arrangement does not utilize the same method. Instead, the domain is rotated by 45° by relocating the methane source and fan between measurement sets. Three rotations for four total measurement sets results in 16 total beams to make a comparable case against the optimized and unstructured arrangement.

5.2 Experimental Results

5.2.1 Experiments One & Two

For the first experiment, the methane source was placed at a location with coordinates of (-0.4, 0.1) m, relative to the centre point of the domain, chosen so that the source lies at the edge of the advection path of the fan. The source is connected to a methane cylinder through a Cole Parmer N034-39 rotameter to control the flow. The table fan was placed at the western edge of the reconstruction domain in attempt to match the specified 2.0 m/s vent flow of the FDS simulation. A photograph of the initial experimental setup can be seen in Figure 38, while the beam arrangements for each experiment can be seen alongside the resulting reconstruction in the following sections.

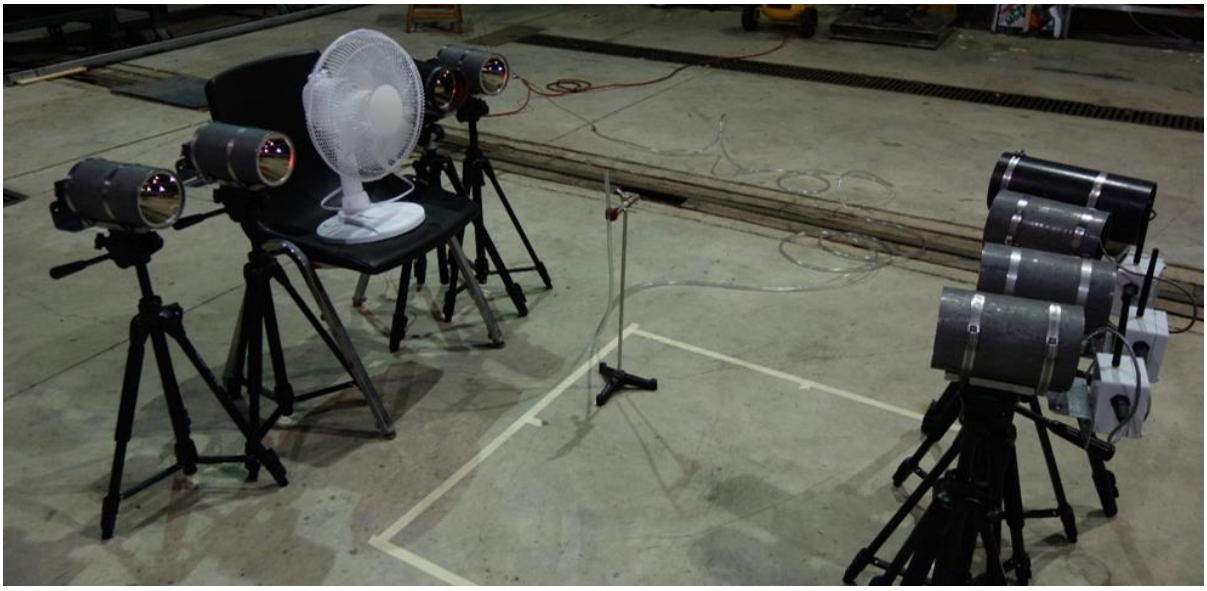

Figure 38: A photograph of an experimental setup for tomography experiments.

As mentioned prior, four sets of measurements were made, each consisting of four optical paths each. Reference measurements were made for each beam set prior to the release of methane into the domain. Methane was released from the source at a height 5 cm below the measurement plane, at a rate of approximately 2.0 L/min. For each set, measurements were made over a span of one minute each without and with methane released in the domain. Figure 39 shows the Tikhonov reconstruction with $\lambda = 0.20$.

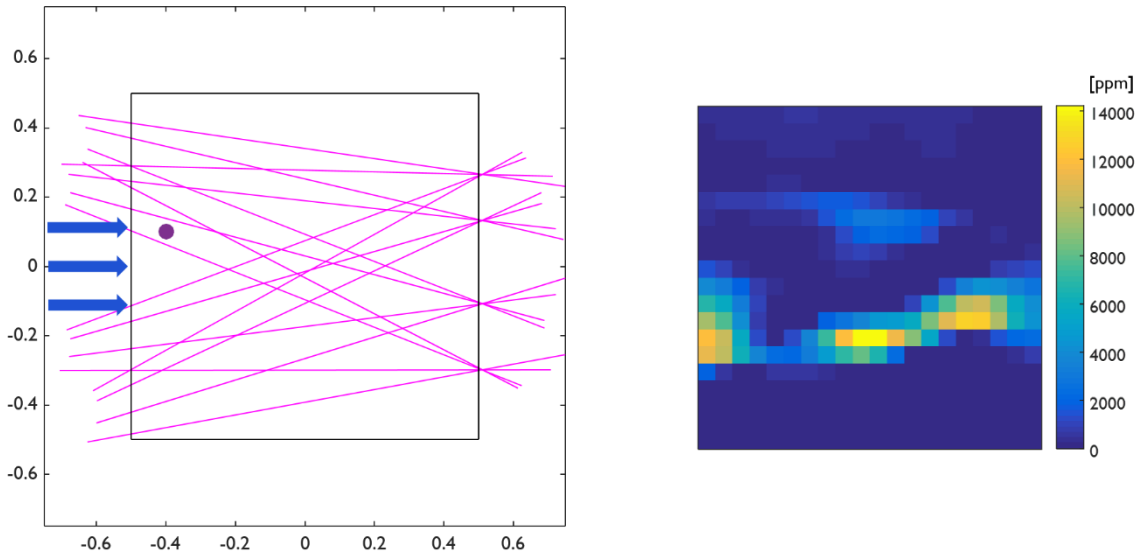

Figure 39: Tomographic reconstruction for experiment #1. Methane source placed 5 *cm* below measurement plane at coordinates of (-0.4, 0.1) with a release rate of 2.0 *L/min*, with advection from the west end.

This result does not agree much with the expectation based on the layout and design of the experiment. Instead, one would expect that the areas of highest concentration would lie in the upper half of the domain in the shape of a triangular plume originating directly above or possibly to the east of the source location. Within the upper half is a small plume shape that would be generally expected; however the pixels of highest measured concentration lie in the lower half along the paths of beams that should not "see" as much methane. Due to the localized positioning of the pixels along one or two specific beams it is likely that the measurements from those beams are a source of error. It was hypothesized at the time that this was due to multiple factors: the beam either measured higher voltages during the reference stage or measured lower voltages during the measurement stage; or misalignment issues of the beam between measurements could affect the result.

The intention of the second experiment was to repeat the procedure of the first experiment whilst incorporating additional information, which would come in the form of additional optical paths of the original beam arrangement after a 90° domain rotation. As a result, rather than four sets of measurements for 16 optical paths, measurements would be made over eight sets for 32 optical paths.

Unfortunately, during the sixth set of measurements, the battery in one of the beams began to discharge rapidly, significantly reducing the voltage supplied by the battery. This was the first observed incident of the effect; the effect of the battery discharge over time was later characterized and is described in Section 3.1.2.

Although the procedure could not be carried out to completion, an additional four paths' worth of information can be included in the reconstruction. Additionally, by using the initial 16 paths for reconstruction, results can be directly compared to those of the first experiment. They can be seen in Figure 40 and Figure 41.

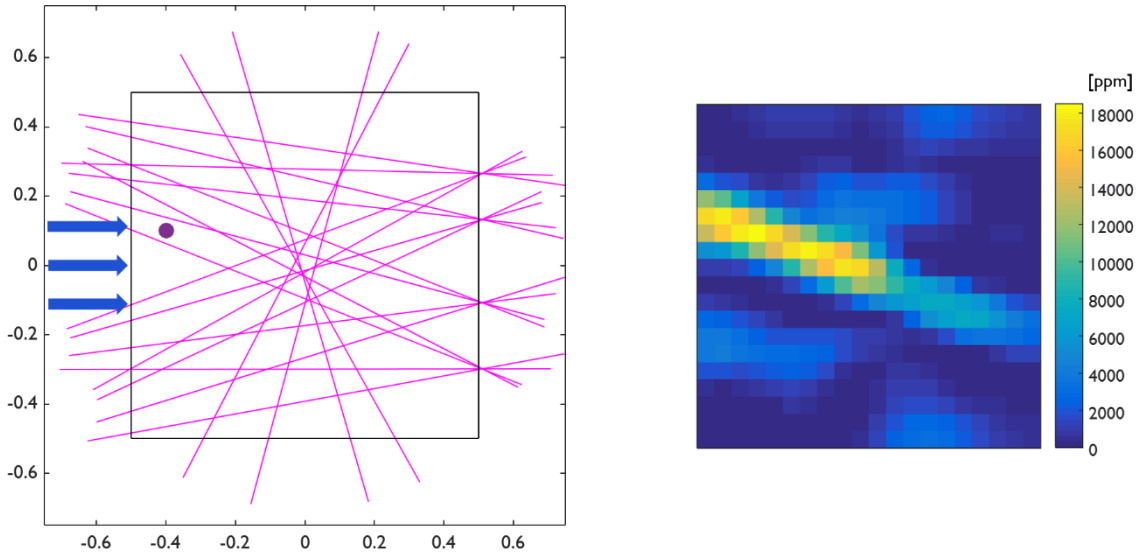

Figure 40: First tomographic reconstruction for experiment #2 using 20 beams. Methane source placed 5 *cm* below measurement plane at coordinates of (-0.4, 0.1) with a release rate of 2.0 *L/min,* with advection from the west end.

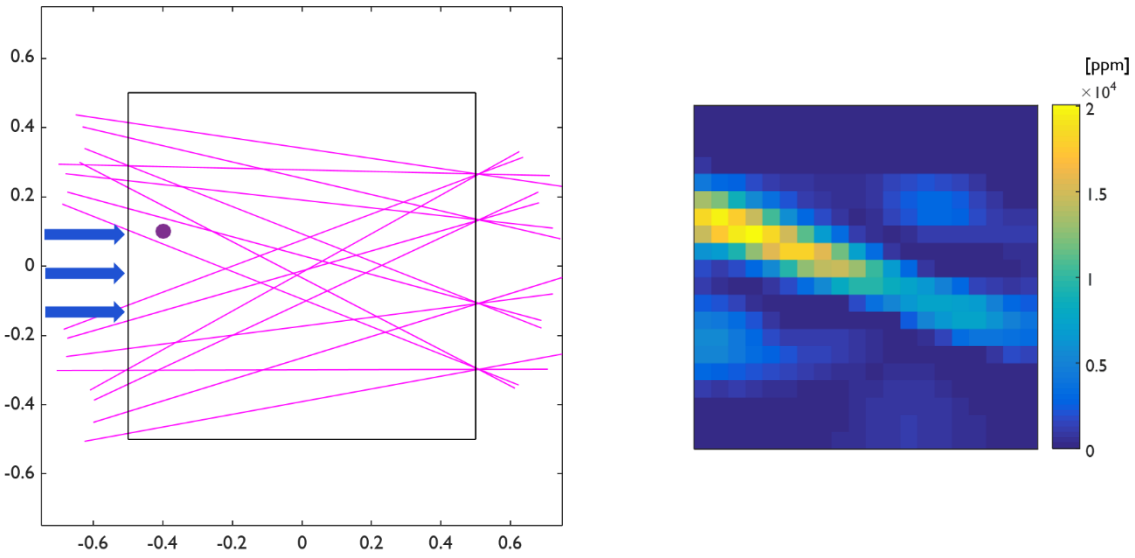

Figure 41: Second tomographic reconstruction for experiment #2 using 16 beams. Methane source placed 5 *cm* below measurement plane at coordinates of (-0.4, 0.1) with a release rate of 2.0 *L/min.*, with advection from the west end.

The results do not differ greatly when compared to each other, with the only differences coming in as small plumes near the edges of the domain. However, in comparing the 16-beam reconstruction to the results of the first experiment, there is a major difference in the location of measured plumes, which suggests that the experimental procedure is not entirely robust. Nevertheless, the results for the second experiment appear to align more closely with general expectations. It can be seen that the highest areas of concentration appear near the source, and are skewed in the direction of advection. The downward deflection is likely caused by the reconstruction tracking a single beam in particular.

5.2.2 Experiments Three to Six

The third experiment was the first experiment in which the FB2750-500 filter was tested for use for reference measurements. Additionally, it was the first experiment to attempt the use of a structured optical path arrangement to serve as a point of comparison with an optimized unstructured arrangement. As in the previous experiments, the location of the source was placed at (-0.4, 0.1) m respective to the centre of the domain, with methane being released from the source at a rate of approximately 2.0 $L/min.$, and with a fan at the west end of the domain. The arrangement, as noted in Section 5.1.2, is generated with a spacing parameter of $\omega = 0.325$. However, due to the physical width

of the fan at the end of the domain, the centre paths are moved outwards an additional 2.5 *cm* as to not obstruct the beam paths.

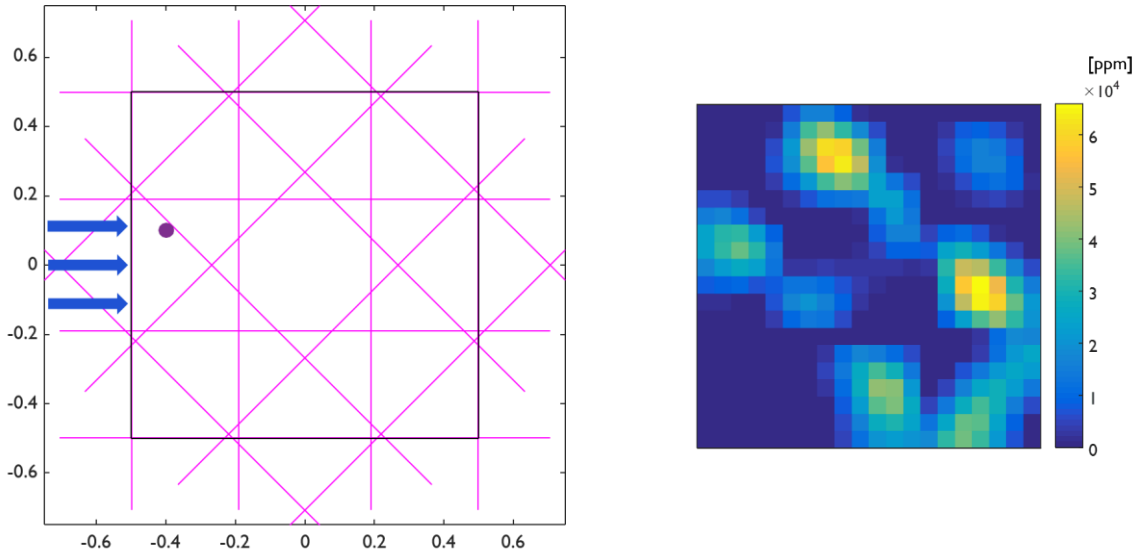

Figure 42: Tomographic reconstruction for experiment #3. Methane source placed 5 *cm* below measurement plane with a release rate of 2.0 *L/min*. at coordinates of (-0.4, 0.1), with advection from the west end.

The results of the third experiment show multiple locations of high concentration, with the largest plume located along a centre diagonal beam. It is apparent that the reconstructed peak concentrations appear to coincide directly along specific beams of the arrangement. As with the first two experiments, the expected plume shape is triangular with an origin at or near the methane source. The inaccuracy of the results are likely due to a combination of issues originating from faster battery depletion compared to the first two experiments (that were not realized at the time), inadequate source emission rate, and alignment disturbances from attempting to use the second reference filter. Due to measurements being time-averaged, faster battery depletion would impact some projected measurement sets more than others.

Although reference measurements with the ThorLabs FB2750-500 were attempted, they were not used for reconstruction. Overall, the quality of this particular estimate is quite poor, which was evidenced by the fact that the detector voltages recorded very little change between reference and measurement sets.

As a result, the experiment was carried out again with a higher flow rate of approximately 7.0 *L/min* to try to measure an appreciable amount of methane. Aside from this, all other factors were unchanged from the previous experiment.

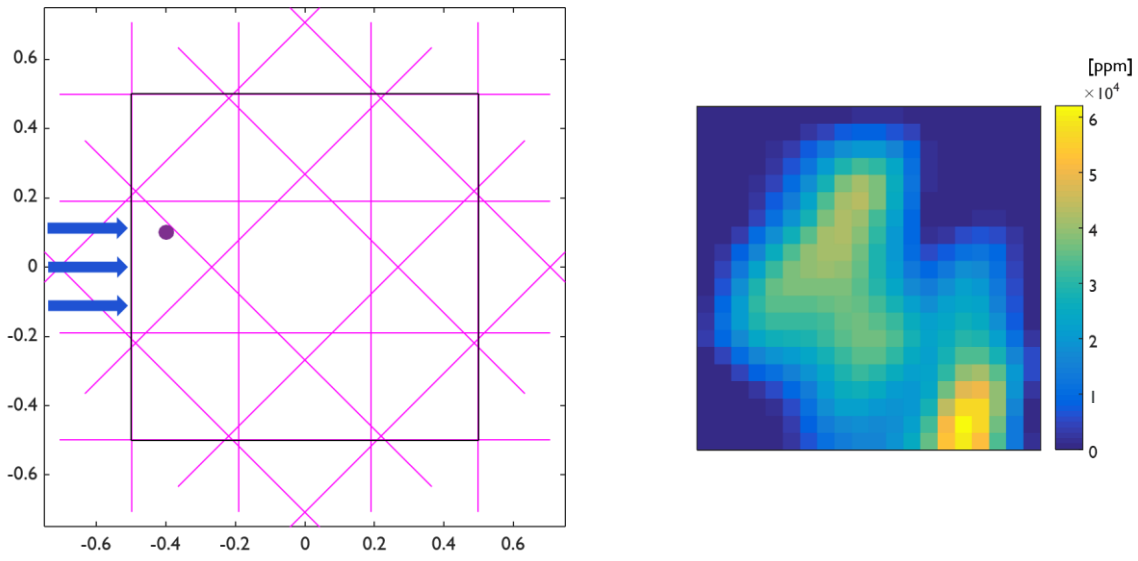

Figure 43: Tomographic reconstruction for experiment #4. Methane source placed 5 *cm* below measurement plane at coordinates of (-0.4, 0.1) with a release rate of 7.0 *L/min*, with advection from the west end.

The result of this experiment shows that the area of highest concentration lies in the lower right corner of the domain, which would go against the basic expectation for the experiment. The shape of the overall plume, however, suggests that that particular peak is an anomaly, and the remainder of the estimate is relatively accurate.

For the fifth experiment, several factors were changed to simplify the experimental setup in attempt to capture the basic plume structure and location. The advection source was removed in order to reduce the turbulent nature of the flow, and the source was lowered from 5 *cm* below the measurement plane to 35 *cm* below. This was to provide vertical distance for the methane exiting the source to naturally expand radially to increase the size of the plume to accommodate the large spacing of the beams. The location of the source was moved to coordinates of (-0.11, -0.11) *m* as it is very nearly an intersection point of three beams.

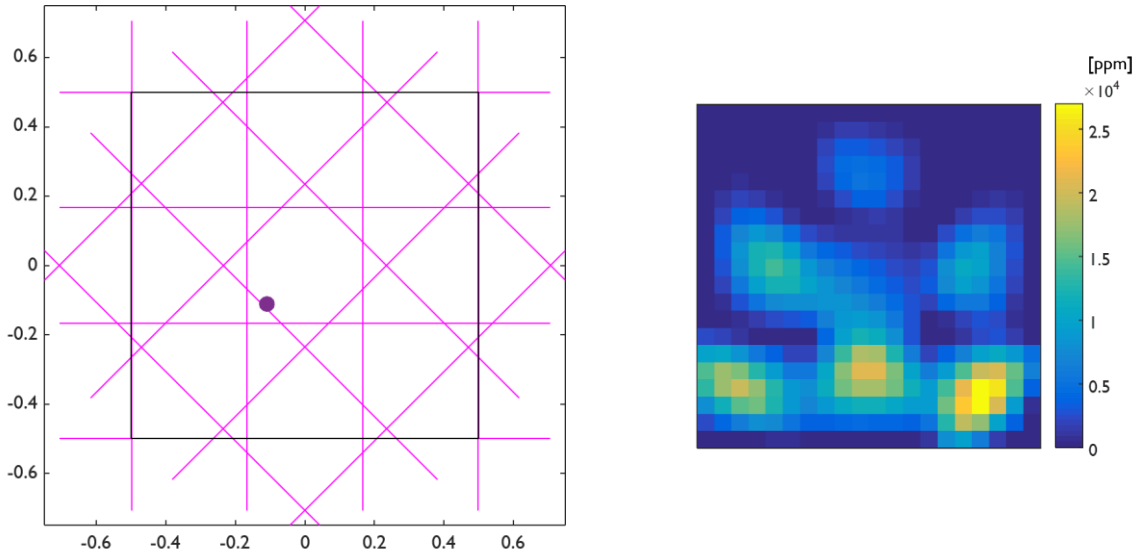

Figure 44: Tomographic reconstruction for experiment #5. Methane source placed 35 *cm* below measurement plane at coordinates of (-0.11, -0.11) with a release rate of 7.0 *L/min*, with no advection.

The reconstructed concentration estimate of this experiment differs drastically from the physical expectation of a stationary methane plume. Although many factors contribute to this, the main conclusion drawn from this experiment is that the alignments of each beam had a high likelihood of being disturbed between reference and measurement sets, once again due to the nature of using the filter wheel in attempt to make use of the FB-2750. Additionally, continual minor issues with sealed lead acid batteries as a power supply are apparent in the reconstruction, and prompted investigation into the issue.

The sixth experiment was carried out in preparation for presentation at the 2016 Canadian Section of the Combustion Institute (CI/CS). For this experiment, the filter wheels and the batteries were removed to help establish consistency and reliability in the detector readings. The filter wheel was removed primarily for two reasons: the selected reference filter is heavily impacted by the variable presence of water vapour absorption; and to eliminate the potential for misalignment issues caused by switching filters between measurement sets. All four emitter units were connected to the same 12 *V* Tenma power supply used for calibration measurements discussed in Chapter 4. The resulting reconstruction for the sixth experiment can be seen in Figure 45.

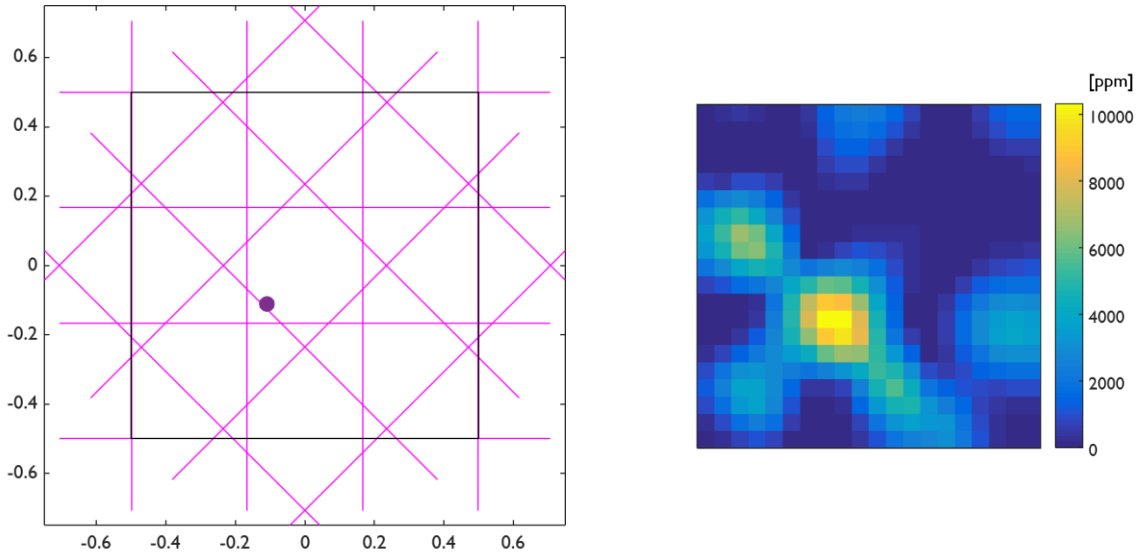

Figure 45: Tomographic reconstruction for experiment #6. Methane source placed 35 *cm* below measurement plane at coordinates of (-0.11, -0.11) with a release rate of 7.0 *L/min*, with no advection, and a constant power supply.

As seen above, the result for this experiment was notably more successful compared to the preceding three experiments. The point of highest concentration lies directly at the intersection point, marking the source location. From that center, the concentration decreases with distance from the source, with some slight aberrations, and small amounts of methane are registered in areas outside of the single expected plume, which could be due to residual methane being measured or a reconstruction artifact.

5.2.3 Experiments Seven & Eight

Although some success has been shown in using methane as a test gas for tomographic reconstructions, it is overall quite difficult to obtain a reasonable result due to the low IR absorption of methane compared to propane and ethylene, as well as the rapidity with which it disperses in air. In its stead, propane was chosen as a test gas as it appears to absorb more readily at lower concentrations, demonstrated above in Figure 34 by each species' transmittance line shape. Additionally, as a larger and heavier molecule, it is expected that it would not disperse in open air as quickly, resulting in higher quality measurements.

For the following experiment using propane, most other parameters from the sixth experiment were maintained. The orthogonal arrangement was used with a spacing parameter of 0.325, the source was placed 35 *cm* below the measurement plane, the source was placed at coordinates of (-0.11, -0.11) *m*, relative to the center, and no forced advection affected the flow. The only change to the procedure was the substitution of methane for propane, which was set to a release flow rate of 5.36 *L/min*.

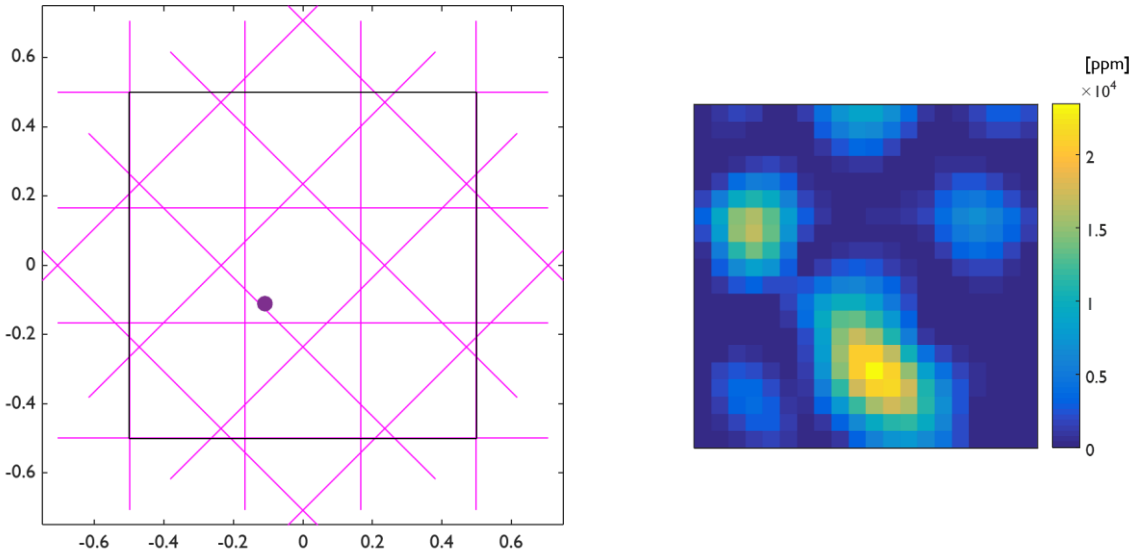

Figure 46: Tomographic reconstruction for experiment #7. Propane source placed 35 *cm* below measurement plane at coordinates of (-0.11, -0.11) with a release rate of 5.36 *L/min*, with no advection, and a constant power supply.

Overall, the reconstruction does not look much different from the immediately prior experiment using methane. However, it is very apparent from the raw voltage measurements that the absorption is much greater. The table below lists the raw **T** vectors used for the Tikhonov reconstructions for the sixth and seventh experiments. In comparing values for each beam, it can be seen that the transmittance measurements are much more sensitive to propane than they are to methane.

Table 7: Comparison of raw transmittance field measurements between methane (experiment #6) and propane (experiment #7).

T_i	Experiment #6	Experiment #7
1	1	1
2	0.999	1
3	0.998	0.883
4	0.998	0.993
5	0.998	0.945
6	0.997	0.903
7	0.991	0.932
8	0.998	0.962
9	1	1
10	0.997	1
11	0.983	0.800
12	0.997	0.980
13	0.997	0.996
14	0.999	0.949
15	0.995	0.979
16	0.997	0.999

Following this experiment, another attempt was made to reconstruct a propane concentration distribution. In this case, the propane source was moved up from 35 *cm* to 15 *cm* below the measurement plane in attempt to reduce the plume footprint in the reconstruction. Due to the greater sensitivity of the detectors to propane, the arrangement was configured to discern between the presence and the absence of the hydrocarbon. Additionally, a fan was used in between measurement sets to clear the air of any lingering propane to try and reduce reconstruction error. Reconstruction results can be seen in the following figure.

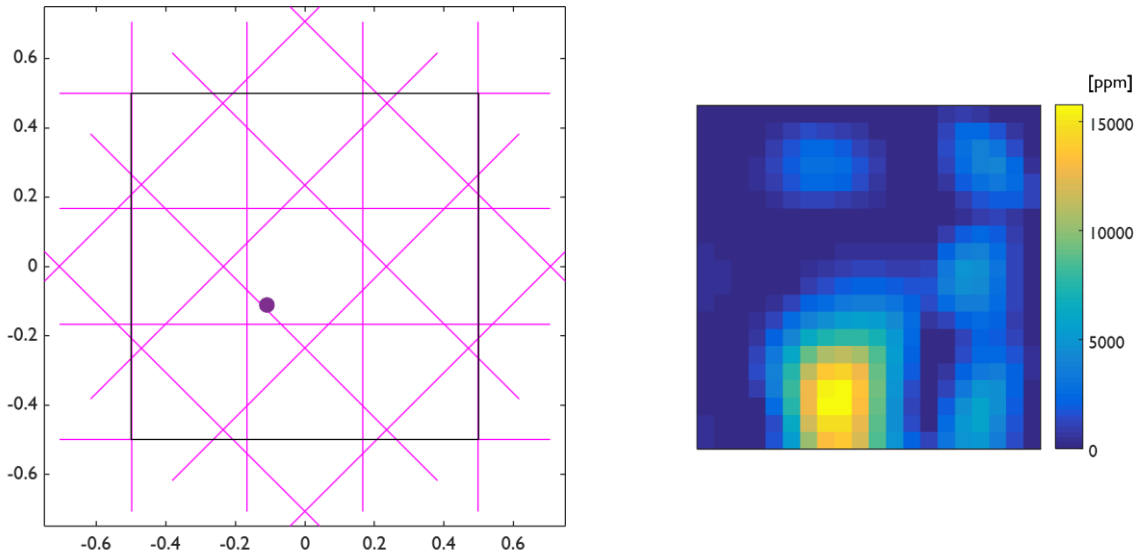

Figure 47: Tomographic reconstruction for experiment #8. Propane source placed 15 *cm* below measurement plane at coordinates of (-0.11, -0.11) with a release rate of 5.36 *L/min*, with no advection, and a constant power supply.

Results for experiment #8 were moderately successful, with the area of highest concentration appearing to the south of the source location. This can be reasonably explained by the fact that some beams had measured higher than expected, skewing the reconstruction locally. This likely occurred due to lingering propane in the domain that was not cleared between measurement sets, despite the use of the fan.

5.2.4 Experiment Nine & Ten

Having performed prior experiments with propane successfully used as the main species of interest, the fan was introduced once again in attempt to improve results. Once again, the source is placed at coordinates of (-11,-11) *cm* relative to the centre of the domain, approximately at the intersection of three beams, at a height 15 *cm* below the measurement plane. Propane was released at a rate of approximately 5.36 *L/min*. Once again, the middle two beams were moved outwards by 2.5 *cm* to accommodate the size of the fan.

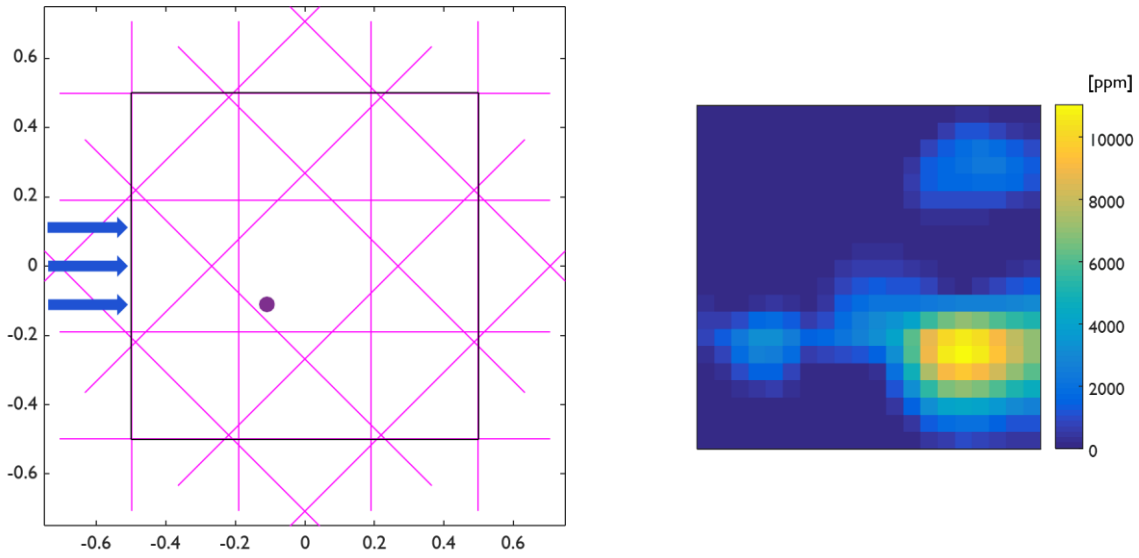

Figure 48: Tomographic reconstruction for experiment #9. Propane source placed 15 *cm* below measurement plane at coordinates of (-0.11, -0.11) with a release rate of 5.36 *L/min*, with advection from the west end, and a constant power supply.

Results for the 9th experiment appear to be reasonable and consistent with expectations, in that the area of highest concentration lies directly downwind from the source location. This is in contrast to the expectation of methane with forced advection due to the higher mass of propane, taking into consideration the lower placement of the source. The remainder of the west side of the domain is free of any measured propane, also as expected. The northeast corner shows presence of propane as well, which may possibly be attributed to the actual presence of some gas, or possibly due to a beam with an anomalous reading.

In an attempt to confirm the robustness of the devices and the procedures at this point, an experiment was performed with the location of the source changed from the location most commonly used. For the majority of the previous experiments, the source was placed at coordinates of (-0.11, -0.11) relative to the centre of the domain. In the following experiment, the source was moved to coordinates of (0.10, 0.25). The objective of this was to attempt to determine the source location having the source placed at a sub-optimal location with regards to beam placement. Figure 49 presents the results of this experiment.

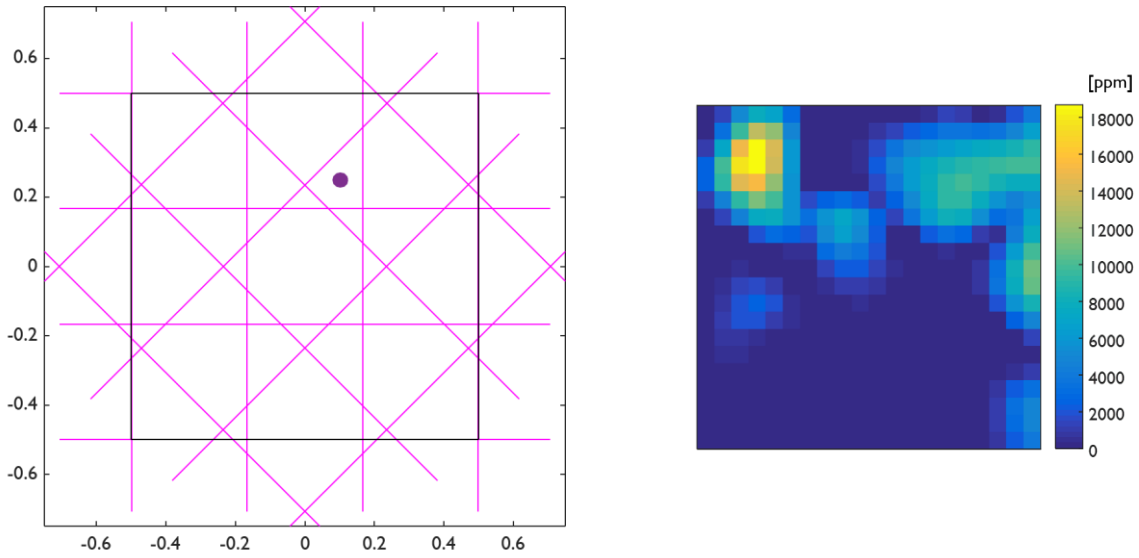

Figure 49: Tomographic reconstruction for experiment #10. Propane source placed 15 *cm* below measurement plane at coordinates of (0.10, 0.25) with a release rate of 5.36 *L/min*, with no advection, and a constant power supply.

As shown in the above figure, the results for this experiment were not successful. The location of the source shows a moderate plume of propane, with the area of highest concentration likely identified incorrectly.

5.2.5 Experiment Eleven

Following propane as an alternate hydrocarbon gas used in attempts of tomographic reconstruction experiments, ethylene was used for the 11th experiment. As it is included in the HITRAN database, its exact absorption profile is known, as shown previously in Section 2.3. The expected transmittance curve shows high levels of absorption even at low volume fractions, suggesting that ethylene is a good candidate for CST experiments.

For ease of comparison, many of the parameters used are identical to those of previous experiments. The orthogonal beam arrangement was used, with the ethylene source located at coordinates of (-0.11, -0.11) at a height 15 *cm* below the measurement plane at a release rate of 7.8 *L/min*. The reconstruction can be seen in Figure 50.

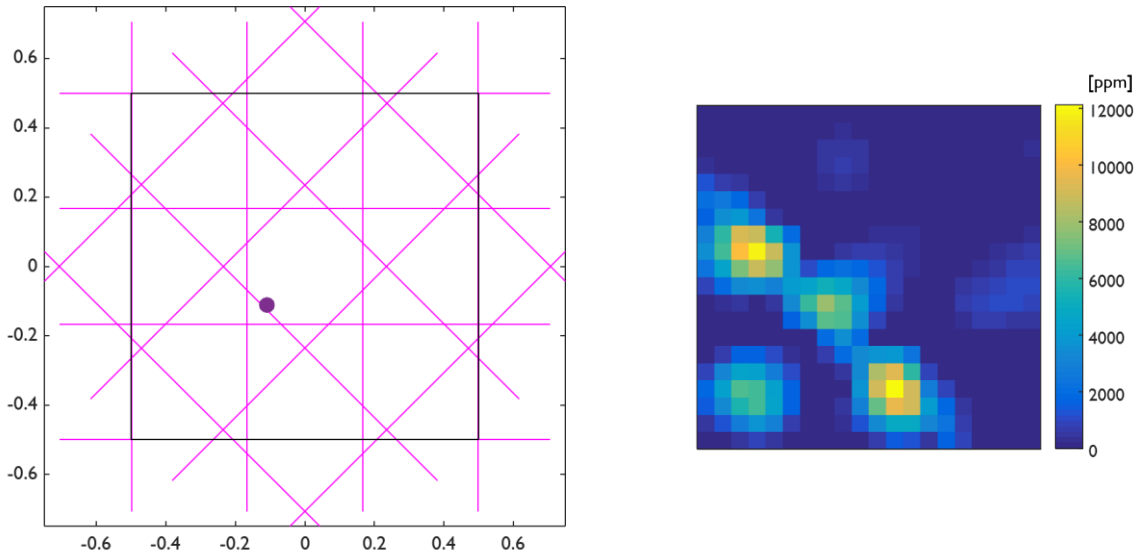

Figure 50: Tomographic reconstruction for experiment #11. Ethylene source placed 15 *cm* below measurement plane at coordinates of (-0.11, -0.11) with a release rate of 7.81 *L/min*, with no advection, and a constant power supply.

Reconstruction of ethylene distributions proved to be unsuccessful. Beam measurements showed little sensitivity to the presence of ethylene, contrary to the expectations set based on test cell measurements. Separate tests were conducted where the source was placed immediately below a beam, with no discernable change in signal. Subsequently, ethylene was no longer considered for use in tomography experiments. It is hypothesized that ethylene is not suitable for tomography due to its dispersion in air as well as its absorption profile. In comparing the absorption profile to methane or propane in Figure 10, it can be seen that although the absorption is much more broadband, the magnitude of absorption is also lower, which may make the presence of ethylene more difficult to detect outside of the controlled environment that the test cell provides.

5.2.6 Experiment Twelve

The final experiment was performed after numerous changes and adjustments to the design of both the open path detectors as well as the experimental procedures. One goal of this experiment was to establish statistical confidence in measurements, which required a significantly higher number of measurements per measurement set. To achieve this, the UWPC-2-NEMA process transmitters were replaced with the NI DAQ (see Section 3.2.3) as it is capable of a much higher measurement frequency.

However, this also required the implementation of an amplifier, discussed in Section 3.2.4. Selecting a sampling frequency of 2 *Hz* (vs. 0.2 *Hz* provided by the process transmitters) also allowed for more measurement sets to be taken within a similar time frame. A modified 35-beam orthogonal arrangement was used, once again due to the physical placement of the table fan. Three centre beams were removed and replaced by two crossed beams as some compensation for the loss of information.

The fan was placed in the northeast corner, pointed diagonally across the domain towards the southwest corner. The propane source was placed at coordinates of (0.21, 0.21) and released at a rate of 8.03 *L/min*.

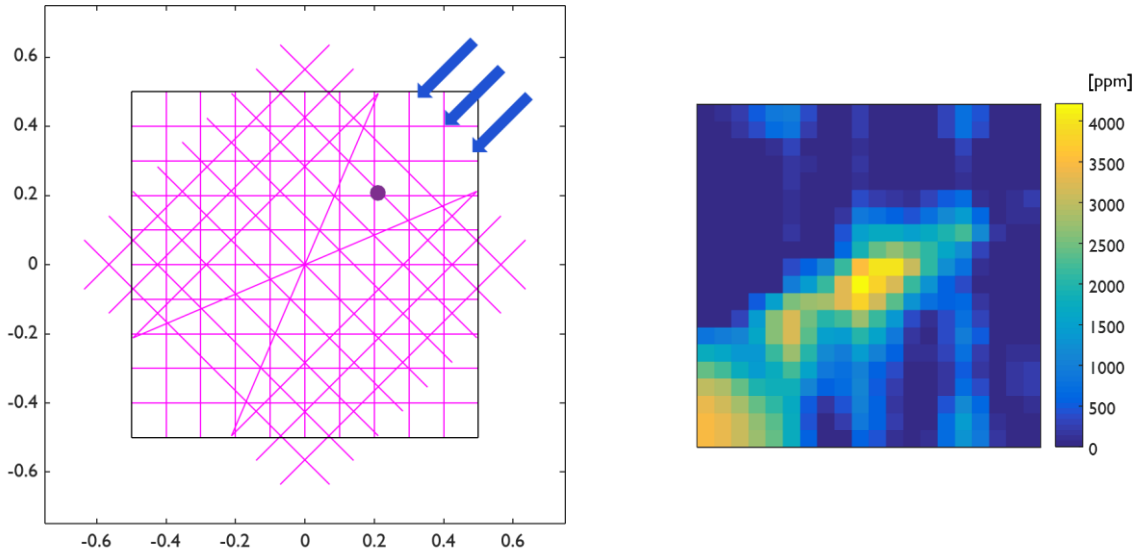

Figure 51: Tomographic reconstruction for experiment #12. Propane source placed 5 *cm* below measurement plane at coordinates of (-0.21, -0.21) with a release rate of 8.03 *L/min*, with advection from the northeast to southwest direction, and a constant power supply.

Qualitatively, the reconstruction quality from this experiment is much higher than in previously executed experiments. This improvement is attributed to the improvements to the open path detector design, especially the amplifier, as well as the increased amount of information obtained through the additional beams. For a robust quantitative error analysis, a ground truth is needed to serve as a point of comparison. A full quantitative error analysis is presented in [74].

5.3 Ground Truth Measurements

In attempts to obtain an independent estimate of the ground truth distribution to serve as a point of comparison for the tomographic estimates, point detectors were used for several separate procedures. To measure methane concentrations, an RKI Instruments GX-2012 unit was rented from Maxim Environmental, Inc. The GX-2012 is a multi-gas detector designed to measure standard gases for confined spaces: LEL combustibles, O_2, CO, and hydrogen sulfide (H_2S). The GX-2012 measures methane via two different sensors, depending on the range of concentration. For concentrations below the lower explosive limit (LEL) of 5000 ppm, the detector uses catalytic combustion as method of detection. Once the detector senses concentrations higher than this, the detector switches sensor types to a thermal conductivity sensor to measure percent volume of the combustible gas. Alternatively, the detection mode can be locked to this setting by the user to avoid damage to the combustion sensor if the local concentrations are known to be higher than the LEL.

The GX-2012 can also detect the presence of other hydrocarbons. However, the detector is not as sensitive to propane as it is with methane. In lieu of this, Imperial Oil once again provided their TVA-1000A FID to carry out measurements.

The first set of procedures with the GX-2012 was designed to visualize the plume shape created by the diffusing source. Measurements of local methane concentration were made at gridded points on a 2D frontal plane above the unit. The MATLAB® *griddata* function was then used to interpolate between these points to generate an approximate concentration map. Figure 52 shows the frontal plume shape with the points at which measurements were made with concentrations in *% vol.* Figure 53 shows a 2D top-down view of the domain. Here, measurements were made at 12.5 *cm* gridded intervals, with additional in-between points in the area around the source. The source was set up 35 *cm* below the measurement plane, in the location at which the previous tomography experiments were carried out (*i.e.* (-0.11, -0.11) *m* from the origin).

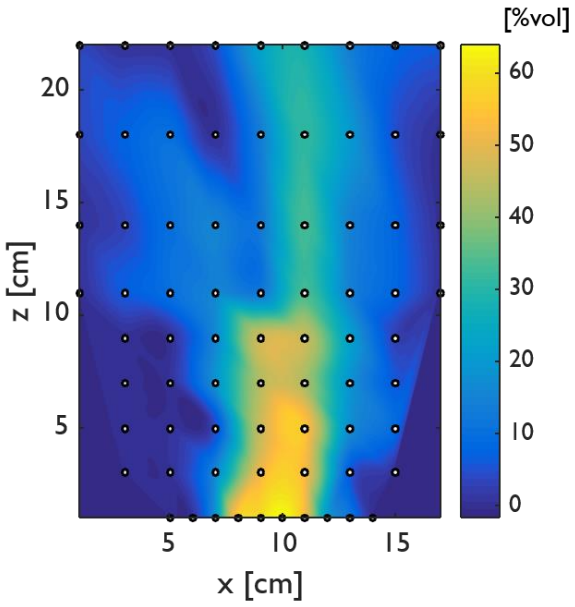

Figure 52: Front view of methane plume from diffuser source in units of % vol.

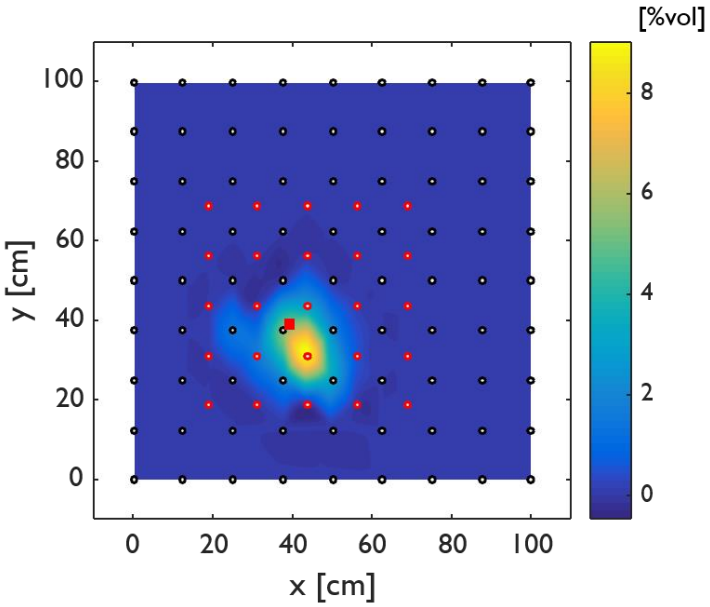

Figure 53: Top-down view of ground truth measurements of methane in units of % vol. from a source 35 *cm* below measurement plane with measurement points shown with source location.

The accuracy of the ground truth measurements is questionable however, which is demonstrated in the figure where it can be seen that the concentration distribution is not centered on the source. This stems from the fact that the number of measurements made at each point are fairly low due to limitations of the GX-2012, in that the response time of the detector is quite long. Measurements at a single point were as far as 10 *s* apart, which results in a large standard deviation at each point.

A second attempt was made with the TVA-1000A FID for a propane plume, which has a much faster response time compared to the GX-2012. Measurements were made every 5 *s* over a minute at 13 locations, under forced advection conditions to match the conditions discussed in Section 5.2.6. A resulting ground truth map can be seen in the following figure. Given the highly turbulent nature of the moving plume, the shape cannot be accurately compared to the reconstruction of experiment #12. However, the magnitudes of the peak concentrations measured in both the reconstruction estimate and the ground truth estimate match closely, demonstrating a successful broadband tomography proof-of-concept.

For experiments 1 to 11, it is difficult to comment on the accuracy of the observed concentrations as there are no ground truth estimates that can serve as a basis for comparison. The results of the final tomography experiment suggest that the reconstructions of prior experiments measured higher concentrations than were actually seen. The agreement between the predicted and measured level of concentration in the final experiment is mainly attributed to incorporating the amplifier to the detector side of each pair, which improves the signal-to-noise ratio. The poor signal-to-noise ratio of the prior experiments would also explain many of the artifacts seen in the reconstructions.

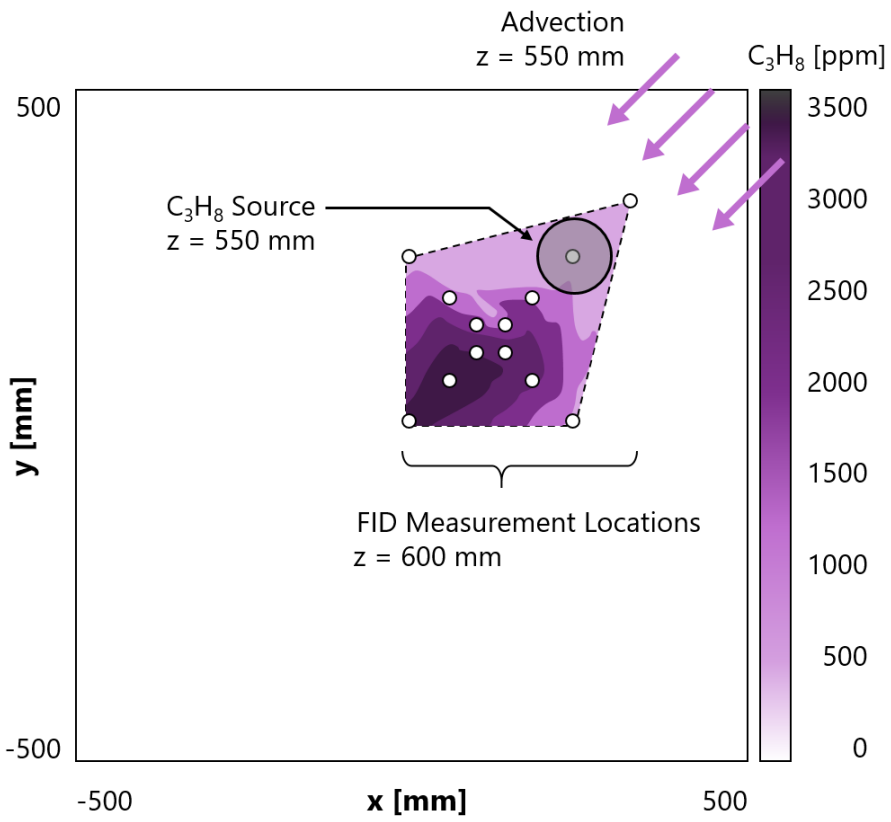

Figure 54: Propane ground truth measurements made by an FID under forced advection.

Chapter 6
Conclusions

Chemical species tomography shows promise for the detection and quantification of large-area hydrocarbon emissions. Current methods for detecting and measuring these emissions are time-consuming and can be severely inaccurate. This thesis presents the development and fabrication of a low-cost broadband open path hydrocarbon detector system that can be used for lab-scale experiments to demonstrate a new broadband tomography technique, with the potential to conduct measurements over larger areas up to 10 m in length.

The open path units are constructed in pairs, each with an emitter side and a detector side. Emitter units contain a Hawkeye Technologies, Inc. mid-IR silicon nitride thermal emitter, powered by a 12 V source, and surrounded by a Phoenix Electroformed Products, Inc. PA10.2 parabolic reflector for efficient collimation. The detector side holds a Hamamatsu P10090-01 InAs photovoltaic detector with a focusing lens and an optical filter. The focusing lens is an LA5370 lens, while the filter is a ThorLabs FB3250-500, the spectral window for which contains the relevant absorption band for hydrocarbon detection. The detector signal is then amplified by a Texas Instruments LM358 operational amplifier, to be read by a DAQ.

6.1 Key Findings

Each detector and emitter pair was calibrated through an absorption cell, custom-built for the large-scale open path detectors. Absorption measurements of toluene, methane, propane, and ethylene were made at varying volume fractions of each species to ensure proper functioning as well as to develop transfer equations that were used in tomography experiments. Expected transmittance models were developed using spectral data available in the HITRAN and PNNL databases, dependent on the species of interest. Spectral line parameters for methane and ethylene, derived from theoretical calculations, are comprehensively reported in HITRAN, while experimental data for molecularly-complex species such as toluene and propane are empirically derived in the PNNL database. Although initial measured transmittance results did not match the expected models, actual filter spectral windows were found to be excluding some spectral absorption data, resulting in non-representative model lines.

Following the construction and calibration of each path, tomography experiments were carried out to estimate lab-scale plumes of hydrocarbons. Through a trial-and-error process, a total of 12 experiments were attempted, with varying levels of success. Six experiments measured a methane plume with and without advection (approximately 2 m/s) under both structured and unstructured beam arrangements, and at flow rates of 2.0 and 7.0 L/min. Five experiments measured a propane plume with and without advection, under a structured beam arrangement, at three different locations with flow rates of 5.36 L/min or 8.03 L/min. One experiment attempted to measure an ethylene plume with little success. Of these experiments, the most successful one was the final experiment which measured a propane plume under forced advection using 35 beams in a modified orthogonal arrangement.

Experiments prior to the final one varied in success due to multiple reasons: sub-optimal or faulty equipment, inadequate signal processing, and low source emission rates. However, once accounting for these issues, the final experiment was able to measure a reasonable plume shape validated with a ground truth obtained through FID measurements.

6.2 Future Work

Suggested future work includes further design improvements, encasing the design in an intrinsically safe or explosion-proof housing, and improvement on experimental procedures. Time-resolved measurements would follow from these improvements, allowing for mass flux estimates.

6.2.1 Design Improvements

Improving tomographic reconstruction quality can be achieved by reconsidering design elements of emitter and detector pairs, including: housing design; emitter source and optical component selection; and miscellaneous improvements for ease of use.

The first priority for the housing design is to ensure that the new housing is either intrinsically safe or explosion-proof, such that it may be operated in a Class I, Div I environment, such as a refinery. Again, this can be achieved by selecting pre-manufactured cases that meet the necessary criteria for conducting tomography experiments. Alternatively, the emitter and detector units can be redesigned and certified such that the units are either intrinsically safe or explosion-proof. Additionally, it is recommended that

a smaller housing is used to reduce the physical size of the units, potentially allowing for more optical paths to be used side-by-side.

While not strictly necessary, a new emitter source is a good candidate for design revision. LEDs are available in the mid-IR with low power requirements and may be a viable option with an amplified detector signal. A new parabolic reflector would also need to be selected, especially if a smaller housing is used for the units.

Further improvements can be made to the optical components, including the selection of new filters for absorption and reference measurements and the inclusion of a filter wheel. Ideally, the new filters would be narrower in bandwidth, with the absorption filter centred on the ro-vibrational absorption band and the reference filter containing no absorption lines of common gases. As well, a filter wheel would have to be incorporated into the design. Following guidelines for intrinsic safety, the optics will be completely encased and a method for actuation would need to be considered.

6.2.2 Experimental Work

Based on the results of the final tomography experiment, it would be worthwhile to revisit some of the tomography experiments conducted to try to achieve a higher quality reconstruction. A number of the reconstructions appear to have small reconstruction artifacts throughout the image (e.g. experiments #3, #5, #6, #7, #8) due to poor signal-to-noise ratios, and may be worth repeating.

Other conditions that were considered for a tomography experiment were larger domain sizes and multiple source locations. A larger domain size was considered to evaluate the scalability of the technique. A larger domain would permit more detectors and emitters to be placed simultaneously, but would require pixel size considerations to also be taken into account. Multiple source locations would evaluate the ability of the technique to isolate source locations as well as provide further insight into the sensitivity and resolution.

6.2.3 Mass Flux Estimates

Mass flux estimates require time-resolved measurements, which would follow from improving upon the currently designed devices and manufacturing more devices that can be used simultaneously. Two

methods for calculating mass fluxes are described by Sandsten and Andersson [82] using consecutive image frames of a methane plume measurement. These methods are the block matching model and the velocity field model. In the block matching model, the movement of turbulent gas is tracked by comparison of pixel blocks in images 50 *ms* apart. The velocity of the gas can be calculated based on movement of pixels of best match between images. The velocity field model uses an axially-symmetric jet velocity profile that is mapped onto gas concentration images based on the centre of the gas jet. The velocity field can then be combined with the concentration of gas in each pixel to produce a total estimate of the flow. Sandsten and Andersson found higher accuracy in calculated methane flow with the block matching model.

These methods use time-resolved measurements, which require the construction of many more beams. Aside from constructing a large number of additional detectors, one method to estimate mass fluxes that was briefly discussed is to relate the variance of the measured absorption and reference signals to the average mass flux of the absorbing species. Due to the turbulent nature of the gas flow, the variance of the absorption signal will have a relationship to the velocity of the flow, which may potentially be used to calculate the species flux.

References

[1] Environment and Climate Change Canada, "Canadian Environmental Sustainability Indicators: Greenhouse Gas Emissions," 2016.

[2] Environment Canada, "National Inventory Report: Greenhouse Gas Sources and Sinks in Canada," 2015.

[3] Canadian Association of Petroleum Producers, "A Recommended Approach to Completing the National Pollutant Release Inventory (NPRI) for the Upstream Oil and Gas Industry," 2014.

[4] Scripps Institution of Oceanography, "The Keeling Curve," 2016. [Online]. Available: https://scripps.ucsd.edu/programs/keelingcurve/. [Accessed: 26-Nov-2016].

[5] D. G. V. and S.-P. X. S. T. F. D. Q. G.-K. P. L. V. A. S. K. A. N. L. B. F.-M. B. J. A. C. U. C. S. E. P. F. P. F. N. G. J. M. G. D. L. H. E. J. B. K. R. K. K. K. K. P., "2013: Technical Summary. In: Climate Change 2013: The Physical Science Basis," Cambridge, United Kingdom and New York, NY, USA, 2013.

[6] J. R. Petit *et al.*, "Climate and atmospheric history of the past 420,000 years from the Vostok ice core, Antarctica," *Nature*, vol. 399, no. 6735, pp. 429–436, Jun. 1999.

[7] IPCC, *Climate Change 2013: The Physical Science Basis. Contribution of Working Group I to the Fifth Assessment Report of the Intergovernmental Panel on Climate Change*. Cambridge, United Kingdom and New York, NY, USA: Cambridge University Press, 2013.

[8] D. G. V. and S.-P. X. Stocker, T.F., D. Qin, G.-K. Plattner, L.V. Alexander, S.K. Allen, N.L. Bindoff, F.-M. Bréon, J.A. Church, U. Cubasch, S. Emori, P. Forster, P. Friedlingstein, N. Gillett, J.M. Gregory, D.L. Hartmann, E. Jansen, B. Kirtman, R. Knutti, K. Krishna Kumar, P., "2013: Technical Summary. In: Climate Change 2013: The Physical Science Basis," Cambridge, United Kingdom and New York, NY, USA, 2013.

[9] M. Vermeer and S. Rahmstorf, "Global sea level linked to global temperature," *Proc. Natl. Acad. Sci.*, vol. 106, no. 51, pp. 21527–21532, 2009.

[10] D. Chivers, *The No-Nonsense Guide to Climate Change: The Science, the Solutions, the Way Forward*, 2nd ed. New Internationalist, 2011.

[11] United Nations/Framework Convention on Climate Change, "Paris Agreement," *21st Conf. Parties*, p. 3, 2015.

[12] D. Krewski, R. Snyder, P. Beatty, G, "Assessing the Health Risks of Benzene: a Report on the Benzene State-of-the-Science Workshop," *J. Toxicol. Environ. Heal. Part A*, vol. 61, no. 5–6, pp. 307–338, 2000.

[13] R. A. Lyons, S. P. Monaghan, M. Heaven, B. N. Littlepage, T. J. Vincent, and G. J. Draper, "Incidence of leukaemia and lymphoma in young people in the vicinity of the petrochemical plant at Baglan Bay, South Wales, 1974 to 1991.," *Occup. Environ. Med.*, vol. 52, pp. 225–228, 1995.

[14] S. Sans *et al.*, "Cancer incidence and mortality near the Baglan Bay petrochemical works, South Wales," *Occup. Environ. Med.*, vol. 52, pp. 217–224, 1995.

[15] S. Thepanondh, J. Varoonphan, P. Sarutichart, and T. Makkasap, "Airborne Volatile Organic Compounds and Their Potential Health Impact on the Vicinity of Petrochemical Industrial Complex," *Water, Air, Soil Pollut.*, vol. 214, no. 1–4, pp. 83–92, 2011.

[16] G. Axelsson, L. Barregard, E. Holmberg, and G. Sallsten, "Cancer incidence in a petrochemical industry area in Sweden," *Sci. Total Environ.*, vol. 408, no. 20, pp. 4482–4487, 2010.

[17] P. Baltrenas, E. Baltrenaite, V. Šereviciene, and P. Pereira, "Atmospheric BTEX concentrations in the vicinity of the crude oil refinery of the Baltic region," *Environ. Monit. Assess.*, vol. 182, no. 1–4, pp. 115–127, 2011.

[18] P. Wilkinson *et al.*, "Lymphohaematopoietic malignancy around all industrial complexes that include major oil refineries in Great Britain.," *Occup. Environ. Med.*, vol. 56, no. 1, pp. 577–580, 1999.

[19] S. Belli *et al.*, "Case-control study on cancer risk associated to residence in the neighbourhood of a petrochemical plant," *Eur. J. Epidemiol.*, vol. 19, no. 1, pp. 49–54, 2004.

[20] J. Kaldor, J. A. Harris, and E. Glazer, "Statistical association between cancer incidence and major-cause mortality, and estimated residential exposure to air emissions from petroleum and chemical plants," *Environ. Health Perspect.*, vol. VOL. 54, pp. 319–332, 1983.

[21] Y. Dumanoglu, M. Kara, H. Altiok, M. Odabasi, T. Elbir, and A. Bayram, "Spatial and seasonal variation and source apportionment of volatile organic compounds (VOCs) in a heavily industrialized region," *Atmos. Environ.*, vol. 98, pp. 168–178, 2014.

[22] C.-Y. Yang, M.-F. Cheng, J.-F. Chiu, and S.-S. Tsai, "Female Lung Cancer and Petrochemical Air Pollution in Taiwan," *Arch. Environ. Heal. An Int. J.*, vol. 54, no. 3, pp. 180–185, 1999.

[23] C.-Y. Yang, B.-H. Cheng, T.-Y. Hsu, S.-S. Tsai, C.-F. Hung, and T.-N. Wu, "Female Lung Cancer Mortality and Sex Ratios at Birth near a Petroleum Refinery Plant," *Environ. Res.*, vol. 83, no. 1, pp. 33–40, 2000.

[24] C.-Y. Yang, C.-C. Chang, H.-Y. Chuang, C.-K. Ho, T.-N. Wu, and P.-Y. Chang, "Increased risk of preterm delivery among people living near the three oil refineries in Taiwan," *Environ. Int.*, vol. 30, no. 3, pp. 337–342, 2004.

[25] C. Y. Yang, J. D. Wang, C. C. Chan, P. C. Chen, J. S. Huang, and M. F. Cheng, "Respiratory and irritant health effects of a population living in a petrochemical-polluted area in Taiwan.," *Environ. Res.*, vol. 74, no. 2, pp. 145–9, 1997.

[26] C. L. Yu *et al.*, "Residential exposure to petrochemicals and the risk of leukemia: Using geographic information system tools to estimate individual-level residential exposure," *Am. J. Epidemiol.*, vol. 164, no. 3, pp. 200–207, 2006.

[27] *Canadian Environmental Protection Act, 1999*. Government of Canada, 1999.

[28] EPA, "Method 21 - Determination of Volatile Organic Compound Leaks," Washington, DC, 2007.

[29] D. Cunningham, "Estimation of VOC emissions," *J. Clean. Prod.*, vol. 3, no. 4, pp. 225–228, 1995.

[30] A. K. Chambers *et al.*, "DIAL Measurements of Fugitive Emissions from Natural Gas Plants and

the Comparison with Emission Factor Estimates," *15th Annu. Emiss. Invent. Conf. US EPA*, pp. 1–11, 2006.

[31] D. Hoyt and L. H. Raun, "Measured and estimated benzene and volatile organic carbon (VOC) emissions at a major U.S. refinery/chemical plant: Comparison and prioritization," *J. Air Waste Manage. Assoc.*, vol. 65, no. 8, pp. 1020–1031, 2015.

[32] T. Holm, "Aspects of the mechanism of the flame ionization detector," *J. Chromatogr. A*, vol. 842, no. 1–2, pp. 221–227, 1999.

[33] J. N. Driscoll, "Evaluation of a New Photoionization Detector for Organic Compounds," *October*, vol. 134, pp. 49–55, 1977.

[34] C. F. Poole, "Ionization-based detectors for gas chromatography," *J. Chromatogr. A*, vol. 1421, pp. 137–153, 2015.

[35] B. C. Smith, *Fundamentals of Fourier Transform Infrared Spectroscopy*, 1st ed. Boca Raton, Florida, USA: CRC Press LLC, 1995.

[36] U. Platt and J. Stutz, *Differential Optical Absorption Spectroscopy: Principles and Applications*. Springer, 2008.

[37] R. Henderson, *A Guide to Laser Safety*, 1st ed. London, UK: Chapman & Hall, 1997.

[38] A. Rogalski and K. Chrzanowski, "Infrared devices and techniques (revision)," *Metrol. Meas. Syst.*, vol. 21, no. 4, pp. 565–618, 2014.

[39] C. A. Brereton and M. R. Johnson, "Identifying sources of fugitive emissions in industrial facilities using trajectory statistical methods," *Atmos. Environ.*, vol. 51, pp. 46–55, 2012.

[40] P. R. Griffiths and J. A. De Haseth, *Fourier Transform Infrared Spectroscopy*, 2nd ed. John Wiley & Sons, 2007.

[41] C. Haisch, "Optical Tomography," *Annu. Rev. Anal. Chem.*, vol. 5, no. 1, pp. 57–77, 2012.

[42] H. McCann, P. Wright, and K. J. Daun, "Chemical Species Tomography," in *Industrial Tomography Systems and Applications*, 1st ed., Cambridge, UK: Woodhead Publishing, 2015, pp.

135–174.

[43] B. W. Stuck, "A new proposal for estimating the spatial concentration of certain types of air pollutants," *J. Opt. Soc. Am.*, vol. 67, no. 5, p. 668, 1977.

[44] R. Byer and L. Shepp, "Two-dimensional remote air- pollution monitoring via tomography," *Opt. Lett.*, vol. 4, no. 3, pp. 75–77, 1979.

[45] D. C. Wolfe and R. L. Byer, "Model studies of laser absorption computed tomography for remote air pollution measurement.," *Appl. Opt.*, vol. 21, no. 7, pp. 1165–1178, 1982.

[46] R. J. Santoro, H. G. Semerjian, P. J. Emmerman, and R. Goulard, "Optical tomography for flow field diagnostics," *Int. J. Heat Mass Transf.*, vol. 24, no. 7, pp. 1139–1150, 1981.

[47] N. A. Yule, A. J., Seng, C. A .H., Felton, P. G., Ungut, A., Chigier, "A Laser Tomographic Investigation Of Liquid Fuel Sprays," in *Eighteenth Symposium (International) on Combustion / The Combustion Institute*, 1981, vol. c, pp. 1501–1510.

[48] K. E. Bennett, G. W. Faris, and R. L. Byer, "Experimental optical fan beam tomography," *Appl. Opt.*, vol. 23, no. 16, pp. 2678–2685, 1984.

[49] H. M. Hertz, "Experimental determination of 2-D flame temperature fields by interferometric tomography," *Opt. Commun.*, vol. 54, no. 3, pp. 131–136, 1985.

[50] R. J. Hall and P. A. Bonczyk, "Sooting flame thermometry using emission/absorption tomography.," *Appl. Opt.*, vol. 29, no. 31, pp. 4590–4598, 1990.

[51] K. B. Chung, F. C. Gouldin, and G. J. Wolga, "Experimental reconstruction of the spatial density distribution of a nonreacting flow with a small number of absorption measurements," *Appl. Opt.*, vol. 34, no. 24, p. 5492, Aug. 1995.

[52] M. Ravichandran and F. C. Gouldin, "Retrieval of Asymmetric Temperature and Concentration Profiles From a Limited Number of Absorption Measurements," *Combust. Sci. Technol.*, vol. 60, no. 1–3, pp. 231–248, Jul. 1988.

[53] S. J. Carey, H. McCann, F. P. Hindle, K. B. Ozanyan, D. E. Winterbone, and E. Clough,

"Chemical species tomography by near infra-red absorption," *Chem. Eng. J.*, vol. 77, no. 1–2, pp. 111–118, 2000.

[54] F. P. Hindle, S. J. Carey, K. Ozanyan, D. E. Winterbone, E. Clough, and H. McCann, "Measurement of gaseous hydrocarbon distribution by a near-infrared absorption tomography system," *J. Electron. Imaging*, vol. 10, no. 3, p. 593, 2001.

[55] P. Wright *et al.*, "Toward in-cylinder absorption tomography in a production engine.," *Appl. Opt.*, vol. 44, pp. 6578–6592, 2005.

[56] N. Terzija *et al.*, "Image optimization for chemical species tomography with an irregular and sparse beam array," *Meas. Sci. Technol.*, vol. 19, p. 94007, 2008.

[57] P. Wright *et al.*, "High-speed chemical species tomography in a multi-cylinder automotive engine," *Chem. Eng. J.*, vol. 158, no. 1, pp. 2–10, 2010.

[58] S. A. Tsekenis *et al.*, "Towards in-cylinder chemical species tomography on large-bore IC engines with pre-chamber," *Flow Meas. Instrum.*, pp. 1–10, 2016.

[59] "FLITES: Fibre-Laser Imaging of Gas Turbine Exhaust Species." .

[60] D. McCormick, M. G. Twynstra, K. J. Daun, and H. McCann, "Optimising laser absorption tomography beam arrays for imaging chemical species in gas turbine engine exhaust plumes," in *7th World Congress on Industirial Process Tomography*, 2013, no. September, pp. 2–5.

[61] I. Pundt and K. U. Mettendorf, "Multibeam long-path differential optical absorption spectroscopy instrument: a device for simultaneous measurements along multiple light paths.," *Appl. Opt.*, vol. 44, no. 23, pp. 4985–94, 2005.

[62] M. Johansson, B. Galle, C. Rivera, and Y. Zhang, "Tomographic reconstruction of gas plumes using scanning DOAS," *Bull. Volcanol.*, vol. 71, no. 10, pp. 1169–1178, 2009.

[63] T. E. Wright, M. Burton, D. M. Pyle, and T. Caltabiano, "Visualising volcanic gas plumes with virtual globes," *Comput. Geosci.*, vol. 35, no. 9, pp. 1837–1842, 2009.

[64] G. G. Salerno *et al.*, "Three-years of SO2 flux measurements of Mt. Etna using an automated

UV scanner array: Comparison with conventional traverses and uncertainties in flux retrieval," *J. Volcanol. Geotherm. Res.*, vol. 183, no. 1–2, pp. 76–83, 2009.

[65] R. Kazahaya, T. Mori, K. Kazahaya, and J. I. Hirabayashi, "Computed tomography reconstruction of SO2 concentration distribution in the volcanic plume of Miyakejima, Japan, by airborne traverse technique using three UV spectrometers," *Geophys. Res. Lett.*, vol. 35, no. 13, pp. 2–7, 2008.

[66] E. P. Olaguer, "Overview of the Benzene and Other Toxics Exposure (BEE-TEX) Field Study," *Env. Heal. Insights*, vol. 9, no. Suppl 4, pp. 1–6, 2015.

[67] J. D. Ingle and S. R. Crouch, *Spectrochemical Analysis*, 1st ed. Englewood Cliffs, NJ: Prentice-Hall, Inc., 1988.

[68] L. S. Rothman *et al.*, "The HITRAN2012 molecular spectroscopic database," *J. Quant. Spectrosc. Radiat. Transf.*, vol. 130, pp. 4–50, 2013.

[69] R. Siegel and J. R. Howell, *Thermal Radiation Heat Transfer*, 4th ed. London, UK: Taylor & Francis, 2002.

[70] S. W. Sharpe, T. J. Johnson, R. L. Sams, P. M. Chu, G. C. Rhoderick, and P. A. Johnson, "Gas-phase databases for quantitative infrared spectroscopy," *Appl. Spectrosc.*, vol. 58, no. 12, pp. 1452–1461, 2004.

[71] M. F. Modest, *Radiative Heat Transfer*, 3rd ed. Academic Press, 2013.

[72] K. J. Daun, S. J. Grauer, and P. J. Hadwin, "Chemical species tomography of turbulent flows: Discrete ill-posed and rank deficient problems and the use of prior information," *J. Quant. Spectrosc. Radiat. Transf.*, vol. 172, pp. 58–74, 2016.

[73] J. Hadamard, "Sur les problèmes aux dérivées partielles et leur signification physique," *Princet. Univ. Bull.*, vol. 13, no. 28, pp. 49–52, 1902.

[74] S. J. Grauer, R. W. Tsang, and K. J. Daun, "Broadband Chemical Species Tomography: Measurement Theory and a Proof-of-Concept Emission Detection Experiment," *J. Quant. Spectrosc. Radiat. Transf.*

[75] K. J. Daun, "Infrared species limited data tomography through Tikhonov reconstruction," *J. Quant. Spectrosc. Radiat. Transf.*, vol. 111, no. 1, pp. 105–115, 2010.

[76] S. King, P. Robertson, A. Jahed, and N. Bodd, "Detection of Fugitive Gas Emissions using Infrared Emitters and Detectors," Waterloo, ON, 2013.

[77] "Intrinsically safe and non-incendive equipment for use in hazardous locations, CAN/CSA-C22.2 NO. 157-92." Canadian Standards Association, 2016.

[78] "Explosion-proof enclosures for use in class I hazardous locations, C22.2 NO. 30-M1986." Canadian Standards Association, 2012.

[79] ThorLabs Inc., "Bandpass Filters." [Online]. Available: https://www.thorlabs.com/newgrouppage9.cfm?objectgroup_id=5871. [Accessed: 11-Feb-2016].

[80] S. J. Grauer, P. J. Hadwin, and K. J. Daun, "Bayesian approach to the design of chemical species tomography experiments," *Appl. Opt.*, vol. 55, no. 21, p. 5772, Jul. 2016.

[81] M. G. Twynstra and K. J. Daun, "Laser-absorption tomography beam arrangement optimization using resolution matrices.," *Appl. Opt.*, vol. 51, no. 29, pp. 7059–68, 2012.

[82] J. Sandsten and M. Andersson, "Volume flow calculations on gas leaks imaged with infrared gas-correlation," *Opt. Express*, vol. 20, no. 18, pp. 20318–20329, 2012.

Appendix A
Detector and Emitter Drawings

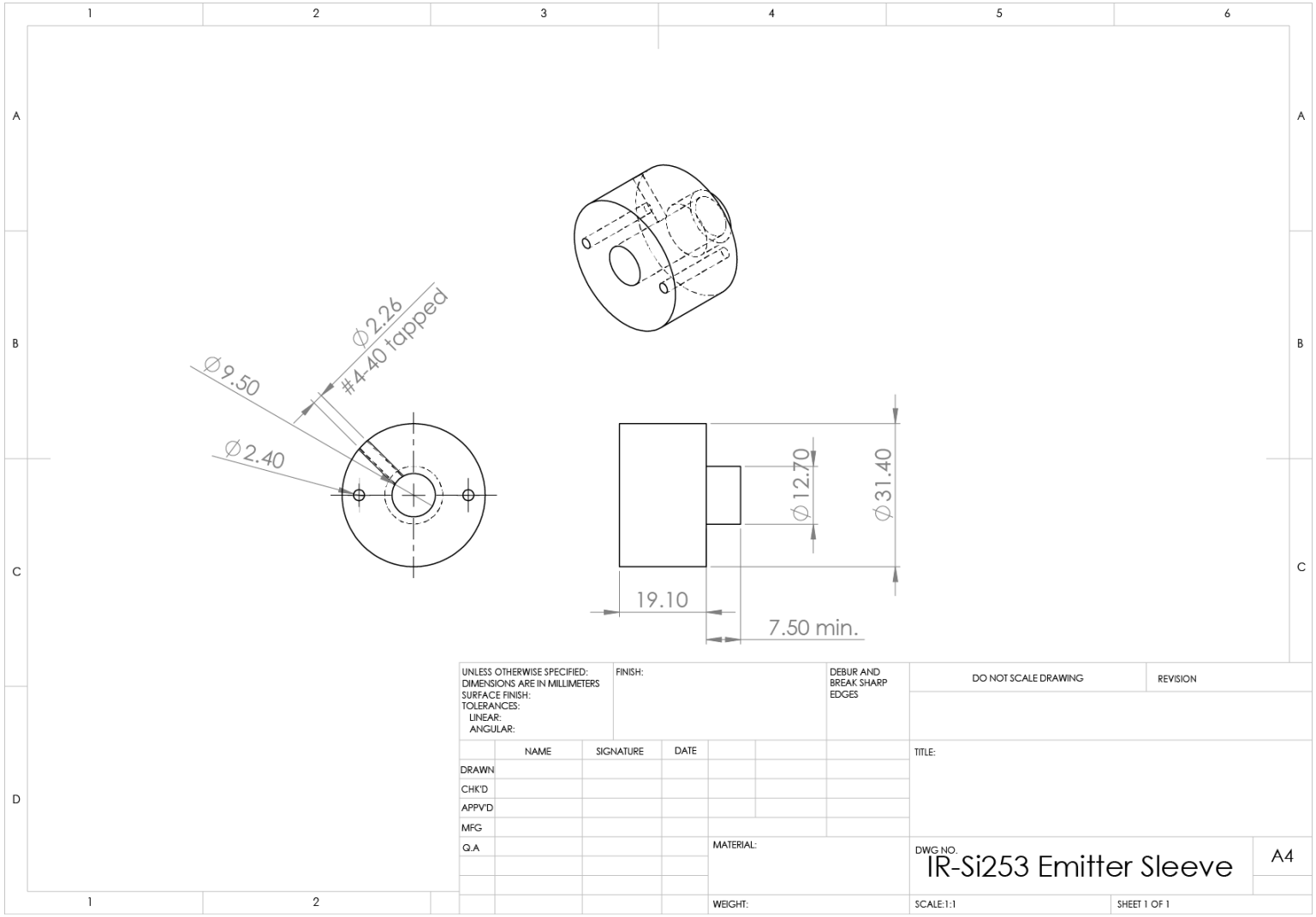
1
2
3
4
5
6
A
B
C
D
∅2.26
#4-40 tapped
∅9.50
∅2.40
∅12.70
∅31.40
19.10
7.50 min.
UNLESS OTHERWISE SPECIFIED:
DIMENSIONS ARE IN MILLIMETERS
SURFACE FINISH:
TOLERANCES:
LINEAR:
ANGULAR:
FINISH:
DEBUR AND BREAK SHARP EDGES
DO NOT SCALE DRAWING
REVISION
NAME
SIGNATURE
DATE
DRAWN
CHK'D
APPV'D
MFG
Q.A
MATERIAL:
WEIGHT:
TITLE:
DWG NO.
IR-Si253 Emitter Sleeve
A4
SCALE:1:1
SHEET 1 OF 1

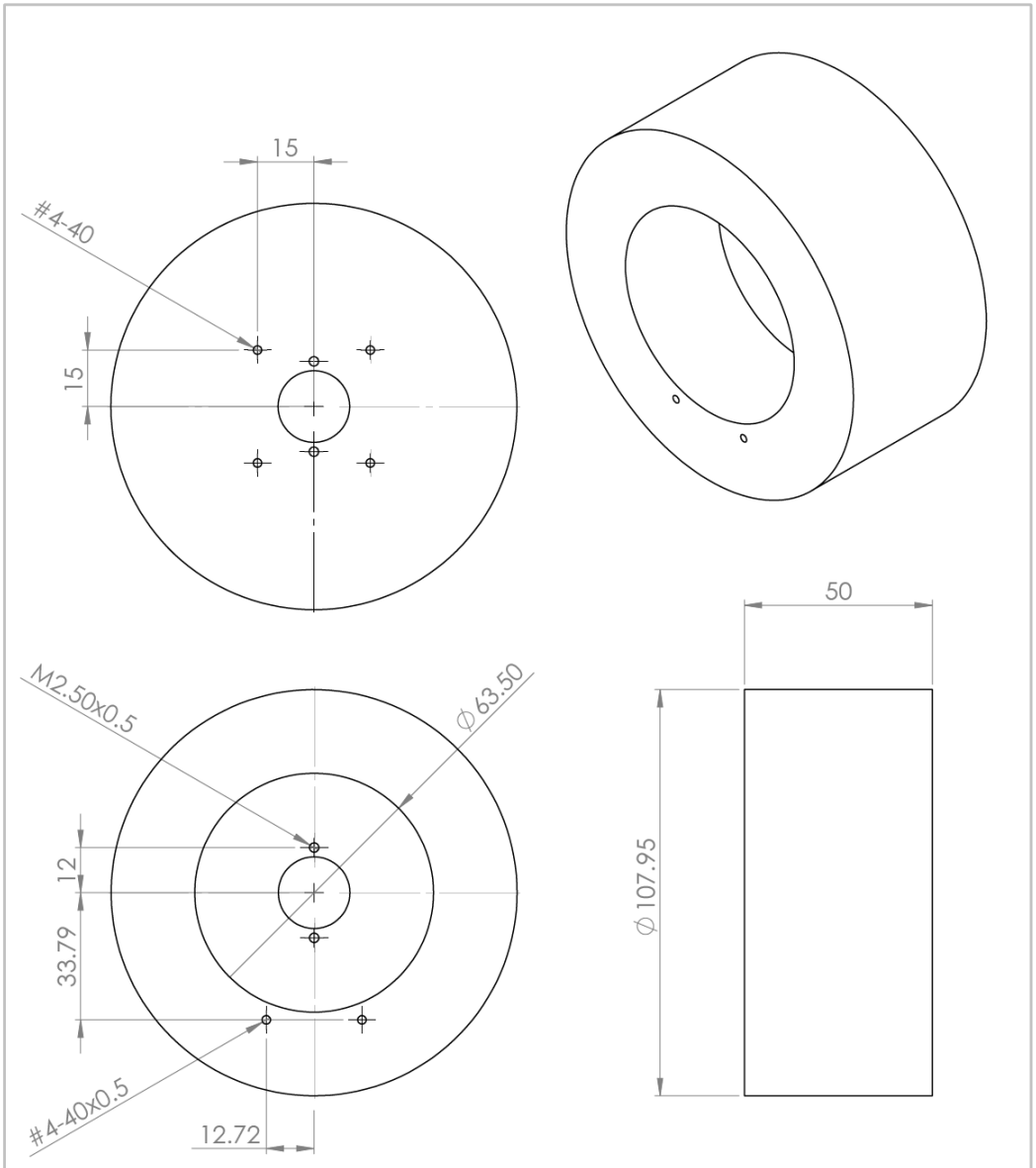

UNLESS OTHERWISE SPECIFIED: DIMENSIONS ARE IN MILLIMETERS SURFACE FINISH: TOLERANCES: LINEAR: ANGULAR:	FINISH:		DEBUR AND BREAK SHARP EDGES	DO NOT SCALE DRAWING	REVISION	
	NAME	SIGNATURE	DATE	TITLE:		
DRAWN						
CHK'D						
APPV'D						
MFG						
Q.A				MATERIAL:	DWG NO. IR-Si253 Detector plate	A4
				WEIGHT:	SCALE:1:2	SHEET 1 OF 1

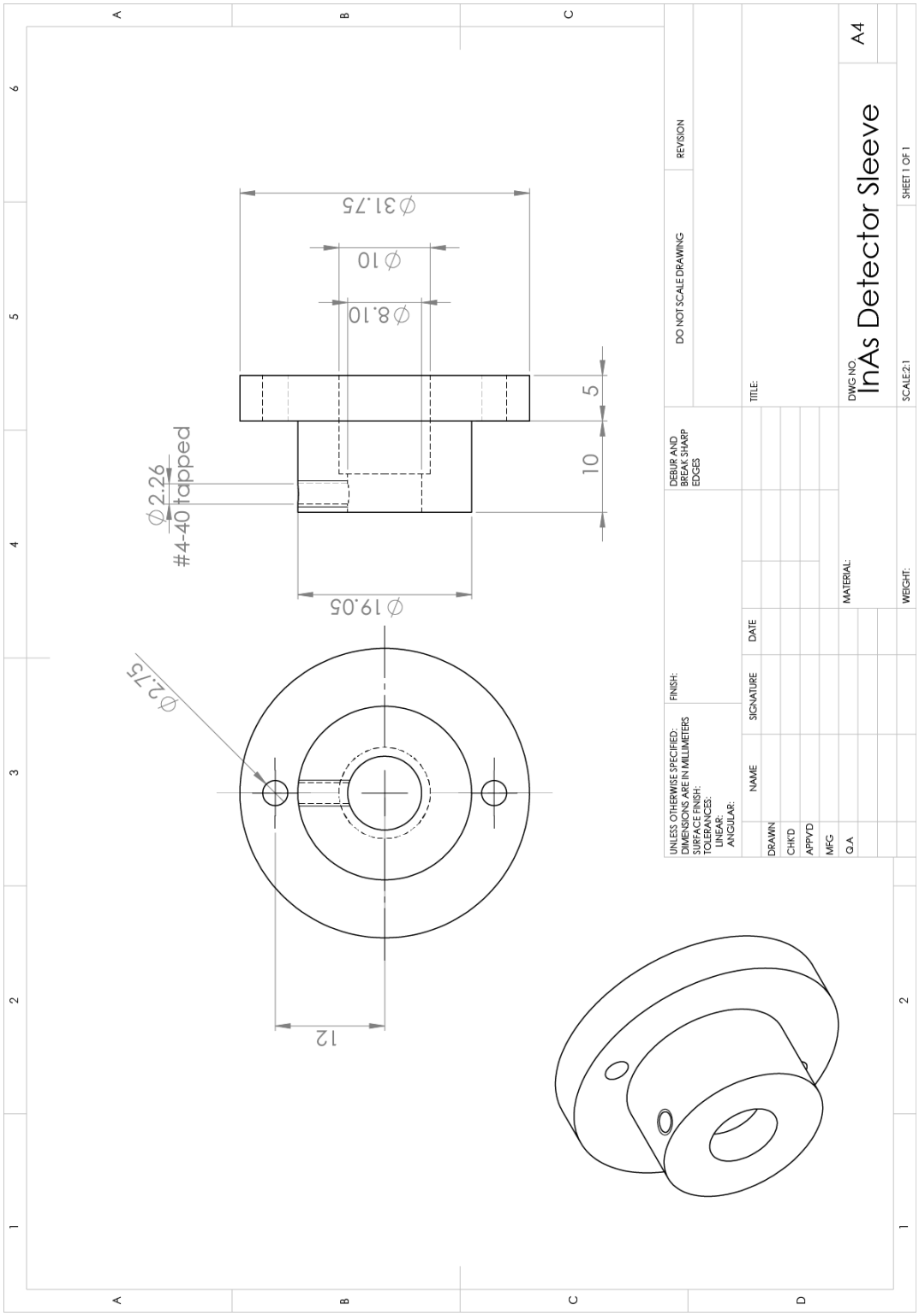
Ø31.75
Ø10
Ø8.10
5
10
Ø2.26
#4-40 tapped
Ø19.05
Ø2.75
12
UNLESS OTHERWISE SPECIFIED:
DIMENSIONS ARE IN MILLIMETERS
SURFACE FINISH:
TOLERANCES:
LINEAR:
ANGULAR:
FINISH:
DEBUR AND BREAK SHARP EDGES
DO NOT SCALE DRAWING
REVISION
NAME
SIGNATURE
DATE
DRAWN
CHK'D
APPV'D
MFG
Q.A
MATERIAL:
WEIGHT:
TITLE:
DWG NO.
InAs Detector Sleeve
A4
SCALE:2:1
SHEET 1 OF 1

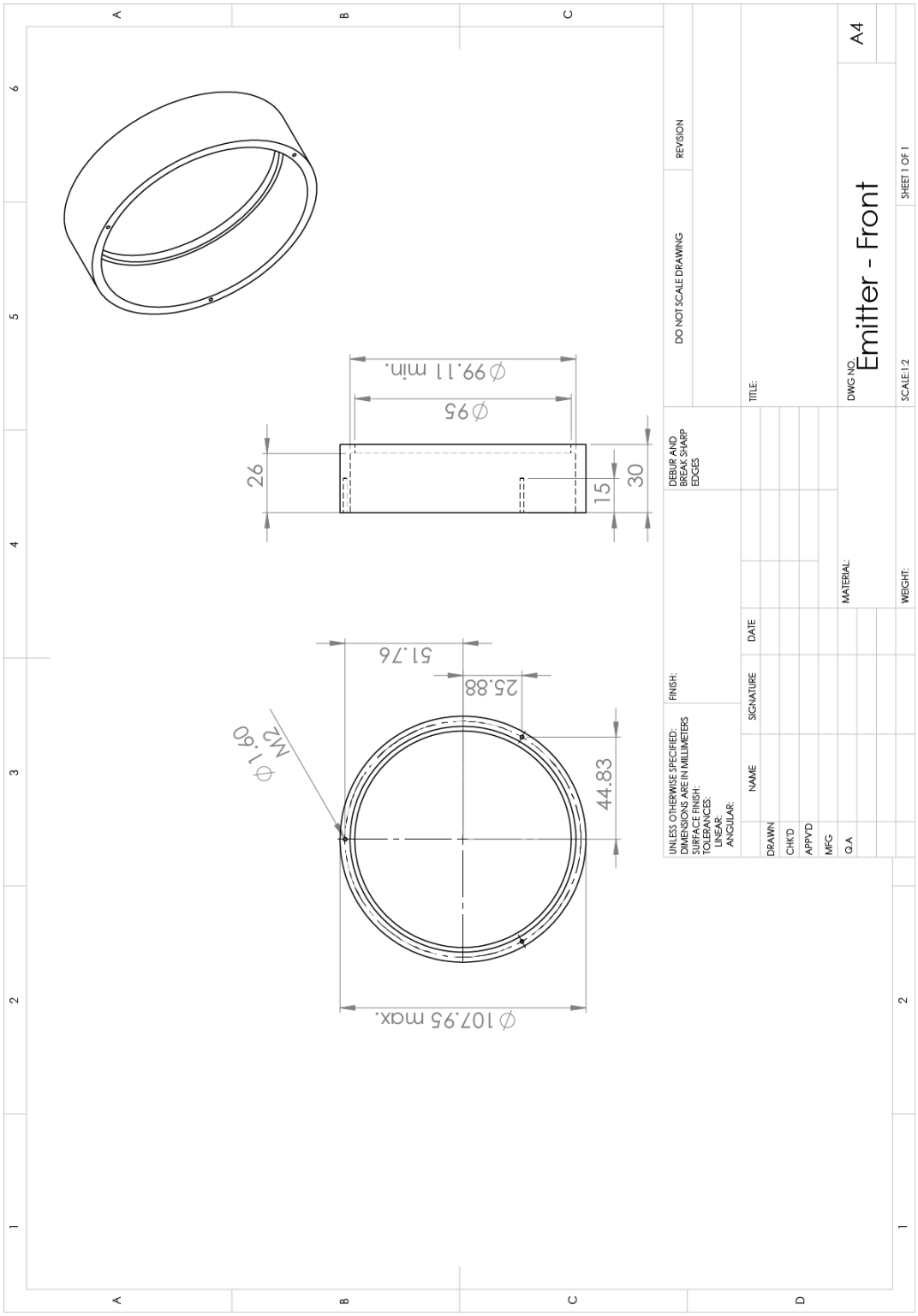
Emitter - Front
A4
SCALE:1:2
SHEET 1 OF 1
DO NOT SCALE DRAWING
REVISION
DEBUR AND BREAK SHARP EDGES
FINISH:
UNLESS OTHERWISE SPECIFIED:
DIMENSIONS ARE IN MILLIMETERS
SURFACE FINISH:
TOLERANCES:
LINEAR:
ANGULAR:
NAME
SIGNATURE
DATE
DRAWN
CHK'D
APPV'D
MFG
Q.A
MATERIAL:
WEIGHT:
TITLE:
DWG NO.
Ø99.11 min.
Ø95
26
15
30
51.76
25.88
44.83
M2.90
Ø107.95 max.

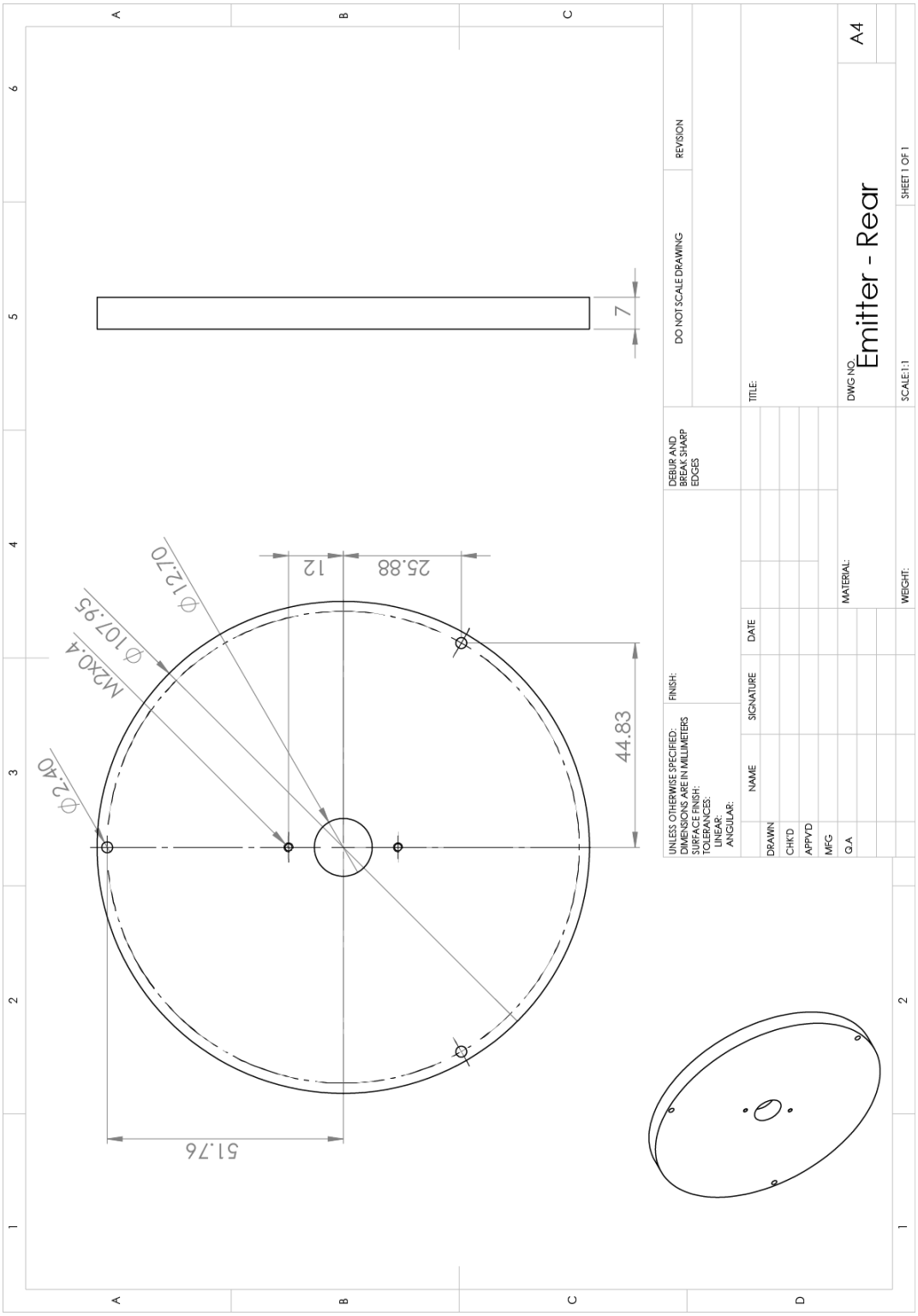
Emitter - Rear
A4
DWG NO.
SCALE 1:1
SHEET 1 OF 1
DO NOT SCALE DRAWING
REVISION
DEBUR AND BREAK SHARP EDGES
UNLESS OTHERWISE SPECIFIED:
DIMENSIONS ARE IN MILLIMETERS
SURFACE FINISH:
TOLERANCES:
LINEAR:
ANGULAR:
FINISH:
NAME
SIGNATURE
DATE
DRAWN
CHK'D
APPV'D
MFG
Q.A
MATERIAL:
WEIGHT:
TITLE:
7
25.88
12
44.83
51.76
Ø12.70
Ø107.95
M2X0.4
Ø2.40

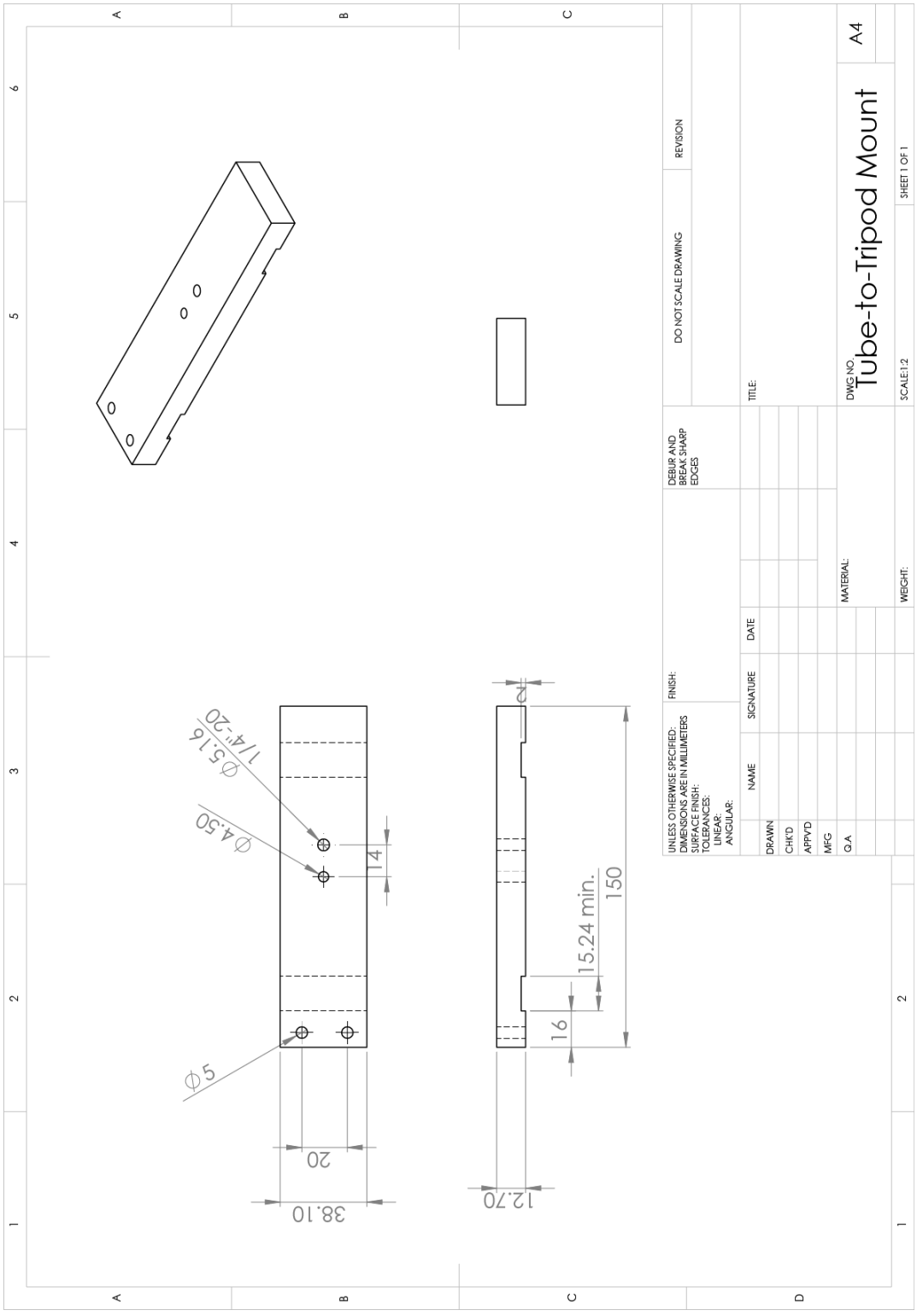
Tube-to-Tripod Mount
A4
DWG NO.
SCALE:1:2
SHEET 1 OF 1
WEIGHT:
MATERIAL:
DO NOT SCALE DRAWING
REVISION
DEBUR AND BREAK SHARP EDGES
FINISH:
UNLESS OTHERWISE SPECIFIED:
DIMENSIONS ARE IN MILLIMETERS
SURFACE FINISH:
TOLERANCES:
LINEAR:
ANGULAR:
NAME
SIGNATURE
DATE
DRAWN
CHK'D
APPV'D
MFG
Q.A
TITLE:
Ø5.16
1/4"-20
Ø4.50
Ø5
14
20
38.10
12.70
16
15.24 min.
150